

2018

Monitoring The Progress Of Damage In A SICf-SICm Composite Nuclear Fuel Cladding Under Internal Pressure Using Acoustic Emission

Luis H. Alva
University of South Carolina

Follow this and additional works at: <https://scholarcommons.sc.edu/etd>



Part of the [Mechanical Engineering Commons](#)

Recommended Citation

Alva, L. H.(2018). *Monitoring The Progress Of Damage In A SICf-SICm Composite Nuclear Fuel Cladding Under Internal Pressure Using Acoustic Emission*. (Doctoral dissertation). Retrieved from <https://scholarcommons.sc.edu/etd/4584>

This Open Access Dissertation is brought to you by Scholar Commons. It has been accepted for inclusion in Theses and Dissertations by an authorized administrator of Scholar Commons. For more information, please contact digres@mailbox.sc.edu.

MONITORING THE PROGRESS OF DAMAGE IN A $\text{SiC}_F\text{-SiC}_M$ COMPOSITE NUCLEAR
FUEL CLADDING UNDER INTERNAL PRESSURE USING ACOUSTIC EMISSION

by

Luis H. Alva

Bachelor of Science
Universidad Nacional de Trujillo, 1982

Master of Science
University of Puerto Rico, 2002

Submitted in Partial Fulfillment of the Requirements

For the Degree of Doctor of Philosophy in

Mechanical Engineering

College of Engineering and Computing

University of South Carolina

2018

Accepted by:

Xinyu Huang, Major Professor

Michael Sutton, Committee Member

Chen Li, Committee Member

George Jacobsen, Committee Member

Cheryl L. Addy, Vice Provost and Dean of the Graduate School

© Copyright by Luis H. Alva, 2018
All Rights Reserved.

DEDICATION

To my family, for their patience, love and understanding.

ACKNOWLEDGEMENTS

This work couldn't be possible without the support of my advisor, Dr. Xinyu Huang, and General Atomics, specially Dr. George Jacobsen. Thanks to Dr. Michael Sutton for his support in understanding the Digital Image Correlation technique and to the people of Correlated Solutions for their technical support. Finally, I want to thank Lee Wooley, Bill Bradley and peers.

ABSTRACT

The relation between the progress of damage and the acoustic emission (AE) activity of a nuclear grade $\text{Si}_f\text{-SiC}_m$ composite tubing under internal pressure was studied. The nuclear grade $\text{Si}_f\text{-SiC}_m$ composite tubing is manufactured by the company General Atomics (GA) and made of nuclear grade HI Nicalon type S fiber preforms following a chemical vapor infiltration (CVI) technique. $\text{Si}_f\text{-SiC}_m$ composites are good candidates to replace current nuclear fuel cladding materials because of the good chemical stability and strength at high temperatures. In this work, a $\text{Si}_f\text{-SiC}_m$ composite tubing was tested under internal pressure at room temperature (RT) to study the damage behavior under hoop loading conditions that occur during a Loss of Coolant Accident (LOCA). In an additional effort, a Pellet Cladding Mechanical Interaction (PCMI) resulting from Reactivity Initiated Accident (RIA) conditions and a thermal shock, meant to represent a reactor reflood, were simulated. The PCMI was simulated by loading the $\text{Si}_f\text{-SiC}_m$ composite tubing, at temperature of 1373 °K (1100 °C), using a solid surrogate and a heating technique that induces temperature gradients through the wall of the $\text{Si}_f\text{-SiC}_m$ composite tubing. The thermal shock was simulated by quenching a $\text{Si}_f\text{-SiC}_m$ composite tubing in water. In all tests, the AE technique was used to monitor the progress of damage by recording the acoustic emission activity within the material using a miniature AE sensor. Digital image correlation (DIC) was used to calculate the full-field strain distribution on the outer surface of the sample. In the case of the high temperature test, a high temperature resistant speckle pattern and a light filtering technique were used. Microscopic and XCT imaging were used

to analyze the damage in the samples caused by the applied load. In the case of the internal pressure loading, a method that relates the acoustic emission activity within the material and the progress of damage is proposed. Damage is the representation of the deterioration of the elastic constants when a load is applied and is typically represented by a damage variable. By finding a correlation between the AE parameters and the damage variable it is possible to predict strains/stresses under specific uniaxial loading conditions. Finally, the Continuum Damage Mechanics method was used to model the mechanical strains of the $\text{Si}_f\text{-SiC}_m$ composite tubing under internal pressure and will be compared to the method proposed.

TABLE OF CONTENTS

DEDICATION	iii
ACKNOWLEDGEMENTS.....	iv
ABSTRACT	v
LIST OF TABLES	ix
LIST OF FIGURES	x
LIST OF SYMBOLS	xiii
LIST OF ABBREVIATIONS.....	xv
CHAPTER 1: INTRODUCTION... ..	1
CHAPTER 2: LITERATURE REVIEW	5
CHAPTER 3: EXPERIMENTAL SETUP.....	30
3.1 THE SIC _F -SIC _M COMPOSITE TUBING	31
3.2 RT OPEN-END SETUP.....	30
3.3 HT SOLID SURROGATE SETUP	32
3.4 QUENCHING SETUP.....	36
3.5 DIGITAL IMAGE CORRELATION	39
CHAPTER 4: DAMAGE MECHANICS AND ACOUSTIC EMISSION	44
4.1 DAMAGE MECHANICS.....	44
4.2 CONTINUUM DAMAGE MECHANICS.....	47
4.3 ACOUSTIC EMISSION.....	50
4.4 AE ENERGY AND DAMAGE VARIABLE D	52

CHAPTER 5: EXPERIMENTAL RESULTS55

 5.1 RT OPEN-END INTERNAL PRESSURE TEST AND AE ANALYSIS.....56

 5.2 CONTINUUM DAMAGE MECHANICS IN UNIAXIAL LOADING74

 5.3 RESULTS OF HT SOLID-SURROGATE TEST.....77

 5.4 QUENCHING TEST RESULTS89

CHAPTER 6: CONCLUSIONS101

REFERENCES103

APPENDIX A – MATERIAL PROPERTIES USED IN FEM MODELING113

APPENDIX B –CONSTITUTIVE EQUATIONS AND BOUNDARY CONDITIONS USED IN THE FEM
MODEL114

LIST OF TABLES

Table 5.1 Dimensions of SiC _f -SiC _m composite samples	55
Table 5.2 Tests performed	55
Table 5.3 Correlations used to calculate the damage variable <i>D</i>	67
Table 5.4 Summary of data corresponding to inter regions and at failure reference points.....	69
Table 5.5 Correlation of damage variable, <i>D</i> and average modulus of elasticity.....	70
Table 5.6 Expression of the damage variable <i>D</i> used to predict the strains obtained during the internal pressure test of sample A.....	76
Table 5.7 Dimensions of SiC samples and surrogate tubes	78
Table 5.8 Summary of AE signals corresponding to sample 2.....	94
Table 5.9 Results of the close-end burst tests	97
Table 5.10 Results of the open-end burst tests	99

LIST OF FIGURES

Figure 3.1 Schematic of RT open-end internal pressure rig	31
Figure 3.2 HT Internal pressurization of SiC cladding.....	32
Figure 3.3 Stresses on the inner surface of sample	33
Figure 3.4 Conceptual design of the HT chamber (a), sample in chamber (b).....	34
Figure 3.5 Schematic of HT apparatus and equipment.....	35
Figure 3.6 The Nernst glower	36
Figure 3.7 Schematic of quenching experimental setup and instrumentation	37
Figure 3.8 Assembly of sample	39
Figure 3.9 DIC Optical arrangement at RT (a) and HT (b)	40
Figure 3.10 DIC vs. strain gauge strains.....	40
Figure 3.11 Speckle pattern on SiC _f -SiC _m tube at RT (a) and HT (b).....	41
Figure 3.12 Spectral blackbody emissive power between 800 °K and 1300 °K.....	43
Figure 4.1 Damage body and RVE (a), damage in a rod axially loaded	45
Figure 4.2 Acoustic emission waveform	50
Figure 4.3 AE Equipment	51
Figure 5.1 Sample mounted showing AE sensor (a), speckle pattern (b) and cross section showing radial cracks.....	56
Figure 5.2 Intratow cracks (a) and fiber pullout after failure	57
Figure 5.3 Stress vs. strain curve and the normalized cumulative AE energy N.....	58
Figure 5.4 Calculating the AE Onset stress of sample A.....	58

Figure 5.5 Stress vs. strain curve: experimental and calculated strain using D.....	61
Figure 5.6 Risettime vs. time for sample A	63
Figure 5.7 Stress vs. strain curve: experimental and calculated strains using $N_{25\%}$	63
Figure 5.8 AE Parameters in the fiber region of sample A.....	64
Figure 5.9 Cumulative AE events of sample A in the fiber-driven region	65
Figure 5.10 Stress vs. strain curve: experimental and calculated strains of sample A	66
Figure 5.11 Stress vs. strain curve: experimental and calculated strains of sample B	66
Figure 5.12 Stress vs. strain curve: experimental and calculated strains of sample C	67
Figure 5.13 Predicted vs. experimental stress-strain curve.....	70
Figure 5.14 Bad match between predicted and experimental stress-strain curve	71
Figure 5.15 Frequently observed waveforms in the matrix-driven region	72
Figure 5.16 Frequently observed waveforms in fiber-driven region	73
Figure 5.17 Example of waveforms discarded due to high risetime.....	74
Figure 5.18 Stress vs. strain curve: experimental and calculated strains of sample A found using expressions from Table 5.4	76
Figure 5.19 Stress vs. strain curve: experimental and calculated strains of sample D found using expressions from Table 5.4	77
Figure 5.20 Picture of SiC_f-SiC_m composite sample mounted on surrogate tube.....	77
Figure 5.21 Temperature profiles and strains of sample G.....	79
Figure 5.22 3D DIC-strain map of sample G at 1350 °K, (a) total axial strains, (b) total hoop strains	79
Figure 5.23 T_{out} , mechanical strains and AE energy of sample G	80
Figure 5.24 50x magnification microscopic image of cross section of sample G	81
Figure 5.25 Temperature profiles and strains for sample H	82
Figure 5.26 Mechanical strains and individual AE events for sample H.....	83

Figure 5.27 X-ray image of sample I.....	83
Figure 5.28 Schematic of sample-surrogate assembly showing the heat flux (a), and image of the meshed sample (b) and the deformed sample from the simulation	86
Figure 5.29 Model predicted temperature profile and stress distribution through the wall at $T_{OUT} = 1087$ °K for SiC _f -SiC _m sample	87
Figure 5.30 Model predicted total strain distribution through the wall at $T_{OUT} = 1087$ °K for SiC _f -SiC _m sample	87
Figure 5.31 Model predicted mechanical strain distribution through the wall of $T_{OUT} = 1087$ °K for SiC _f -SiC _m sample	88
Figure 5.32 Model predicted stress distribution along the length of the sample at $T_{OUT} = 1087$ °K for SiC _f -SiC _m sample G	89
Figure 5.33 Quenching process corresponding to sample 2	90
Figure 5.34 Temperature profile of samples 2, 3 and 4	93
Figure 5.35 Cracks in the face of the endplug of composite tube, sample 2 (a) and sample 3 (b).....	93
Figure 5.36 AE signals found during quenching of sample 2	95
Figure 5.37 Hoop strain map at failure of sample 2	98
Figure 5.38 Open-end burst test results	100

LIST OF SYMBOLS

bar	Pressure
C	Carbon
D	Damage variable
dB	Decibel
E	Elastic modulus, where E_0 or E^* is the initial elastic modulus
I.D.	Inside diameter
O.D.	Outside diameter
K	Kelvin degrees
kHz	Kilohertz
MPa	Mega Pascals
m	meter
mm	millimeter
SiC	Silicon carbide
s	Second
t	time
W	Watt
wt%	percent of weight
Zr	Zirconia
σ	Stress

- ϵ Strain, where ϵ_0 is a reference strain
- μ micron
- $\varphi(F)$ Weibull distribution density function

LIST OF ABBREVIATIONS

AE	Acoustic Emission
ASTM	American Society of Testing and Materials
ATF	Accident Tolerant Fuel
CCD	Charge-Coupled Device
CDM	Continuum Damage Mechanics
CMC.....	Ceramic Matrix Composite
CTE.....	Coefficient of Thermal Expansion
CVD	Chemical Vapor Deposition
CVI.....	Chemical Vapor Infiltration
DIC.....	Digital Image Correlation
DM	Damage Mechanics
FFT.....	Fast Fourier Transform
GA.....	General Atomics
HT	High Temperature
LOCA.....	Loss of Coolant Accident
LWR.....	Light Water Reactor
NDT	Non-Destructive Technique
OS	Onset Stress
PCMI.....	Pellet Cladding Mechanical Interaction
PLS.....	Proportional Limit Stress
PWR.....	Pressure Water Reactor

RIA..... Reactivity Initiated Accident
RT Room Temperature
SiC_f-SiC_m..... Silicon carbide fiber – Silicon carbide matrix
sfc..... Single carbon fiber composite
UPR.....Unsupervised Pattern Recognition
UTS..... Ultimate Tension Stress
XCT.....X-ray Computer Tomography
3D.....Three dimensional
2D.....Two dimensional

CHAPTER 1

INTRODUCTION

Ceramic composites consisting of nuclear grade, highly stoichiometric, silicon carbide fiber and matrix ($\text{Si}_f\text{-SiC}_m$) are being developed as the next generation accident tolerant fuel (ATF) cladding for LWRs [1,2]. The nuclear fuel cladding is the first barrier designed to contain the fuel pellets and to prevent the release of radioactive fission products into the coolant, and eventually to the outside environment [3]. Currently, prototypes of $\text{Si}_f\text{-SiC}_m$ composite tubing are manufactured and extensively tested under laboratory conditions. The toughness of $\text{Si}_f\text{-SiC}_m$ composite tubing under thermo-mechanical loading, needs to be evaluated, not only under normal operation conditions but also under accident conditions such as LOCA and RIA. It is of great interest to develop practical methods and capabilities of replicating extreme thermo-mechanical conditions, simulating the stress state, potentially encountered by the cladding during severe accidents, to determine the relevant mechanical properties [4]. In the case of the fuel cladding materials, the failure typically occurs by fracture due to excess hoop stress generated by internal pressure and temperature gradient [4,5,6,7]. During normal operating conditions the cladding works in compression, however, swelling of the fuel pellet due to temperature gradient and irradiation could hit the cladding creating an internal pressure, which adds up to the internal pressure of the prefilled gas plus the fission gases which accumulate with time [7]. During LOCA and RIA, the fuel cladding develops additional stress and deformation, due to loss of coolant pressure, rising internal gas pressure, severe pellet cladding mechanical

interaction (PCMI), high temperature, and high thermal gradients through the thickness of the cladding [5,6,7,8]. This will result in localized high mechanical contact stress which could lead to mechanical failure [7,9]. Also, during reactor reflood as part of the recover process of LOCA, the cladding will experience severe thermal shock that may induce significant thermal stresses [10,11]. Therefore, a mechanical test of a Si_f-SiC_m composite tubing must include all or some of the work-accident conditions experimented by the Si_f-SiC_m cladding in order to reproduce the damage mechanisms characteristic of the material. In addition to mechanical testing, it is of great importance to understand the kinetics of damage of the Si_f-SiC_m cladding when undergoing loading, in order to predict its behavior [12,13]. Methods such as the acoustic emission (AE) technique and the acousto-ultrasonic technique [14,15,16] are used to monitor the evolution of damage in Si_f-SiC_m composites [12,13]. The AE data is then analyzed to find correlations between the damage mechanisms and the AE parameters such as amplitude, duration or energy. More elaborated methods can be used to analyze AE data, such as pattern recognition, Fast Fourier technique or modal analysis.

In this work, Si_f-SiC_m composite tubing is tested under internal pressure at room temperature to simulate the hoop stresses experimented by the cladding during an accident, such as LOCA and RIA. The test is an open-end internal pressure test, or open-end burst test, that uses a bladder to transmit the pressure to the inner surface of the tubing, loading the tubing in the hoop direction only.

In addition, a test that simulates the pellet-cladding mechanical interaction (PCMI) and a test that simulates the thermal shock during reflooding of the nuclear core are designed. During the PCMI test, the Si_f-SiC_m composite tubing is tested at temperatures

ranging from room temperature to about 1373 °K (1100 °C), measured on the outer surface. The mechanical contact of pellet and cladding is simulated by using a solid surrogate inserted in the Si_f-SiC_m composite tubing and inducing temperature gradients through the wall of the tubing. Due to a mismatch in the coefficient of thermal expansion of tubing and surrogate, an internal pressure is applied on the inner surface of the tubing. During the thermal shock test, the Si_f-SiC_m composite tubing is quenched in water at room temperature (RT) and in hot water. In order to monitor the progress of damage in the Si_f-SiC_m composite tubing, the AE technique is used, and the AE data acquired during the test is analyzed.

As reported in several works [17,18,19-36], a close relation between AE parameters and damage evolution in Si_f-SiC_m composites has been found. Parameters such as the cumulative AE events and cumulative AE energy [18,32,34] have a direct relation with the evolution of the stress-strain curve which deviates from linearity with the accumulation of damage. The prediction of damage of the composite materials, is of great interest for the engineers who design parts made of composites. It is desired, that stress levels such as the proportional limit stress (PLS) and the ultimate stress (UTS), can be predicted to improve safety and efficiency. In the area of composites, a continuum damage mechanics (CDM) approach has been used to make such predictions [37,38]. The method uses data from tensile and torsion tests to find a damage evolution law as function of the forces (stress approach) or the strains (strain approach). This damage evolution law, describes the deterioration of the elastic constants and can be used to predict the deformation of the material.

Based in the analysis of the AE data obtained during the tests, a method that uses AE parameters to find the progress of damage in a $\text{Si}_f\text{-SiC}_m$ composite tubing when loaded under internal pressure is proposed. The progress of damage is represented by a damage variable, D , which has the same definition than the damage variable in Damage Mechanics [39], expressed as the rate of the crack area normal to the loading over the cross-section area of the object. Once obtained, the damage variable, D , can be used to calculate the strains when the stresses and the modulus of elasticity of the material are known. The proposed method is applied to uniaxial loading, as this is the case during the open-end internal pressure test, which induces hoop stresses only in the $\text{Si}_f\text{-SiC}_m$ composite tubing. In addition, a Continuum Damage Mechanics approach is used to model the stress-strain curve obtained during the internal pressure test and the results are compared to the proposed method. A stress approach will be used in this work to obtain the damage evolution function [37].

In addition of AE data, the internal pressure is measured by using a transducer, and the strains in the outer surface of the tubing are measured using strain gauges. As the strain gauges measure the strains in a relatively small area, the 3D stereo DIC method is used to calculate the strain field on a larger area of the surface of the $\text{Si}_f\text{-SiC}_m$ composite tubing. Digital image correlation (DIC) is a non-contact full-field measurement technique with a broad range of applications [42]. In the case of the high-temperature (HT) solid surrogate test, the image acquisition will require a heat-resistant speckle pattern and a light filtering technique to filter the unwanted light emitted from the sample as it behaves as a black body at high temperature [43]. The damaged samples will be analyzed by microscopic and XCT imaging to identify damage mechanisms such as cracks, pull-out and debonding.

CHAPTER 2

LITERATURE REVIEW

The concept of Accident Tolerance Fuels (ATFs) has been proposed to improve safety in the core of the nuclear reactor in the event of an accident such the loss of core cooling capacity [42,43]. The ATF consists of two parts: the nuclear fuel and the cladding which contains the stacked fuel pellets. Attributes of an ATF cladding are improved high temperature oxidation resistance and superior temperature strength compared to Zircalloys [42]. Silicon carbide-based cladding is considered a promising candidate to replace current Zircaloy technology, and possess the required attributes required for an ATF cladding. Some of the advantages of SiC composite are presented in Table 2.1 [44,45,46].

Table 2.1: Comparison of SiC composite and Zircaloy

Property	SiC Composite	Zircaloy
Melting Point	2974 °K	2174 °K
Strength Retention @ 874 °K	500 MPa	120 MPa
Absorption of Thermal Neutrons	25% less	---
Oxidation after 400 sec in 1474 °K steam	Negligible	17%
Hydrogen Production at 1974 °K	40 time lower	---

A few designs of $\text{SiC}_f\text{-SiC}_m$ composite cladding have been proposed. A silicon carbide based cladding or Triplex silicon carbide cladding was proposed by Feinroth et al [1] as an alternative to the current Zircalloys. The Triplex silicon carbide cladding consists

of a monolith SiC inner layer, a SiC_f-SiC_m composite layer at the middle, and a monolith SiC outer layer for corrosion barrier. Ross et al. [9] proposed a Duplex tube consisting in an inner α -SiC monolithic layer and an outer layer made of SiC_f-SiC_m composite tubing. General Atomics proposed a two-layer design consisting of a SiC_f-SiC_m composite tubing with a SiC monolith layer on the outer surface [47]. Regardless of the design, the SiC_f-SiC_m composite layer provides the mechanical toughness necessary to counterbalance the loads that occur during normal and accident conditions in the reactor, and currently is the subject of intensive study.

Despite the improved properties of the SiC_f-SiC_m composite compared to Zircalloys, such as high temperature strength, better neutron economy, reduced hydrogen production during severe accidents and minimal vibration induced fretting [48], the statistical failure of the SiC_f-SiC_m composite must be understood [49]. It must be demonstrated that SiC based cladding material has the required strength and very low failure rates required in nuclear reactor applications. In addition, well-established testing standards and material codes must be established [50]. The only standards applicable to composites are ASTM C1773-13, ASTM C1819-15 and ASTM C1862-17. ASTM C1773-13 is “Standard test method for monotonic axial tensile behavior of continuous fiber-reinforced advanced ceramic tubular test specimens at ambient temperature”. ASTM C1819-15 is “Standard test method for hoop tensile strength of continuous fiber-reinforced advanced ceramic composites tubular test specimens at ambient temperature using elastomeric inserts”. ASTM C1862-17 is “Standard test method for the nominal joint strength of end-plug joints in advanced ceramic tubes at ambient and elevated temperatures”. No other standard is available for testing tubular ceramic composites.

Ceramic matrix composites (CMCs) are anisotropic materials consisting of three basic constituents: fibers, matrix and fiber/matrix interphase, as a result they are highly heterogeneous [51]. In addition, these constituents are ceramic materials, therefore, as in the case of ceramic materials, ceramic matrix composites exhibit a varying strength that is better described by statistical analysis [52,53]. Weibull statistical analysis has been used for many years to describe the strength of ceramics and CMCs [54]. Weibull analysis is based on the weakest link theory which affirm that failure occurs at the most critical flaw by the lowest stress [53]. There is no doubt that the $\text{SiC}_f\text{-SiC}_m$ composite is a strong candidate to replace Zircalloys as cladding material in LWRs. In order to prove it, it is necessary to test the $\text{SiC}_f\text{-SiC}_m$ composite cladding under working and accident conditions, to study the mechanical behavior and to obtain mechanical properties such as elastic constants, onset stress (OS) (stress at initiation of matrix cracking), proportional limit stress (PLS) and ultimate stress (UTS).

Of particular interest in this work is the study of the response of $\text{SiC}_f\text{-SiC}_m$ composite tubing when loaded in the hoop direction, as is the case during the open-end internal pressure test at RT. The progress of damage during the test is monitored using the acoustic emission (AE) technique and post analysis of the AE data is conducted. It is believed that understanding the progress of damage of the cladding undergoing loading by interpreting the AE parameters, will make possible to predict mechanical properties such as the PLS, OS, deformation in the inelastic region, and UTS. To study the mechanical response of $\text{SiC}_f\text{-SiC}_m$ composite tubing when internally pressurized at high temperature and high temperature gradients, simulating a PCMI, is an additional objective. It is also of interest, the study of the behavior of the $\text{SiC}_f\text{-SiC}_m$ composite tubing under thermal shock.

Internal pressurization, hoop loading, high temperature and high temperature gradients are typically encountered by the nuclear cladding during normal and accident conditions.

The mechanical characterization of nuclear fuel cladding materials, mostly Zircalloys, has been made by C-ring compression test [4,55], O-ring tension test [4,5,42,56], close-end pressure burst test [4,56,57], expansion-due-to-compression test [4,7,55,58], segmented expanding cone-mandrel test [4,59] and open-end burst test [6]. These types of test can be conducted at RT or at HT. In the case of C-ring compression test and O-ring tension test, high stress occurs only in a small portion of the sample, and large stress gradient exists. For this reason, these testing conditions are not representative of the working conditions of the nuclear fuel cladding. As mentioned before, in the case of the fuel cladding materials, the failure typically occurs by fracture due to excess hoop stress generated by internal pressure and temperature gradient [4,5,6,7]. Therefore, the internal pressure test better represents the load condition of cladding tubes during normal operating and severe accident conditions. Internal pressure tests or burst tests of tubular specimens can be achieved by liquid (water, oil), gas (air, nitrogen, argon, helium), or solid (silicon rubber, aluminum, copper) pressurizing media [4]. The choice is largely dictated by the desired temperature range required by the test.

Reported burst tests of nuclear fuel cladding, typically use oil or gas as the pressurizing media. Close-end burst tests of nuclear fuel cladding at high temperature are preferentially used compared to the open-end burst test. This is due to the fact that a close-end test creates a bi-axial stress state which is similar to the stresses developed in a LOCA. A $\sigma_{hoop}/\sigma_{axial} \sim 2$ occurs when the ends of the specimen are closed, and a uniaxial state of stress, σ_{hoop} only, is developed when the ends are opened or not constrained [4,8]. At RT,

the pressurized cylindrical tube test or burst test, is very reliable, relatively easy to implement, economical, and can be applied to small and large samples [60]. For laboratory testing, the controlled internal high pressure can be generated by a fluid media, a rubber plug, or an expanding solid plug with split segments. According to Desquines et al. [4], oil pressurization is used up to 773 °K (500 °C), gas pressurization using Helium at temperatures above 773 °K (500 °C), and expansion-due-to-compression test up to 603 °K (330 °C) using a PTFE pellet (PTFE: Polytetrafluoroethylene). In case of ceramics and SiC composites, the preferred test is the expanding internal plug method or rubber plug test because is considered safer than using a gas or liquid media, as a high internal pressure is needed [58].

Room temperature rubber plug tests of ceramic tubes have been reported. Carter reported a load-to-failure rubber plug test of ceramic tubes for the Ceramic Gun Barrel Program Army [59]. However, no further details were reported. Ross et al. [9] reported a rubber plug test of Duplex tubes consisting in an inner α -SiC monolithic layer and an outer layer made of Si_f-SiC_m composite tubing with no crossover of tows. Compared with a monolithic SiC tubing, the Duplex tubing showed to be tougher up to 0.2% strain. A miniaturized fracture stress test of thin-walled tubular SiC specimens at RT was reported by Byun et al. [61]. The internal pressure was applied using the rubber plug technique and the fracture stress calculated was 238.8 MPa. The tubes were made by chemical vapor deposition (CVD) of SiC on pyrolytic carbon, having I.D. of 1 mm. Carpenter [62] and Stempien [63] reported the test of a 3-layer silicon carbide cladding under simulated PWR conditions. The cladding is composed of three layers (Triplex): an inner monolithic SiC layer, a central SiC_f-SiC_m composite layer, and an outer environmental barrier coating

(EBC). The monolith was manufactured via CVD process and the composite was made of Hi-Nicalon type S SiC fibers wrapped around the central monolith with a matrix deposited by chemical vapor infiltration (CVI) process. The EBC was a thin (50-150 μm) SiC coating applied to the outside of the composite. Both studied the mechanical behavior of irradiated Triplex SiC specimens at RT using the rubber plug technique.

Jacobsen et al. [50] used the rubber plug method to test nuclear grade $\text{SiC}_f\text{-SiC}_m$ composite tubes for LWR manufactured by the company General Atomics and compared the data from the rubber plug test with data from a C-ring test. The ultimate tensile stress (UTS) values of the $\text{SiC}_f\text{-SiC}_m$ composite tubes measured with the C-ring method were within 6% of the values obtained with the rubber plug method. Rohmer et al. [64] reported the internal pressure test of a 2D-braided $\text{SiC}_f\text{-SiC}_m$ composite tubing with a 30° fiber angle. The pressurizing media was oil and an elastomeric sleeve was used to transmit the pressure to the inner wall of the $\text{SiC}_f\text{-SiC}_m$ composite tubing. The hoop stress vs. hoop strain curve was reported. Kirill et al. [65] reported a failure map of a $\text{SiC}_f\text{-SiC}_m$ composite tubing constructed with the strains and stresses at failure and at PLS from different mechanical tests such as uniaxial tension, elastomer insert burst test, torsion test, open-end and close-end bladder burst test.

Very few works of ceramic tubing tested at high temperature and under internal pressure have been reported. Chuck et al. [66] reported an interesting high-temperature internal pressure experiment that used glass as the pressurizing media. Glass deforms viscoelastically above its softening temperature. This method was used to test a ceramic matrix composite tube (braided Nicalon/PIP SiC/CeN) at the temperature of 1274 $^\circ\text{K}$ in vacuum, using induction heating to heat the sample and glass. As temperature rises, the

viscosity of the glass decreases rapidly and can behave like a hydraulic fluid. However, this method requires a high temperature end seal. This practically limits the upper usable temperature of this method. Shelleman et al. [67] reported the design and construction of a high temperature burst test apparatus. The apparatus consisted of a steel test chamber, O-ring pressure seals, water-cooled end caps and gas as the pressurizing media. An electrical resistance was used to heat the samples. The burst hoop stress at 1473 °K of siliconized silicon carbide tubes (SCR210 by Coors Ceramic Co.) was reported.

Quenching tests in water of SiC ceramic composites have been reported. Wang et al [68] conducted a comprehensive literature review (for publications prior to 1995) of quenching tests of ceramics and ceramic composites. Singh et al. [69] reported quenching test of continuous fiber reinforced ceramic composites (CFCCs) using different fibers (NicalonTM and NextelTM 312) and SiC matrix. A furnace was used to heat the samples before they were dropped into water at RT. Quenching temperature difference (ΔT) up to 1273 °K (1000 °C) were used and the strength of the samples was measured by four-point bending test. Singh et al. found that ceramic composites showed better resistance to thermal shock than monolithic ceramics, due to various toughening mechanisms such as crack bridging and fiber pullout. The thermal shock induced damage to the ceramic composites are reflected in the decrease in elastic modulus and ultimate strength. The damage increases as ΔT increases. They also concluded that the NicalonTM fiber/CVI SiC matrix composite showed superior resistance to thermal shock damage than other types of SiC composites. The threshold ΔT for damage onset was 973 °K (700 °C). When quenched with ΔT greater than the threshold, a gradual decrease of strength is observed. At $\Delta T=1273$ °K, the retained strength of the composites was 89% of the original value. Lee et al. [10]

studied the development of cracks in monolithic α -SiC tubes from Saint-Gobain. The objective is to understand the behavior of the monolithic layers of a Triplex cladding. The α -SiC tubes were quenched in deionized water at 295 °K (22 °C) from temperatures in the range of 623 °K (350 °C) to 1174 °C. Lee et al. observed pore bridging with pores representing pre-existing flaws and found that the survival probability is 50% when quenching from 673 °K (400 °C) and is zero when quenching from higher temperatures.

Avincola et al. [46] reported oxidation and quench of SiC_f-SiC_m composite tubes at temperatures between 1872 °K (1600 °C) to 2273 °K (2000 °C) in water at 363 °K (90 °C). Avincola et al. used the induction heating technique to heat up the samples and used graphite as susceptor. The quenching water was injected from the bottom by means of a translation mechanism while the sample remained steady. The quenching samples were Triplex tubes which consist of an inner monolith SiC layer, a middle SiC_f-SiC_m composite layer, and an outer monolith SiC environmental barrier coating. After quenching, most of the samples survived, however cracks were observed in the inner monolithic layer as revealed by the X-ray tomography images. They also noticed a steep increase of hydrogen production at 1973 °K (1700 °C), however they estimated that this was still 40 times lower than the hydrogen produced by Zircaloy-4 at the same temperature. Bacalski et al. [70] reported the permeability of SiC_f-SiC_m composite tubes after quenching into water at room temperature and boiling water. The results showed that the samples quenched from 1273 °K (1000 °C) into boiling water retained the permeability, while quenching from temperatures \geq 573 °K (300 °C) results in significant leaking rates of helium. After quenching in room temperature, the remaining strength of the samples was measured using

the expanding plug test showing no difference when compared to the strength of a fresh sample.

Acoustic emission (AE) is an effective non-destructive method for examining the deformation of materials under stress and has been used to study damage in ceramic matrix composites. Different authors agree in the importance of AE technique and found that the AE parameters are related to the evolution of damage in $\text{SiC}_f\text{-SiC}_m$ composites [14-22,25-27,32-36,71]. It was found that the AE activity follows the trend of the stress vs. strain curve [19] and mimic the decrease in elastic modulus of the material [72]. It is believed that AE is a promising technique to classify the failure behavior [17] and to identify the damage phases in $\text{SiC}_f\text{-SiC}_m$ composites [16]. Different AE parameters have been used to correlate the progress of damage in the materials, for example, cumulative number of counts [72], cumulative AE events [19,16], and cumulative AE energy [17]. A similar analysis to the AE technique is the Acousto-Ultrasonic technique which uses a wave generator and a receiver to measure the velocity of the wave traveling through the material [14]. The wave velocity is correlated to the progress of damage in the material.

The analysis of the AE data is crucial for the understanding of the progress of damage in the material. A simple approach is to analyze the AE data by plotting AE parameters such as duration vs amplitude and observe trends or clusters of data that could be related to specific damage mechanisms. The cumulative data of AE parameters such as the energy or the number of hits, are typically plotted against the strains or stresses with the objective of finding a correlation with the stress-strain curve [17,18,28, 29,31,33,31]. Also, mechanical parameters such as the stress intensity factor are correlated with the AE energy [20,21]. However, a simple analysis of the AE parameters is not enough to correlate

the AE events with damage mechanisms. It is difficult to differentiate the AE signals that corresponds to different damage mechanisms in the composite such as matrix cracking, fiber braking, interfacial debonding, and frictional sliding [32]. In the other hand, AE signals that correspond to the same damage mechanism may have differences, i.e. the signal is attenuated because of the presence of matrix cracks. The use of only one AE parameter to identify a specific damage mechanism is sometimes possible when this damage mechanism is predominant. When more than one damage mechanisms occur at the same time, a careful analysis of the AE signals is necessary with the assistance of methods such as unsupervised pattern recognition (UPR) [15,16,26,32,34], Fast Fourier Transform (FFT) [19,27,30], modal analysis [36,19] or wavelet decomposition [28]. In some cases, two or more of the available methods are used simultaneously to analysis the AE data [19,34].

Reifsnider et al. [20] used the AE technique to monitor the progress of damage in static tensile fatigue test of Boron-aluminum and Boron-epoxy composites at RT. Reifsnider et al. found a good correlation between cumulative AE counts and the level of damage in the composites. A linear relation was found between the dynamic compliance ($1/E$) and the cumulative AE counts. The dynamic compliance, $1/E$, was obtained from the hysteresis loops. The damage mechanisms in composites were classified as matrix cracking, interfacial debonding and fiber breakage. Reifsnider et al. proposed the idea that a damage variable equal to the cumulative AE counts could be used to calculate the strain energy release rate, however, no more information is reported. Eiichi Jinen [21] used the AE technique to obtain the fracture toughness quantity, G_c , in a notched short carbon fiber reinforced nylon 66 composite or CFRTP under monotonic tensile test. CFRTP stands for

carbon fiber reinforced thermosoftening plastic. Jinen found two knees in the plot of cumulative AE counts vs. displacement that he related to the initiation of a stable crack growth. Jinen mention that this damage initiation cannot be detected by simple observation. Qing et al. [23] used the AE technique to monitor the progression of damage in notched specimens under monotonically tensile test. The specimens were made of carbon fiber reinforced thermosoftening plastic (CFRTP). Qing et al. proposed a relation between the cumulative AE energy (AEE) and the stress intensity factor (k) as $AEE = C' \cdot K^m$ where C' is a coefficient that depends if the analysis is for plane stress or plane strain. Exponent m was found to be 4 for this application. The experimental values of cumulative AE energy and the predicted values using the above equation showed very good agreement.

Garg et al. [22] studied the progress of damage in graphite-epoxy laminates in four-point bending test using the AE technique. Garg et al. listed the damage mechanisms that cause AE activity as: fiber fracture, matrix fracture, fiber-matrix debonding, fiber pullout, and interplay delamination. It is also mentioned that artifacts such as rubbing of free surfaces could generate AE activity and the presence of moisture in the composite samples could attenuate the AE response. Garg et al. observed that the crack density and the total AE counts vary linearly with loading strain. They also observed that the characteristics of the AE signals are different for transverse cracking (AE response is continuous) and for delamination (AE response is discontinuous). Garg et al. proposed a relation between the cumulative number of AE counts (N) and the strains (ϵ) as $N = B \cdot \epsilon \cdot \ln(\epsilon/\epsilon_0)$ where B is a constant of proportionality and ϵ_0 is a threshold strain below which no counts are observed.

Kaya [31] used the AE technique to monitor the progress of damage in woven mullite fiber-reinforced alumina ceramic matrix composites under tensile load with the

purpose of identifying the damage mechanisms. In addition, Kaya studied the effect of the porosity in the strength and the AE activity, finding that the higher the porosity level the lower the strength in tensile loading. Kaya concluded that the fiber debonding events have the lowest energy levels, matrix cracking events have moderate energy levels and fiber fracture events have the highest energy levels and observed that the fiber-fracture events occurred regularly (i.e. two fiber bundles every 10 seconds). Morscher et al. [18] monitored the progress of damage in 2D woven Sylramic-iBN and Hi-Nicalon in CVI SiC matrix under monotonic and loading-unloading tensile tests using the AE technique. Morscher et al. measured the matrix crack density by counting the number of cracks over 10 mm in the gage section and dividing by the length of the sample. It is mentioned that the normalized cumulative AE energy is an excellent measure of the relative matrix crack density and a good estimation of the crack density can be calculated by multiplying the final crack density (measured from the sample after failure) by the normalized cumulative AE energy.

Wang et al. [33] studied the progress of damage in a 2.5 D C/SiC composite under monotonic and loading-unloading tests using the AE technique. Wang et al. noticed that the AE activity, in the form of cumulative AE energy, initiated before the nonlinearity region of the stress-strain curve due to the propagation of processing-induced matrix cracks. Starting at 50 MPa where the nonlinearity initiated, and up to 200 MPa an intense AE activity was observed, decreasing above 200 MPa until failure. The intense AE activity is associated to large bridged matrix cracks and debonding/sliding at the interface. Above 200 MPa until failure, the stress-strain curve is quasi linear indicating matrix cracking saturation with the yarns supporting all the load alone. Micrographic analysis showed cracks perpendicular to the loading direction and revealed frequent fractures of the yarns

in the crossover areas. Lomov et al. [35] monitored the AE activity during tensile loading of a 3D non-crimp orthogonal woven carbon/epoxy composite. Lomov et al. found that the cumulative AE energy correlate with the initiation of damage in the composite as observed in the change in slope of the curve cumulative-AE-energy vs. strain. The first change in slope correlates with the initiation of cracks in the direction normal to the direction of loading, and the second change in slope correlates with the initiation of cracks in the longitudinal direction. The peak frequency of the AE events did not correlate with any of the damage mechanisms as it was observed in similar studies.

Use of AE technique to monitor the damage in $\text{SiC}_f\text{-SiC}_m$ composites have been reported. Lissart et al. [24] study the mechanical behavior of SiC/SiC minicomposites under tension and monitored the AE activity during the test. Lissart et al. found that the cumulative number of AE counts corresponded well with the stress-strain curve mentioning that the matrix cracking saturation was identified by the transition between AE regimes (e.g. change in slope in the cumulative AE counts-deformation curve). Also, Lissart et al. proposed a fracture statistic-based model to predict the stress-strain curve, where matrix cracking and fiber failure is modeled using Weibull's equations of failure probability. Surgeon et al. [25] monitored the AE activity of a Tyrano silicon carbide (SiC)/barium-magnesium aluminosilicate (BMAS) matrix composite during tensile testing. Surgeon et al. concluded that the cumulative number of AE events can be used to monitor the progress of damage in ceramic-matrix composites. It is also suggested that AE characteristics such as event duration and energy could be used to differentiate between damage modes. Morscher [29] studied the behavior of a SiC/SiC woven composite panel with Sylramic fibers, in cyclic loading-unloading tensile test and the AE technique was used to monitor

the progress of damage in the material. Morscher mentioned that the normalized cumulative AE energy and the relative number of matrix cracks are directly related. The stress-dependent matrix crack distribution is calculated by multiplying the final matrix crack density (measured from the specimen at the end of the test) and the normalized cumulative AE energy.

Nozawa et al. [17] studied tensile, compressive, and in-plane shear failure behaviors of nuclear grade CVI $\text{SiC}_f\text{-SiC}_m$ composite. The progress of damage in all three tests were monitored by plotting the cumulative AE energy in the stress-strain curve. They found that due to strong frictional stress at the fiber/matrix interface, AE signals corresponding to matrix cracking occurred prior to the proportional limit stress or PLS. Nozawa et al. mentioned that it is possible that AE signals with a frequency of 130 kHz correspond to fiber sliding and AE signals with frequency of 260 kHz corresponds to matrix cracking. Gyekenyesi et al. [14] used an Acousto-ultrasonic (AU) technique to monitor the progress of damage of a $\text{SiC}_f\text{-SiC}_m$ composite laminate during loading-unloading tensile cycles. The AU technique consist of two ultrasonic sensors placed at certain distance from each other and attached on the surface of the sample. One ultrasonic sensor sends an ultrasonic pulse on the surface of the sample and the other sensor detects the signal (ultrasonic wave) that passed through the material. The sensor detecting the ultrasonic pulse works similarly to a sensor in the AE technique. Gyekenyesi et al. mentioned that the primary contributors to the non-linear behavior of the composite are the transverse matrix cracks, which are perpendicular to the loading direction. It is also mentioned that the interface works as an energy absorber, dissipating energy during the progress of damage. Gyekenyesi et al. found that the cumulated AE energy correlates with

the amount of matrix cracking in the transverse direction of the sample. It was found that the change in slope in the plot cumulative AE energy vs. strain, which is a change in rate, is evidence of matrix crack saturation.

Fast Fourier Transformation (FFT) method has been used to analyze the AE data to find a correlation between waveform parameters and damage mechanisms in composites. Dzenis et al. [27] used the AE technique to monitor the progress of damage in laminated panels made from Hexcel T2G-190-12-F263 graphite-epoxy unidirectional prepreg tape, during tensile loading. A transient analysis of the AE waveforms was conducted by finding the frequency spectra of randomly selected waveforms by FFT analysis. Three types of waveforms were identified during the analysis. One having low amplitude (A), one having medium to high amplitude (B) and one having long rise times (C). The three types of waveforms appeared simultaneously during the test. Type A waveforms were related to matrix cracks, type B to fiber breakage and type C to macrodamage development. Ramirez-Jimenez et al. [30] performed tensile test on glass/polypropylene composites and used the AE technique to monitor the progress of damage. The AE waveforms were analyzed using the FFT to obtain the frequency spectrum. It was assumed that the waveform can be represented by the highest power frequency in the frequency spectrum. In this way, the different damage modes can be identified, e.g. an event with a highest power frequency of 100 kHz represents a fiber/matrix debonding and an event with two highest power frequencies is related to fiber breaking, for the composite studied.

The Unsupervised Pattern Recognition (UPR) method has been used to cluster the AE data with similar AE parameters and relate them to damage mechanisms in composites. Pappas et al. [26] analyzed AE data obtained from a quasistatic tensile test of a 2D carbon-

carbon laminate. The samples were cut out from the laminate and a hole was drilled at the center. Following the experimental work, Pappas et al. used the UPR method to classify the data in clusters, with each cluster representing a damage mode. The k-means validation criteria was used and five AE descriptors: amplitude, rise time, energy, duration and counts. The optimum solution resulted in five clusters, each of one representing one damage mode. Cluster 1 was associated to short fiber/matrix debonding, cluster 2: matrix cracking including intralaminar matrix cracking, cluster 3: single fiber failure and long fiber/matrix debonding, cluster 4: frictional sliding and fiber pullout, cluster 5: multifiber failure.

Moevus et al. [32] used the AE technique to monitor the process of damage of SiC_f/[Si-B-C] composites in tensile loading and analyzed the AE data using the UPR method with the objective of identifying the damage modes. Moevus et al. used as AE descriptors the log(risetime), log(energy), average frequency, rise frequency between others, and as validation criteria used the k-means and Davies-Bouldin (D&B) index (R). As a result, Moevus et al. found that the global AE activity is in good agreement with the observed damage mechanisms which can be considered as cracks (subdivided in four types of cracks), debonding, fiber fracture and yarn fracture. Loutas et al. [15] monitored the progress of damage in carbon/carbon woven reinforced composites using the AE technique. The AE data was later analyzed using the UPR method to identify damage modes. The AE descriptors used were the rise angle, load (parametric), reverberation frequency and amplitude. As clustering validation criteria Loutas et al. used k-means and Davies-Bouldin (D&B) index (R). Four clusters corresponding to four damage modes were identified: matrix cracking, interfacial phenomena (debonding and fiber pull-out), thermal stress relief (matrix friction and fiber push-in) and fiber failures (single fibers and fiber

bundle failures). Loutas et al. concluded that the damage mechanisms working in a material can be revealed by analyzing AE data using the UPR method.

Methods such as the wavelet transform, and modal analysis has been used to analysis the waveforms of the AE signal in composites. Ni et al. [28] studied the fracture process of a single carbon fiber composite (sfc) embedded in epoxy when loaded in tension and used the AE technique to monitor the progress of damage. Four loading-unloading cycles were performed on the sfc specimen. Ni et al. found that the number of AE events and the number of broken fibers corresponded very well in each cycle. They also found that the frequency is a better parameter for waveform analysis than the amplitude. Using the wavelet transform method, Ni et al. determined the range of peak frequencies for the failure modes of matrix cracking (<100 kHz) and carbon fiber break (400 to 450 kHz). Breeded et al. [36] used the AE technique to monitor the progress of damage in C/C-SiC composites under tensile load and then applied the modal AE approach to analyze the waveforms. The cumulative AE energy was used to analyze the stress-dependent damage accumulation and it was observed that the AE activity increased in composites as the fiber angle increased. It was found that most of the high energy AE events occurred at high stress levels in contrast with SiC/SiC composites where high energy events occur early in the test. Breeded et al suggest that a better identification of the different damage modes could be possible by using in situ nano-CT imagery and as an alternative to AE technique the measurement of the electrical resistivity could be used for damage monitoring in the sample.

More than one method of analysis of AE data has been used simultaneously in composites. Morscher [19] used the AE technique to monitor the progress of damage in

SiC_r-SiC_m composites under monotonic and loading-unloading tensile tests. Then Morscher used the modal AE approach to analyze the waveforms in order to relate the AE waveforms and the damage source, mentioning that the extensional and flexural modes of the waveform are important to identifying the source of damage. After a Fast Fourier transform (FFT) analysis, Morscher suggests that events with high and low amplitude, loud and soft events respectively, could occur early, and soft events at high strains (>~0.65%) correspond to fiber failure and/or interlaminar cracking. Morscher mentions that the change in slope at ~0.4% in the stress-strain curve corresponds to matrix-crack saturation and that is difficult to separate events corresponding to matrix cracking from interphase events. Morscher also suggests that the first waveforms with predominantly extensional mode correspond to matrix microcracking and waveforms with large flexural components occurring close to failure correspond to fiber fractures. It was found that the speed of sound through the sample decreases as the strain increases and is related to the reduction in the modulus of elasticity.

Cuadra et al. [34] monitored the progress of damage in a glass fiber reinforced polymer (GFRP) composite in tensile fatigue using what Cuadra et al. called a hybrid non-destructive testing system that consists of three non-destructive techniques (NDT) running simultaneously: AE, Digital Image Correlation (DIC) and Infrared Thermography (IRT). In addition, the UPR method was used to analyze the AE data, evaluating the clustering procedure with the D&B and τ criteria and the FFT method was applied to find the peak frequency of the AE signals. Because of the UPR analysis, two clusters were identified. Cuadra et al. suggested that one cluster, with higher risetime and lower peak frequency signals, may be associated to matrix-dominated failure. The second cluster, with lower

risetime and higher frequencies, may be associated to fiber-dominated failure process. Cuadra et al. also found that the AE activity, such as the counts and the cumulative energy, and the increase of temperature with the applied load, offer evidence of the progress of damage in the composite.

Maillet et al. [16] used the AE technique and the acousto-ultrasonic technique to monitor the progress of damage in a SiC/SiC minicomposite under tensile loading. By using the acousto-ultrasonic technique the wave velocity was measured during the test, finding that the wave velocity decreases when the strain increases. The UPR method was used to analyze the AE data resulting in two clusters. One cluster is identified with matrix cracking (at strains $<0.6\%$) and fiber failures (at strains $>0.6\%$). The other cluster is identified with interfacial phenomena, including debonding and frictional slip at the fiber/matrix interfaces. The validation criteria used was Davies-Bouldin index and Silhouette. Maillet et al. found that there was a very good agreement between the estimated number of cracks and the number of sources at strains $<0.6\%$. Similar agreement was observed between the number of fiber failure and the number of sources at strains $>0.6\%$. Maillet et al. defined a damage parameter D as $D(\epsilon) = 1 - E(\epsilon)/E_0$, where ϵ is strain, E_0 is the initial modulus of elasticity and $E(\epsilon)$ is the secant elastic modulus extracted from the hysteresis plot from the loading-unloading tensile cycle.

McCrary et al. [71] studied the progress of damage in a carbon fiber composite panel under buckling using the AE technique. Afterward, the AE data was analyzed following three methods: Artificial Neural Networks (ANN), Unsupervised Waveform Clustering (UWC) and Measured Amplitude Ratio (MAR). The ANN method consists of first an UPR analysis of the data used to train a self-organizing map (SOM) and then used

to find the optimum number of clusters, in this case two. The UWC is an Unsupervised Waveform Clustering analysis used to group the peak amplitude of the waveforms from the AE data, resulting in this case in two clusters as well. The MAR method uses the amplitude of the extensional and the flexural components of the waveform to calculate a ratio which is the quotient of the extensional amplitude over the flexural amplitude. According to McCrory et al. the flexural component is a result of an out-of-plane movement of the structure, i.e. during delamination, and the extensional component is an in-plane movement of the structure, i.e. due to matrix cracking. The data was grouped in two clusters, one for the $MAR > 1$ and one for $MAR < 1$. McCrory et al. concluded that the three methods classified the AE data in two clusters and correlated very well the progress of damage in the carbon fiber composite panel.

The AE technique has been used to monitor the progress of damage in applications other than composites or composites that are made of ceramic and non-ceramic components. Weng et al. [73] used the AE technique to study the progress of damage in a thermotropic liquid crystalline co-polyester with and without fiber glass reinforcement material. The notched specimen was tested in tensile cyclic loading and it was observed that the cumulative number of events increased exponentially close to failure. Brendel et al. [74] monitored the AE activity in a SiC monofilament reinforced copper under tensile load. Brendel et al. concluded that the source of the AE activity was mostly fiber/matrix debonding in the samples with C/SiC interface. Ohtsu et al. [75] studied the progress of damage in structural concrete under uniaxial compression using the AE technique, with the purpose of estimate the damage without having information of the original conditions of the concrete. Masayasu et al. calculates a relative modulus ration E_0/E^* that represents the

evolution of damage in the material. E^* is the modulus of elasticity of the material without damage. E_0 is calculated using a linear approximation as function of a variable “a” which is obtained from the expression $N_h = C \cdot V^a \exp(bV)$ where N_h is the cumulative AE hits, $V(\%)$ is the stress level, C is an integration constant and b is a parameter typically very small. Masayasu et al. concluded that this method could be used to estimate the level of damage due to weak cementation of inadequate hydration of concrete however is not recommended for the case of hardening.

Zhou et al. [76] studied the progress of damage of 8 wt% Y_2O_3 - ZrO_2 (8YSZ) ceramic coating using the AE technique and digital image correlation under uniaxial tension. Zhou et al. concluded that the AE activity correlate very well with the failure mode of the ceramic coating and mentioned that the cumulative damage can be defined “as a ratio of the collected AE events in the vertical cracking stage and the total AE events”.

Ji et al. [77] used the AE technique to monitor the damage evolution of granite under uniaxial compression, founding a good correlation between the AE count rate and the stress-strain curves of the material. Ji et al. mentioned that the cumulative AE counts could be used to describe the evolution of damage of granite and a damage variable D can be defined as the rate of cumulative AE counts (Ω) and the total cumulative AE counts corresponding to the final failure of the specimen (Ω_m), $D = \Omega/\Omega_m$. Ji et al. also mentioned that an alternative approach is to express the damage variable using a Weibull distribution density function, in the form: $dD/dF = \varphi(F)$ where F is the random distribution variable of the Weibull distribution and $\varphi(F)$ is the Weibull distribution density. Finally, Ji et al. use the expression for the effective stress as in [39] to calculate the stresses (σ) as function of D and the strains (ϵ), $\sigma = E_0 \cdot \epsilon(1-D)$ where E_0 is the initial modulus of elasticity. Ji et al.

concluded that the strains calculated using the damage variable, D , calculated by both method (AE and Weibull) resulted in similar predicted stresses however these values were overpredicted compared to the experimental data. An exception was the data of the stress-strain curve close to failure where the damage variable calculated by the Weibull approach predicted very well the experimental stress while the damage variable calculated by AE counts under predicted the stresses.

Intermediate and high temperature application of AE technique have been reported in composites. Morscher [78] studied the strength degradation of a woven Hi-Nicalon fiber, BN-interphase, melt infiltrated (MI) SiC-matrix composite in tension and at temperatures of 1233 K and 1088 K in air. The location of high energy events in the gage zone was obtained successfully, the high energy events were related to matrix cracking, and the cumulative AE energy represented the progress of damage in the material better than the cumulative AE events. Morscher found embrittled fibers in the samples tested at high temperature, which calculated rupture stress was lower (~75%) than the correspondent rupture stress of a fiber tested at room temperature.

Momon et al. [12,79] studied the response of C_f /[Si-B-C] and SiC_f /[Si-B-C] composites at medium to high temperature when loaded in static fatigue tests, and used the AE technique to monitor the progress of damage in the composite. The range of temperatures was 973 K to 1473 K for the C_f /[Si-B-C] composite and 723 K to 773 K for the SiC_f /[Si-B-C] composite. Momon et al. proposed the use of a coefficient, RAE, to predict the residual fatigue life of the composite. The proposed coefficient is obtained using the AE energy by the expression $RAE(t) = (1/E_{loading}) \cdot (\Delta E / \Delta t)$ where t is time, $E_{loading}$ is the final cumulative AE energy, ΔE is the increment of cumulative AE energy during the

increment of time Δt . It was found that RAE decreases from the beginning of the fatigue test until a minimum value is reached, after this RAE start increasing until failure of the composite. Momon et al. proposed the use of the coefficient RAE as a criterion to estimate the remaining life of the composite. The UPR method was used to analyze the AE data using as validation criteria the Davies & Bouldin criterion, resulting in an optimum solution of four clusters named A (high energy, high duration and high amplitude AE signals), B (lower energy, higher risetime/duration ratio and higher frequency AE signals when compared to A), C (shortest rise time, low amplitude and low energy AE signals) and D (longest rise time and low energy AE signals). The damage mode associated with signals from cluster A were big matrix cracks for signals detected at the beginning and yarn failures for the signals detected at the end of the test. Signals from Cluster B were associated to matrix cracks in the transverse yarns and the B signals detected at the end of the test were associated to fiber breaks. Signals from cluster C were detected at the beginning of the test and are associated to matrix cracks in the longitudinal yarns. Signals from cluster D were associated to fiber-matrix interfacial debonding.

Similar analysis of RAE coefficient was made by Maillet et al. [13] in $\text{SiC}_f/[\text{Si-B-C}]$ composite in fatigue test and at temperatures of 673 °K to 773 °K. In another work, Maillet et al. [80] studied the attenuation of AE signals in $\text{SiC}_f/[\text{Si-B-C}]$ composites under static tensile fatigue test at temperatures of 723 °K to 773 °K. Maillet et al. used two AE sensors located at opposite sides of the rectangular sample, to sense the AE energy emitted by the material during testing. Maillet et al. calculated a coefficient $R(n)$ which is the logarithm of the rate of AE energies received by the sensors, and plotted $R(n)$ vs. time. $R(n)$ is defined by $R(n) = \ln (E_1(n)/E_2(n))$ where E_1 and E_2 is the AE energy detected by

AE sensors 1 and 2 correspondingly. The AE source is represented by n . The slope of the resulting curve was called attenuation coefficient, $C_{\text{Attenuation}}$. Maillet et al. observed that $C_{\text{Attenuation}}$ increased mostly during the first half of the tests and the corresponding AE events were associated to matrix crack openings. In the second half of the test and until failure $C_{\text{Attenuation}}$ reached a plateau. The authors suggest that the use of coefficient of attenuation, $C_{\text{Attenuation}}$, could be used as a tool for lifetime prediction.

“Damage Mechanics (DM) is the study of the mechanisms involved in the deterioration of the material (the damage) when subjected to loading” [39]. The mechanics of damage of a material can be explained using mechanical variables defined at a mesoscale level. These mechanisms are the accumulation of microstresses and the growth of microcracks and microvoids that develop cracks in the material [39]. In DM a variable of damage or simply damage, represented by D , is defined as the quotient of the area in the plane normal to the load containing the microcracks or microvoids and the total cross section area [39]. A similar definition of damage is found in the work of Talreja [81]. A direct application of the definition of D can be obtained for the case of uniaxial loading such as a tension test [39]. The damage, D , can be formulated in three dimensions by introducing an internal state variable defined in the frame of the thermodynamics of irreversible processes and based in the strain equivalence principle [38,39,82]. This approach of the study of damage is known as Continuum Damage Mechanics (CDM) [37,39,83]. Therefore, CDM is a DM approach developed at the meso/macroscale that considers the material as a continuous medium [37,83]. CDM attempts to measure the mechanical damage, which causes the variation of the elastic coefficients, by introducing a damage variable, which is function of state variables, such as strain, stress and

temperature. In the CDM approach, as the material is damaged, the mechanical properties of the material deteriorate following a process that can be represented by a mathematical function or damage evolution law. In the case of a stress derivation, the observable state variables are chosen to be the stress, the temperature, and a thermodynamic potential based on the Gibbs free energy [37]. The CDM approach has been used successfully to predict the evolution of damage of SiC composites [37,38,84,85,86] and will be used in this work to predict the strains obtained in uniaxial loading.

CHAPTER 3

EXPERIMENTAL SETUP

Three experimental setups were used, a RT open-end internal pressure setup, a HT solid-surrogate internal pressure setup and a quenching setup. The composite tubes were provided by the company General Atomics with headquarters in California.

3.1 THE SiC_f-SiC_m COMPOSITE TUBING

The SiC_f-SiC_m composite tubing was fabricated at General Atomics following a chemical vapor infiltration (CVI) technique [50,87,88] using Hi-Nicalon type S fibers and a pyrolytic interphase. A hoop biased composite was used for the RT open-end bladder tests and a more balanced architecture was used for the samples tested at high temperature. The dimensions of the SiC_f-SiC_m composite tubes are shown in Chapter 5. A set of open-end samples (named A through I) were used in the burst tests and HT tests. A set of close-end samples were used for the quenching test. In the case of the quenching test, the SiC_f-SiC_m composite tubing had an end-plug sealed using the GA-HSiC joining method (GA patent US 20130266363 A1).

3.2 RT OPEN-END SETUP

The high pressure is generated using a piston-type hydraulic pressure generator (Model 37-6-30 from High Pressure Equipment Co. Erie PA) that feeds hydraulic oil into a flexible rubber tubing being placed within the Si_f-SiC_m sample tube. A unique test rig was designed to seal the ends of the rubber tubing while pressurizing it up to 200 MPa (2000 bar). The expanding rubber tubing confined by the Si_f-SiC_m sample tube exerts a

controlled uniform internal pressure to the $\text{Si}_f\text{-SiC}_m$ sample [89]. Strain gauges and 3D-DIC were used to measure the strains on the outside surface of the sample and a pressure sensor was used to measure the internal pressure. A schematic of the RT open-end bladder test rig is shown in Figure 3.1. Because of the special design of the pressure rig, the sample was not loaded axially, only in the hoop direction. The hoop stress in the $\text{SiC}_f\text{-SiC}_m$ tube was calculated at the outer diameter using thick-walled cylinder theory of the case of internal pressure only [90] using the equation:

$$\sigma_h = P \frac{2r_i^2}{r_o^2 - r_i^2} \quad (1)$$

Where:

σ_h : hoop stress on the outer surface

P : internal pressure

r_i : inner radius of the sample

r_o : outer radius of the sample

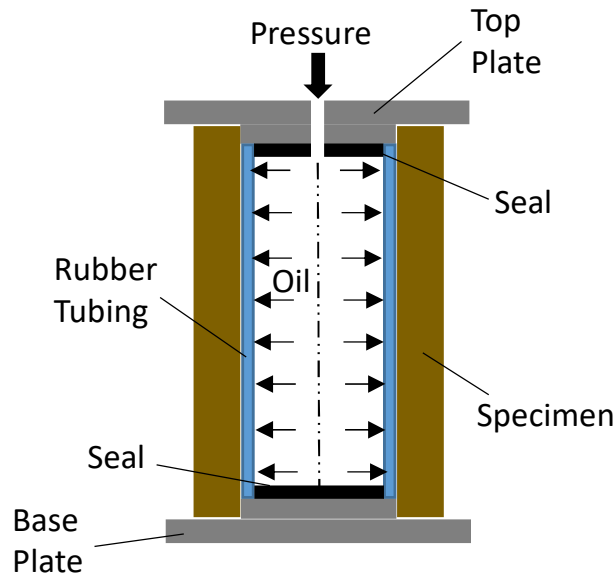


Figure 3.1: Schematic of RT open-end internal pressure rig.

3.3 HT SOLID SURROGATE SETUP

The proposed method uses a solid tubular surrogate, made of alumina, to internally pressurize a $\text{Si}_f\text{-SiC}_m$ composite nuclear fuel cladding (the sample). The surrogate is inserted in the cladding and it is bonded using a thin layer of ceramic adhesive in between. In order to generate the internal heating of the assembly, a Nernst glower is used as heater and is inserted in the surrogate as shown in Figure 3.2. The solid surrogate is chosen to be of a material with a coefficient of thermal expansion (CTE) that is larger than the CTE of the SiC sample, this is the case of alumina. When heated, a thermal gradient occurs through the thickness of the surrogate and cladding with a temperature profile having a maximum temperature in the inner surface of the surrogate and decreasing in the radial direction, reaching a minimum at the outer surface of the cladding [91].

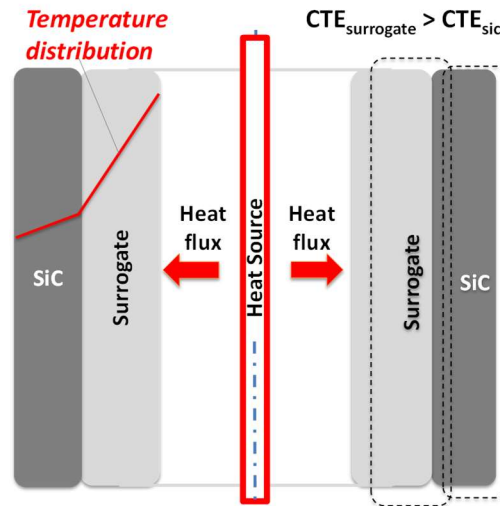


Figure 3.2: HT Internal pressurization of SiC cladding.

As a consequence of the different rates of expansion between surrogate and sample and the temperature gradient across the thickness of the assembly, the surrogate will exert a normal pressure and shear stress on the inner surface of the sample through the thin ceramic adhesive layer, resulting in a biaxial state of stresses in the center portion of the

SiC sample as shown in Figure 3.3. Hoop stresses are induced in the sample as a result of the internal pressure, and axial stresses are induced due to the shear stresses applied on the inner surface of the sample, as a consequence of the axial expansion of the surrogate. Using this approach, it is possible to replicate thermal-mechanical conditions such as temperatures, temperature gradients, PCMI, and internal pressure, similar to the conditions that might be expected during accidents such as LOCA and RIA.

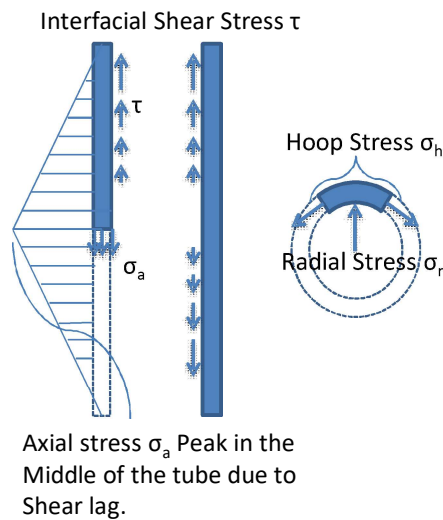


Figure 3.3: Stresses on the inner surface of sample.

The main component of the test apparatus is the test chamber (Figure 3.4a) designed for the high temperature experiment. The test chamber is a 51 x 51 mm cube with aluminum frame and quartz windows to allow the acquisition of images of the sample using CCD cameras. A picture of the chamber taken during a high temperature test is shown in Figure 3.4b. In addition, the test chamber has openings to accommodate instrumentation such as thermocouples and electrical leads, and orifices to supply air or other gas to the chamber. The surrogate of the SiC sample is made much longer than the sample in order to attach an AE sensor far from the sample which is at high temperature, preventing the AE sensor to be damaged. The SiC sample is placed at the center of the chamber, being hold by the

surrogate which passes through a hole in the floor of the chamber. Another feature of the test apparatus is a sliding arm that is used to displace the heater (the Nernst glower) into position, inside the sample-surrogate assembly.

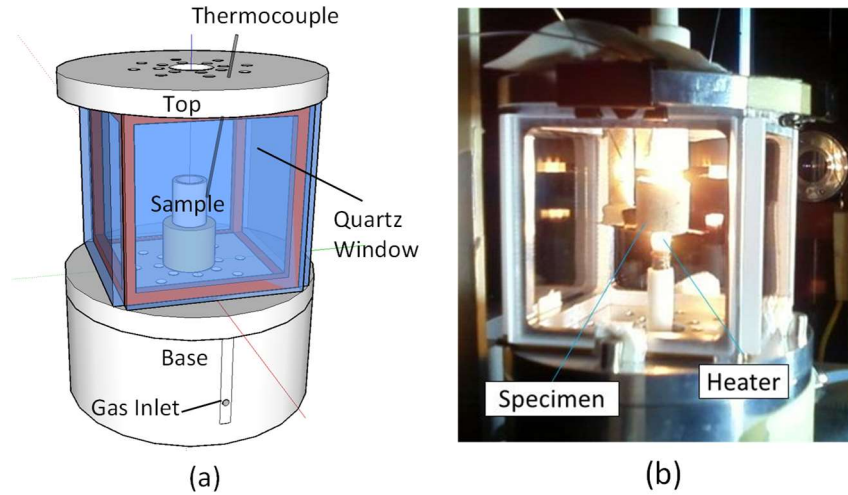


Figure 3.4: Conceptual design of the HT chamber (a), sample in chamber (b).

Figure 3.5 shows a schematic of the high temperature apparatus and equipment. As can be seen, the AE sensor is located at the bottom of the long surrogate where the temperature is lower than its maximum temperature allowed. The CCD cameras are located at some distance of the chamber and aiming to the sample. The thermocouples are inserted through openings in the chamber to measure temperatures on the outer surface of the sample and between the sample and surrogate. A piece of Kanthal is used to hold the heater from the ends. The Kanthal is attached to copper rods, serving as a heat-conduction bridge between heater and rod, keeping the area close to the end of the rod cool. The wires that connect the heater and the copper rod are made of Platinum/Rhodium which are capable of withstanding temperatures as much as 2073 K without melting and have good electrical conductivity. To operate the heater, which is a Nernst glower, an external variable transformer is used to supply the necessary power, and a ballast is installed in series to

compensate the variation in the resistivity of the heater that decreases fast as the temperature increases. The external wires that connect the apparatus to the electrical circuit are regular copper wires.

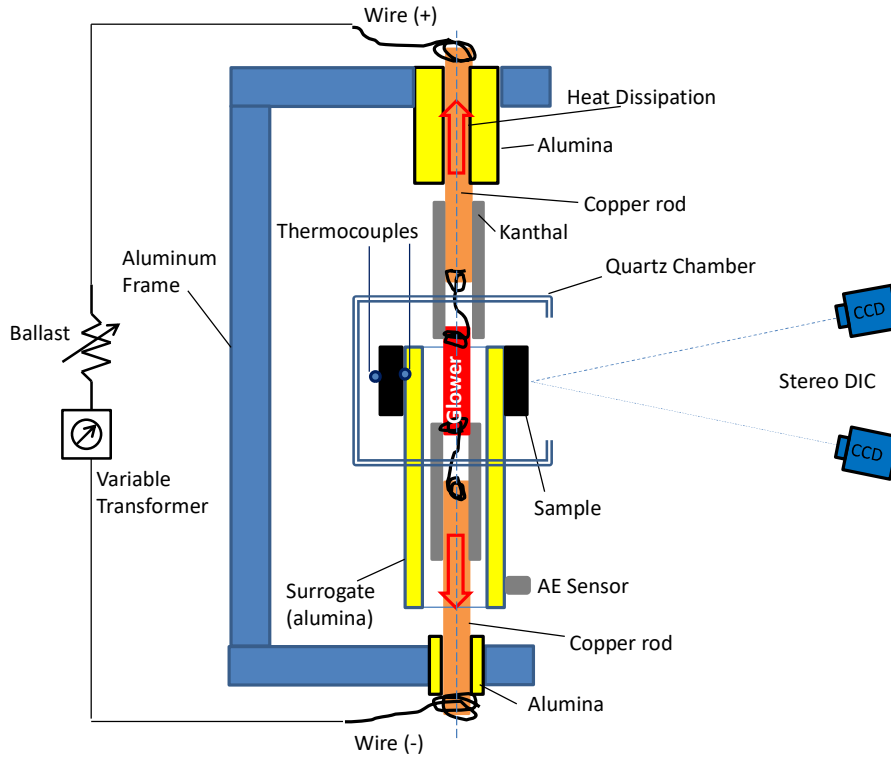


Figure 3.5: Schematic of HT apparatus and equipment.

3.3.1 NERNST GLOWER HEATER

The heater is a ceramic rod (O.D. 3.48 mm and 28 mm long) heated to incandescence made of Ytria (3mol) Partially Stabilized Zirconia from Ortech Advanced Ceramics. The heater is a Nernst glower, invented by Walther Nernst [92] and used in the Nernst lamp as the glower. The Nernst glower is a good conductor of electric current at high temperature, above 873 K, and non-conductor at room temperature. The Nernst glower must be pre-heated at around 873 K in order to start conducting electric current. When the electric current is conducted through the ceramic rod, the Nernst glower

incandesce in the open air, irradiating heat to the surrounding objects, making the Nernst glower a perfect heater. In order to pass electrical current through the Nernst glower, a fine layer of platinum paste (component metallization from Heraeus Inc.) is applied on the area close to the ends of the ceramic rod, cured at 1073 K, and then a platinum wire (Platinum - 30wt% Rhodium, O.D. 0.25 mm) of about 0.14 m in length is coiled in each end; these electrodes are connected to a variable voltage AC source. A schematic of how the Nernst glower is connected to the electrical circuit is shown in Figure 5 and picture of a Nernst glower is shown in Figure 3.6.



Figure 3.6: The Nernst glower.

In order to compensate the rapid decrease in resistance to the pass of electrical current through the heater, a ballast is connected in series to the electric circuit. The ballast is made of four 300 W incandescence bulbs connected in parallel. The ballast compensates the loss of resistivity in the circuit, as the resistance of the bulbs increases while the resistance of the Nernst glower decreases, limiting the pass of current through the circuit and as a result allows the control of temperature of the glower.

3.4 QUENCHING SETUP

During the quenching test, the sample is heated using a 15 KVA induction heater, a 25 mm (1 in.) diameter copper coil and using a Tungsten rod as susceptor with diameter of 6.35 mm (0.25 in.). The tungsten rod has an orifice of 3.175 mm (0.125 in.) to accommodate a B-type thermocouple. The sample is held using an alumina tube with a lip that fits tight in the sample, this is the main mechanism of support, and a small amount of

ceramic paste is applied outside to seal the gap between sample and alumina tube. During heating, a IRCON Modline-3 pyrometer is used to measure the temperature on the outer surface of the $\text{SiC}_f\text{-SiC}_m$ composite tube. During quenching, a K-type thermocouple is used to measure the temperature on the outer surface of the $\text{SiC}_f\text{-SiC}_m$ composite tubing, and a B-type thermocouple is used to measure the temperature at the center of the sample-susceptor arrangement. A nano-50 AE sensor is attached to the alumina tube at about 760 mm (2.5 ft.) from the sample to prevent overheating. A schematic of the setup is shown in Figure 3.7 (the induction coil is not shown).

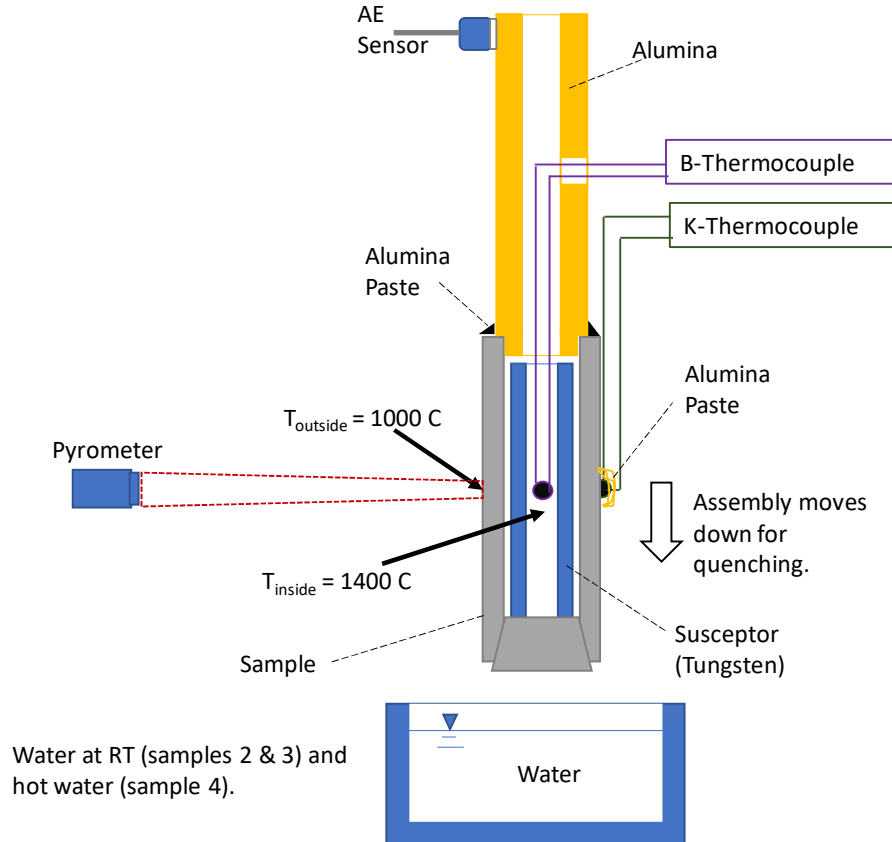


Figure 3.7: Schematic of quenching experimental setup and instrumentation.

Before quenching, the sample was held in vertical position and placed inside the induction coil, as in Figure 3.7, by an alumina support tube. In the initial position of the

sample, the bottom end of the close-end SiC_f-SiC_m composite tube is at a distance of about 0.25 m (10 in.) from a beaker full of water. The alumina tube is firmly attached to a carriage fixed to an aluminum frame. The carriage slides on a rail and can be moved up and down manually. The sample reached the target temperature in about 60 seconds following a dwelling period of about 5 minutes before quenching. When the sample reaches a steady state at the desired temperature, the carriage is moved down quickly by hand while the induction heater is turned off. The displacement of the sample from the initial position to the final position takes about 1 second. The target temperature on the outer surface of the sample during heating is 1273 °K (1000 °C). The correspondent temperature inside the tungsten susceptor is 1673 °K (1400 °C).

An image of the sample, the alumina tube and the thermocouples are shown in Figure 3.8. In Figure 3.8, “B” is the B-type thermocouple and “K” is the K-type thermocouple. Temperature data was recorded using a NI cDAQ-9172 chassis with module NI cRIO-9215 and a LabView program. The close-end SiC_f-SiC_m composite tubes were quenched from a temperature of 1273 °K (1000 °C), as measured in the outer surface of the sample, into water at RT (23 °C) and hot water (~100 °C). After quenching, the sample was allowed to cool down to ambient temperature, then was removed from the aluminum holder, placed in a hood, and let it dry for 24 hours. Once dry, the sample was prepared for internal pressure test. The internal pressure test will reveal the remaining strength of the sample.

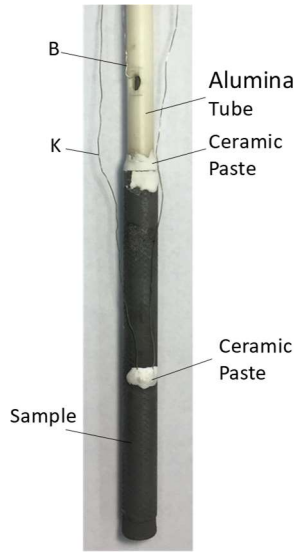


Figure 3.8: Assembly of sample.

3.5 DIGITAL IMAGE CORRELATION

The full-field strain distribution of the outside surface of the sample was captured by 3D digital image correlation (DIC) method. The arrangement of the optical components for 3D DIC is shown in Figure 3.9(a)(b). Two CCD cameras from Point Grey (GRAS-30S5M) were used for image acquisition; the CCD sensor in the camera is ICX625AL from Sony, and two high resolution fixed focal length (0.025 m) lenses (NT63-780, from Edmund Optics). The camera was placed at 0.22 m away from the sample and the angle between the two optical axes was 22° and 10° (RT and HT correspondingly). The DIC technique was not used with the quenching test. For the RT test two fluorescent lights were used to illuminate the sample, see optical arrangement in Figure 3.9(a). In the high temperature experiment two Thorlabs-LIU004 LED lights were used to illuminate the sample which was placed behind a fused quartz window (transmittance of >0.9 , from $0.28 \mu\text{m}$ to $2.0 \mu\text{m}$), see optical arrangement in Figure 3.9(b). During testing, the two CCD cameras were triggered simultaneously at 4 Hz.

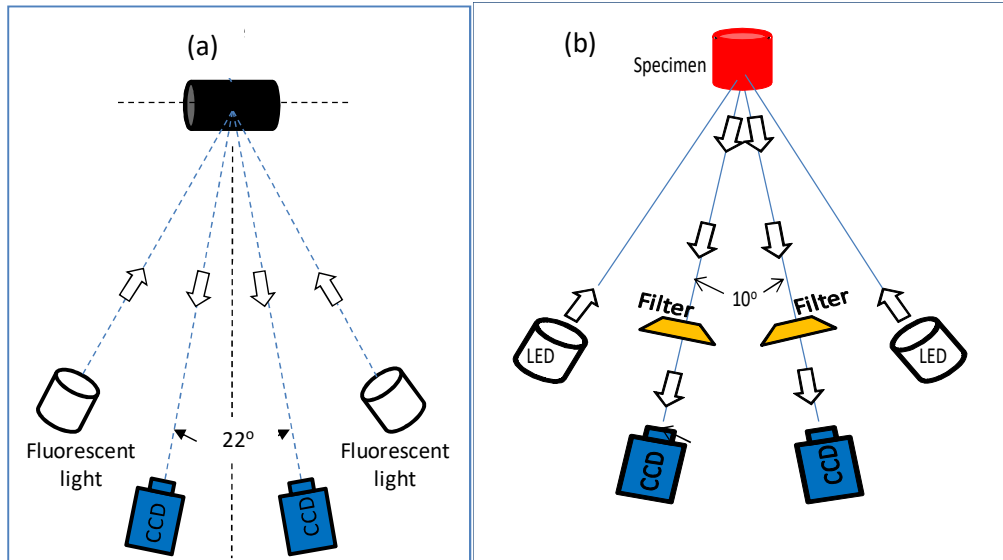


Figure 3.9: DIC optical arrangement RT (a) and HT (b).

A comparison between DIC strains and strain-gauge strains is shown in Figure 3.10 where the stress vs. strain curves correspond to an internal pressure test of a nuclear grade $\text{SiC}_f\text{-SiC}_m$ composite tube. The DIC data points are scattered compared to the data points from the strain gauges, however, follow a similar trend. The standard deviation of the DIC strains is lower than the typical DIC measurement error of $200 \mu\epsilon$, see Figure 3.10.

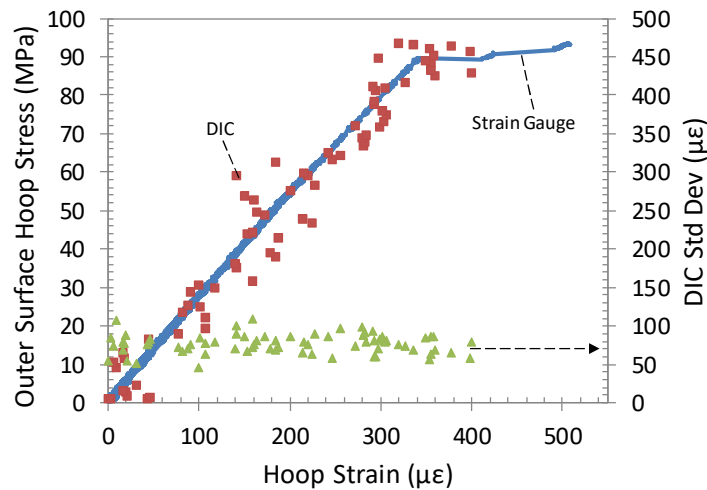


Figure 3.10: DIC vs. strain gauge strains.

3.5.1 THE SPECKLE PATTERN

In the case of RT bladder test, the speckle pattern was painted directly on the sample using flat white spray paint after the installation of strain gauges. The sample was placed in a fume hood and then the spray jet of the paint was aimed towards the sample forming an angle of about 40° with respect to the plane of the hood and from a distance of about 0.6 m from the sample. Spraying for two seconds and then turning the sample, the spray droplets drifting downwards slowly coated the sample surface. This process is repeated until a uniform speckle pattern is obtained, then the sample is air dried for 12 hours. See an image of a RT speckle pattern and the strain gauges in Figure 3.11(a). In the HT the speckle must resist the harsh conditions maintaining the initial contrast otherwise would be impossible to correlate the images. Through trial-and-error, we found a commercially available alumina spray paint (A-aerosol from ZYP-Coatings Company) which is capable of producing temperature resistance speckle pattern on the SiC and SiC_f-SiC_m composite sample surfaces. See an image of HT speckle pattern in Figure 3.11(b). The speckle pattern made of alumina spray survived a temperature of 1500 °K in the laboratory. Chemical thermodynamic calculation indicates that the SiC-Al₂O₃ interface is stable at temperature below 1800 °K [93].

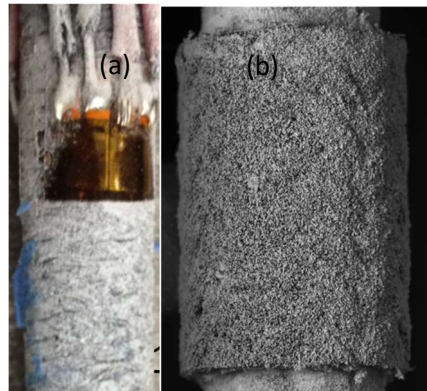


Figure 3.11: Speckle pattern on SiC_f-SiC_m composite tube at RT (a) and HT (b).

3.5.2 LIGHT FILTERING TECHNIQUE

In the case of the RT experiment, the sample was illuminated by using fluorescent light. However, for the HT experiment a special light filtering technique was used. The surface of a hot object emits radiation that depends on the material of the object, the quality of the surface (e.g. polished, ground) and the temperature of the surface. The radiation consists of beams of electromagnetic waves characterized by their wavelength. As an object increases its temperature, the electromagnetic waves extend in the direction of lower wavelengths, and when the temperature of the object is higher than 800 °K it will emit radiation in the visible range of the spectrum (0.4 to 0.76 μm) [94]. The SiC and SiC_r-SiC_m composite sample surfaces will emit visible light above 800 °K which can change the contrast of the speckle image and confuse the DIC algorithm. To overcome this problem a light filtering scheme [41] is used. This approach illuminates and images the sample through a narrow spectral window around 0.45 μm , avoiding thermal emitted photons mostly at longer wavelength. This arrangement allows the capture of images with stable surface contrast during the heating process [95].

In Figure 3.12, the spectral blackbody emissive power of a blackbody at the temperature of 800 °K and 1300 °K is plotted against the wavelength. The SiC and SiC_r-SiC_m composite samples are not perfect radiators consequently they will emit less power than a blackbody. As can be seen from Figure 3.12, a small amount of visible light will be emitted by the sample between 800 °K and 1300 °K. Most of this light will be blocked to prevent changes of brightness in the surface of the sample that could trick the cameras affecting the calculation of strains. Two 0.45 μm bandpass filters from Edmund Optics

(BP450, effective range 0.44-0.46 μm) were used in front of each camera to filter the light reaching the camera lenses.

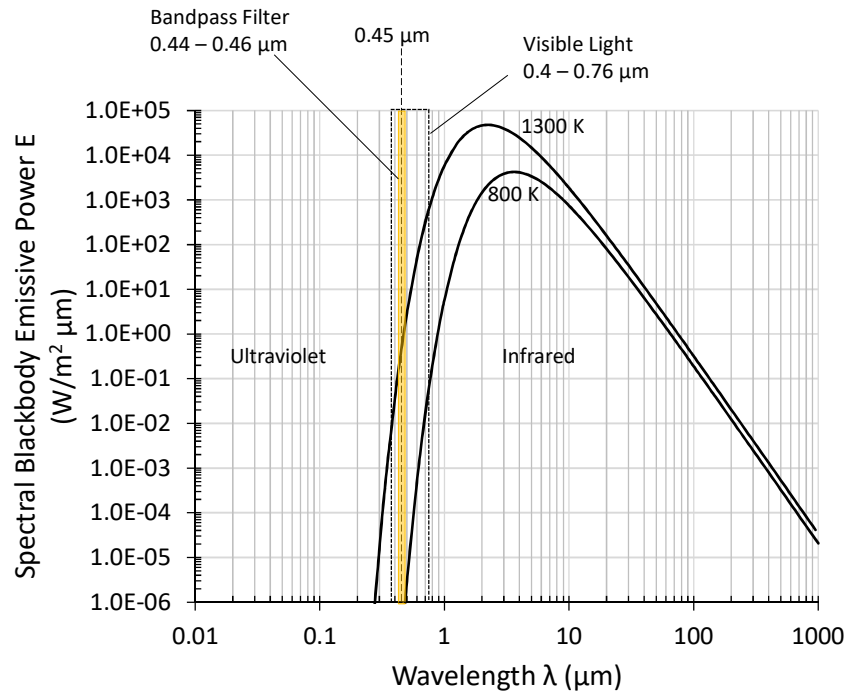


Figure 3.12: Spectral blackbody emissive power between 800 °K and 1300 °K.

CHAPTER 4

DAMAGE MECHANICS AND ACOUSTIC EMISSION

In this chapter, the definition of damage (D) is explained, and a relation between D and acoustic emission is proposed.

4.1 DAMAGE MECHANICS

A visualization of the damage in a material under loading is represented in Figure 4.1(a). The concept of a Representative Volume Element (RVE) is introduced by Lemaitre [39] in order to define the damage (similar work was published by Talreja [81]). According to Lemaitre [39], at the mesoscale, the damage of the material, consisting of broken bonds and microcavities, can be quantified by considering the intersections of all the flaws with a plane that passes through the body of interest at a point such as point M in Figure 4.1(a). The damage in a cross section of the REV at point M can be expressed as,

$$D(M, \vec{n}, x) = \frac{\delta S_{Dx}}{\delta S} \quad (2)$$

Where:

D : is the damage variable

M : is a point in the body

\vec{n} : vector representing the direction of the plane

δS_{Dx} : area of the microcracks intersecting the plane in the REV

δS : area of the RVE intersecting the plane

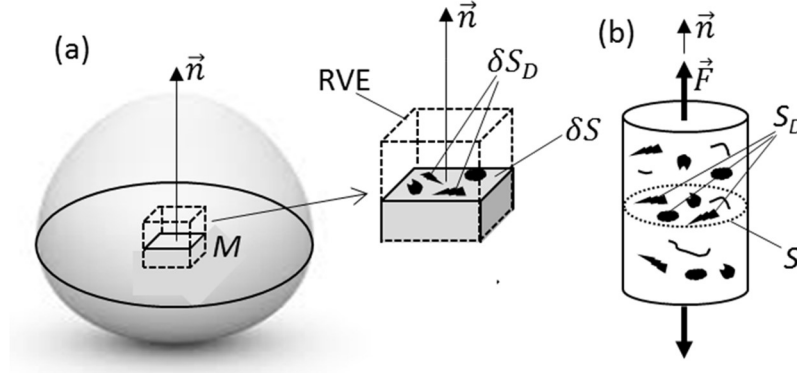


Figure 4.1: (a) Damaged body and RVE, (b) damage in a rod axially loaded.

In the case of a uniaxial loading as the one represented in Figure 4.1(b), the damage, D , can be simply expressed as,

$$D = \frac{S_D}{S} \quad (3)$$

Where, S is the cross section of the element and is perpendicular to the loading direction, and S_D is the area of the microcracks projected in the plane of the cross section. The cross section to be considered for the representation of damage of the material, must contain the largest amount of damage. The definition of effective stress, $\tilde{\sigma}$, is introduced here [39,84,82],

$$\tilde{\sigma} = \frac{F}{S - S_D} \quad (4)$$

Where, σ is the stress and is equal to $\sigma = F/S$, F is the force.

The damage model to be described in the framework of CMD, is based in the Strain Equivalence Principle. The Strain Equivalence Principle enunciates [39]: “Any strain constitutive equation for a damaged material may be derived in the same way as for a virgin material except that the usual stress is replaced by the effective stress”. Therefore, the elastic strains of an undamaged material, $D = 0$, is expressed as,

$$\varepsilon_e = \frac{\sigma}{E} \quad (6)$$

Where E is the elastic modulus of the undamaged material. And according to the Strain Equivalence Principle, the same expression is used to calculate the elastic strains of a damaged material, $0 < D < 1$,

$$\varepsilon_e = \frac{\sigma}{E(1-D)} \quad (7)$$

Or

$$\varepsilon_e = \frac{\tilde{\sigma}}{E} \quad (8)$$

The elastic modulus of the damaged material or effective modulus, can be expressed as,

$$\tilde{E} = E(1 - D) \quad (9)$$

There are different methods used to measure the damage, D , in a material. They can be summarized as [39],

- a. Direct measurement: D is obtained by calculating the area of microcracks in micrographs pictures.
- b. Variation of the elastic modulus: this can be done by conducting mechanical tests of machined samples representing different level of damage. Another method is measuring the speed of ultrasonic waves to calculate the variation of the elastic modulus.
- c. Variation of microhardness: in this method, the hardness of the material is used to obtain an expression of the variation of the damage variable D .
- d. Other methods,
 - a. Variation of density: pure ductile damage.
 - b. Variation of electrical resistance.
 - c. Variation of the cyclic plasticity response.

- d. Tertiary creep response.
- e. Acoustic emission: good to locate the damage zoned. Considered a qualitative method only.

From Lemaitre book [39], the methods considered good to measure damage in brittle and ductile materials are: elasticity modulus, ultrasonic waves, and microhardness. In addition, for ductile materials only, micrography, density, and electrical resistance are good methods as well. As mentioned by Lemaitre [39], AE is considered a good technique to locate the initiation of cracking in a sample and no relation to the damage of the material is considered other than qualitative.

4.2 CONTINUUM DAMAGE MECHANICS

In this work, for the case of the $\text{SiC}_f\text{-SiC}_m$ sample tubing, the sample is considered as a continuous media, and the variation of the compliance coefficients is a manifestation of damage as consequence of the loading acting on the sample. The manifestation of damage occurs as micro and macro cracks perpendicular to the loading direction, which is uniaxial for the case of the RT bladder test.

The CDM approach in this work, is a stress approach, following the methodology as in Chaboche [96] and Maire et al. [84], assuming the direction of the cracks is perpendicular to the load direction and assuming a plane state of stress. This has been observed during the internal pressure tests where the cracks are always perpendicular to the hoop stresses. In other words, the direction of the damage is load-dependent. There are other CDM approaches that models the composite by considering the different components to try to explain at the mesoscale the physical meaning of the damage. For example, the CDM method is used in laminates or in composites that can be modeled assuming that

behaves as a laminate (some woven or braided SiC_f-SiC_m composites can be modeled as a laminate) [38,84,97,98]. In this CDM-laminate approach, the SiC_f-SiC_m composite is assumed that is made of plies, one of the plies represents the intertow matrix and the other plies represent the tows. Another CDM approach, considers that there are three main aspects of the composite that represents the damage: matrix damage, fiber damage and interphase damage [39,86]. Each aspect responds to a different damage evolution law.

The method of CDM considers the existence of two energy potentials, a thermodynamic potential and a dissipation potential. These potentials are used to derivate the constitutive law or state law, and the damage kinetics [19,83,39]. The isothermal stress derivation of the thermodynamic potential is based in the Gibbs free enthalpy expressed as [84,37],

$$\Phi = \Phi(\sigma, D) \quad (10)$$

Where σ is the stress (state variable) and D is the damage variable. In tensorial form is,

$$\Phi = \frac{1}{2} \sigma : S^o : \sigma + \frac{1}{2} \tilde{\sigma} : \Delta S' : \tilde{\sigma} \quad (11)$$

Where $\tilde{\sigma} = \sigma - \sigma^R$. And σ^R is the residual strain induced by manufacturing processes [84]. The second order effective compliance tensor $\Delta S' = D : S^o$ with D the damage tensor and S^o the initial compliance tensor. In the expression of Gibbs free enthalpy (10)(11), damage deactivation has not been included, as compression and unloading is not considered in this work. In addition, no residual stresses are considered as well. The constitutive law is the derivation of strains,

$$\varepsilon = \frac{\partial \Phi}{\partial \sigma} \quad (12)$$

For the case considered in this work, the expression of strains simplifies to an expression similar to the expression for the effective compliance tensor as in Camus [37] but for load driven damage. In indicial notation,

$$\varepsilon_i = S_{ij}^o(1 - D_{ij})\sigma_j \quad (13)$$

Where $i,j = 1,2,6$. The subindex 1 and 2 represent the orientation of the load in hoop and axial direction while the subindex 6 represent the orientation of shear load. For example, for the case of uniaxial loading in the hoop direction, expression (13) becomes,

$$\varepsilon_1 = S_{11}^o(1 - D_{11})\sigma_1 \quad (14)$$

Here w_{11} is a damage variable. Replacing $S_{11}^o = \frac{1}{E_{11}^o}$ in expression (14) we obtain,

$$\varepsilon_1 = \frac{1}{E_{11}^o(1-D_1)}\sigma_1 \quad (15)$$

Expression (15) for uniaxial loading, has a similarity with expression (7) obtained from the definition of damage. It must be mentioned, that in the case of biaxial loading, expression (15) becomes more complex.

Now a thermodynamic force is defined which is related to the damage variable,

$$Y_i = \frac{\partial \phi}{\partial w_i} = \frac{S_{ii}^o \sigma_i^2}{2} \quad (16)$$

At this time, it cannot be inferred that the damage in the different load directions are coupled because the analysis is based in the application of unidirectional forces. Therefore, the evolution of the damage variable is defined as,

$$D_i = f_i(Y_i, Y_{0i}) \quad (17)$$

In other words, the function that represents the evolution of damage of the composite is expressed in terms of thermodynamic forces and reference forces (Y_{0i}), obtained from the mechanical tests. The damage function can be obtained from tensile,

compression and torsion tests, or can be obtained directly from AE parameters such as hits, energy or amplitude [76].

4.3 ACOUSTIC EMISSION (AE)

AE technique is being considered promising with the purpose of monitoring, identifying and classifying of damage in $\text{Si}_f\text{-SiC}_m$ composites [72,19,17,16]. Acoustic emission is the spontaneous release of elastic energy when a material undergo deformation generating transient elastic waves from localized sources within a material [99]. An example of an acoustic emission waveform is shown in Figure 4.2, where some of the parameters that characterize the waveform are shown, such as: amplitude, duration and rise time. Threshold is the reference value in decibels (dB) used by the AE software to start recording if the signal is higher than this value. In acoustic emission the unit decibel is calculated using the expression $N_{dB} = 20 \log_{10} \frac{V}{V_0}$ where V is potential in volts and V_0 is a reference potential [97].

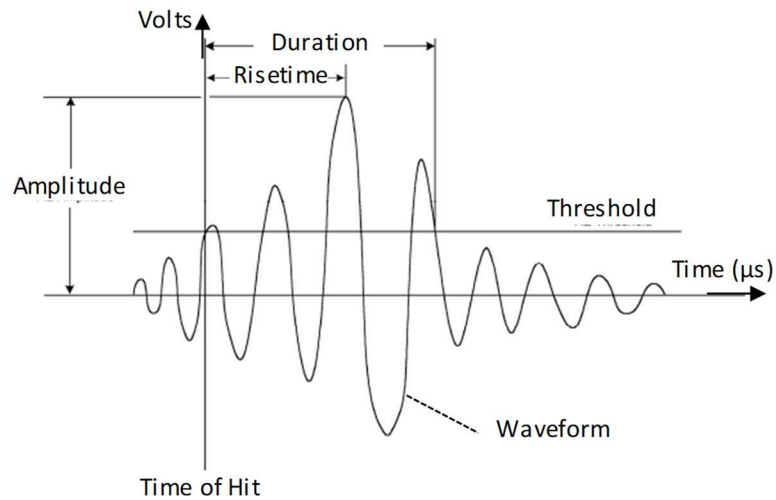


Figure 4.2: Acoustic emission waveform.

A parameter of interest is the absolute energy which is a true energy measurement of the AE event. The absolute energy is calculated using the expression $E = \frac{1}{R} \int_0^{\infty} V^2(t) dt$ where R is the reference resistance, V is voltage and t is time [96] over the duration of the waveform packet [100]. The AE event is related to the internal damage of the composite, and to each event corresponds one waveform.

The AE equipment used in this work, is a Micro-II Digital AE System (Physical Acoustics Corporation) equipped with a NANO-30 AE sensor and 60 dB pre-amplifier and the data is analyzed using AEWin software, see Figure 4.3. AE hardware parameters are PDT: 50 μ s, HDT: 150 μ s, HLT: 350 μ s. The AE signal trigger threshold was set at 54 dB, the sampling rate is set at 5 million sample/s with analog signal pre-amplified by 20 dB.

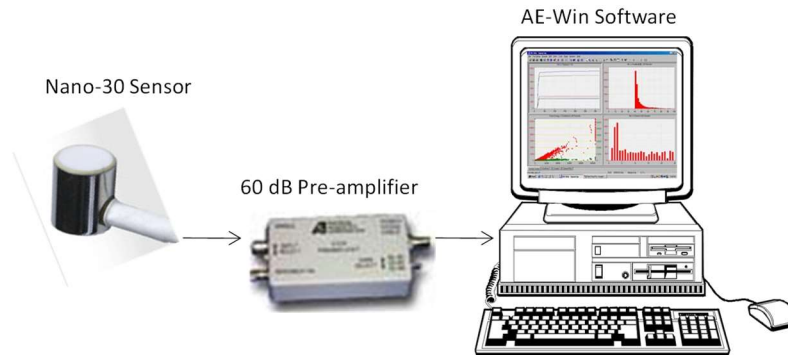


Figure 4.3: AE equipment.

In the case of RT open-end bladder test, the AE sensor will be attached directly to the sample by using a rubber band and using Vaseline as contact media. To enable the monitoring of AE in the HT solid surrogate test, the composite sample is mounted on a long surrogate tube which extends out of the hot zone. The AE sensor will be attached to the cool end of the ceramic surrogate tube which functions as a wave guide with low attenuation. In addition, a fan is used to cool the surrogate tube in order to keep the AE sensor below 434 °K.

4.4 AE ENERGY AND DAMAGE VARIABLE D

The important role of the AE energy in the discrimination of damage mechanisms was mentioned by Moveus et al. [32]. In this work, the relation of the absolute AE energy and the damage variable D (as defined in DM [39]), is studied. Some assumptions are made at this point:

1. The AE energy is the elastic energy released during a structural change in the material therefore is representative of damage and is closely related to the damage variable, D .
2. Every AE signal detected is related to a corresponding event occurring in the material, such as a crack or fiber breaking. As a result, to every event corresponds a particular AE waveform.
3. Microcracks, cracks, fiber breakings and tow failures are mechanisms of damage that contribute to the evolution of the damage characterized by the emission of elastic energy, while the mechanisms of debonding and fiber pullout are only energy dissipation mechanisms but do not contribute to the evolution of the damage variable D .
4. The amount of elastic energy emitted from a crack or fiber breaking is representative of the size of the corresponding crack or the fiber breaking.

The absolute AE energy is a true energy measurement of the AE event [100]. Normalized cumulative AE energy, N_i , has been used to show the similarity of the trend between the N_i vs. strain curve and the stress-strain curve in mechanical tests such as tensile test. It is clear that the trends of both curves are similar, therefore N_i is representative of the evolution of damage represented by the deviation of the stress-strain curve from

linearity, as in Nozawa et al [17]. Gyekenyesi et al. [14] found that the cumulative AE energy is directly related to the amount of transverse matrix cracking in a SiC/SiC 0/90 laminate composite under tensile load. Cuadra et al. [34] observed that the change of the slope of the cumulative AE energy curve corresponds to a transition in the stress/strain curve in a laminate made of glass fiber reinforced polymer under tensile fatigue loading. Qing et al. [23] tested notched samples made of carbon fiber reinforced thermosoftening plastic under monotonically tensile test proposing a relation between the cumulative AE energy (E) and the stress intensity factor (k) of the material, $E = C \cdot K^m$ where C is a coefficient that depends if the analysis is for plane stress or plane strain. Exponent m was found to be 4 for this application. Good agreement was found between predicted and experimental values of E.

Momon et al. [12,79,13] proposed the use of the cumulative AE energy to calculate the residual fatigue life of C_f /[Si-B-C] and SiC_f /[Si-B-C] composites at medium to high temperature when loaded in static fatigue tests. The residual fatigue life was represented by a coefficient RAE, obtained using the expression $RAE(t) = (1/E_{loading}) \cdot (\Delta E / \Delta t)$ where t is time, $E_{loading}$ is the final cumulative AE energy, ΔE is the increment of cumulative AE energy during the increment of time Δt . Morscher et al. [18] monitored the progress of damage in 2D woven Sylramic-iBN and Hi-Nicalon in CVI SiC matrix under monotonic and loading-unloading tensile test. Morscher et al. mentioned that the normalized cumulative AE energy is an excellent measure of the relative matrix crack density and a good estimation of the crack density can be calculated by multiplying the final crack density (measured from the sample after failure) by the normalized cumulative AE energy. Maillet et al. [80] studied the attenuation of AE signals in SiC_f /[Si-B-C] composites under

static tensile fatigue test at temperatures of 723 °K to 773 °K. Maillet et al. used two AE sensors located at opposite sides of the rectangular sample, to sense the AE energy emitted by the material during testing. Maillet et al. found a relation between the AE energy attenuation and the transverse matrix crack opening.

In this work, the cumulative AE energy is calculated using the absolute AE energy of the waveform and is expressed as:

$$CAEE_i = E_i^{AE} + CAEE_{i-1} \quad (18)$$

Where, CAEE is cumulative AE energy, i is the number of event and E_i^{AE} is the absolute AE energy corresponding to event i . However, a unit-free AE energy is preferred, and this is the normalized cumulative AE energy, N_i , calculated using expression (19),

$$N_i = \frac{CAEE_i}{CAEE_M} \quad (19)$$

Where N_i is the normalized cumulative AE energy corresponding to event i , and $CAEE_M$ is the maximum cumulative AE energy corresponding to the last event. The normalized cumulative AE energy calculated using expression (19) represents the AE energy of all the events during the test, making no difference between them.

Based on the facts mentioned above the next assumption is made at this point: if the absolute AE energy is a true representation of the damage mechanisms in the material THEN there must be a relation between the damage variable D and the normalized cumulative AE energy N ,

$$D_i \approx N_i \quad (20)$$

This must be proved.

CHAPTER 5

EXPERIMENTAL RESULTS

The samples with dimensions are shown in Table 5.1 and the tests performed are shown in Table 5.2. The samples belong to different batches; however, they share a similar fiber-matrix architecture. The first batch of samples consisted of samples A, B, D, E, F, G and H used for open-end burst test. Sample C was from a different batch with weaker architecture. A second batch consisted of samples HT1, HT2 and HT3, used in high temperature test. A third batch consisted of samples 1, 2, 3 and 4, used in quenching test. Samples HT1, HT2 and HT3 had different lengths, the purpose was to evaluate the difference in length in the results.

Table 5.1: Dimensions of Si_f-SiC_m composite samples.

Sample	O.D. (mm)	I.D. (mm)	Length (mm)
A, B, C, D, E, F, G, H	10.3	7.87	31.75
HT1, HT2, HT3	10.63	7.83	12.7, 8.5, 4
1, 2, 3, 4	9.8	7.9	107

Table 5.2: Tests performed.

Sample	Quenching	High Temperature	Close-end Burst Test	Open-end Burst Test
A, B, C, D, E, F, G, H				X
HT1, HT2, HT3		X		
1, 2, 3, 4	X		X	X

5.1 RT OPEN-END INTERNAL PRESSURE TEST AND AE ANALYSIS

An image of sample A after a RT open-end bladder test is shown in Figure 5.1. Figure 5.1(a) shows the broken sample between the holders of the pressure rig with the AE sensor still attached to it. It can be observed in Figure 5.1(a)(b) that the sample collapsed following a macro-crack oriented in the axial direction. The presence of cracks oriented in radial direction are shown in Figure 5.1(c), similar orientation of cracks was found in all the samples after test, these cracks are perpendicular to the direction of the hoop stress. Figure 5.2(a) is the microscopic image of the cross section of the sample showing fibers and intra-tow cracks. Figure 5.2(b) is an SEM image along the edge of the sample showing the fiber pullout and part of the matrix. The stress-strain curve corresponding to the RT open-end bladder test of sample A is shown in Figure 5.3. This stress-strain curve is characteristic of the samples similar to sample A, same batch samples

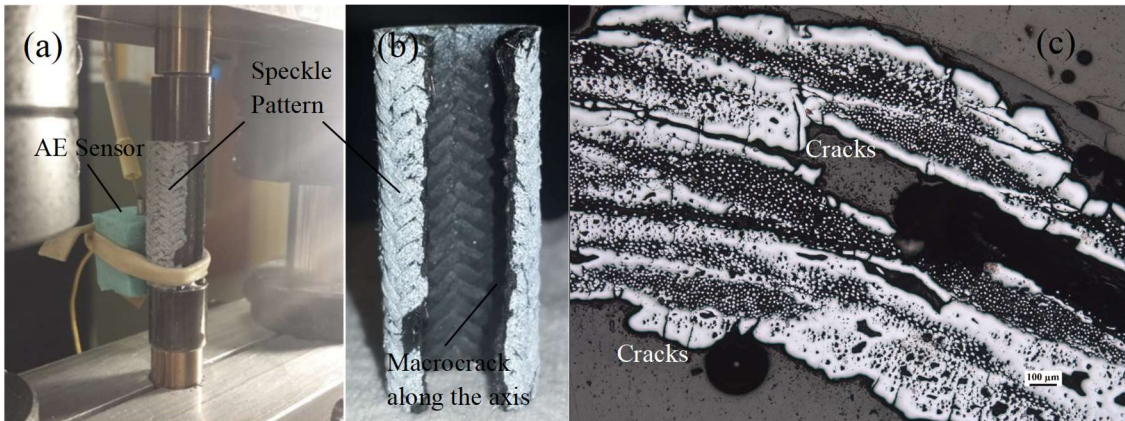


Figure 5.1: (a) sample mounted showing AE sensor, (b) speckle pattern and axial macrocrack and (c) cross section showing radial cracks.

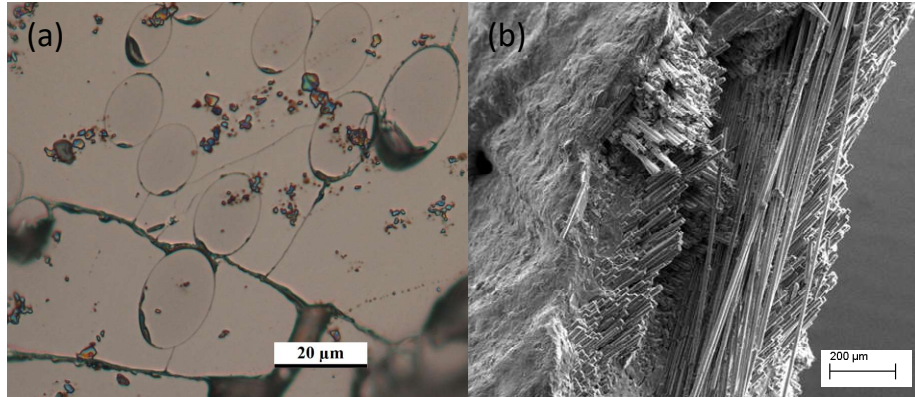


Figure 5.2: (a) intra-tow cracks and (b) fiber pullout after failure.

In Figure 5.3, the normalized cumulative AE energy N , corresponding to sample A, is also plotted against the strains. Clearly, N correlates with the stress-strain curve which shows a particular form and contains a few points of interest such as the Proportional Limit Stress (PLS) and the Ultimate Tensile Stress (UTS). The PLS is the stress level that corresponds to the initiation of the nonlinearity of the stress-strain curve and the UTS is the stress at failure. In Figure 5.3, it can be noticed that the AE activity initiates before the PLS suggesting that the damage before the PLS has not influence in the elastic constants, the damage is very small, i.e. microcracks, or is some form of dissipation energy that does not induce damage. From this point (PLS), the deterioration of the elastic constants occurs rapidly and is evidenced by the strong curvature of the stress-strain curve. This region has been related to matrix cracking and has been named as a matrix-driven region for the case of SiC composites. Also, in Figure 5.3, there is a point where the stress-strain curve starts behaving as quasilinear. This point is located at the intersection of the dashed lines and pointed with an arrow in Figure 5.3. This quasilinear region is known as fiber-driven region because the load is transferred to the fibers due to matrix cracking saturation and damage is due to fiber breaking and tow failure. The quasilinear region ends when the sample fails,

at this point $N=1$. In Figure 5.4, N is plotted against the stress and the AE Onset Stress is calculated as ~ 92 MPa by intercepting the stress axis with a line that follows the slope of the curve after the first large change in slope [101]. The AE Onset Stress is typically close to the PLS calculated as ~ 90 MPa.

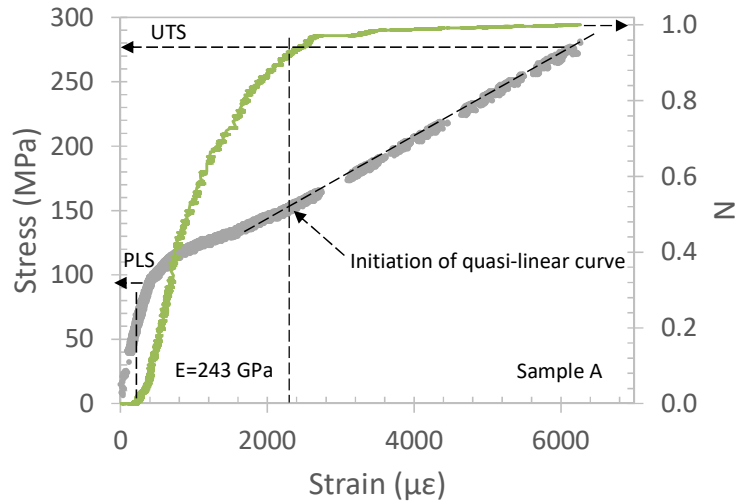


Figure 5.3: Stress vs. strain curve and the normalized cumulative AE energy N .

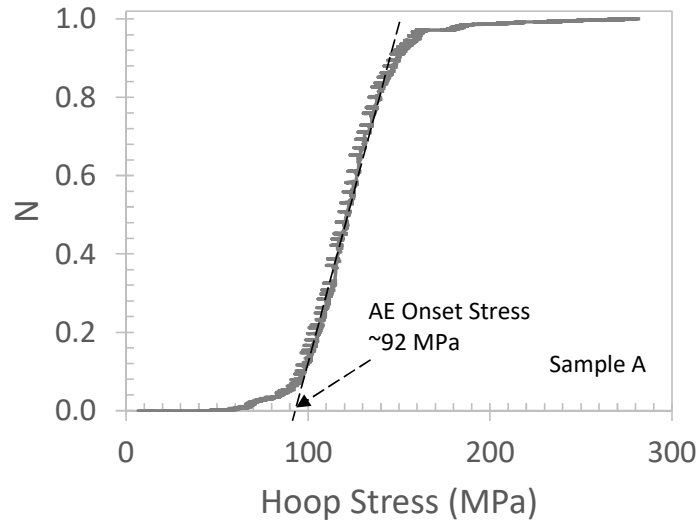


Figure 5.4: Calculating the AE Onset Stress of sample A.

5.1.1 MATRIX-DRIVEN REGION

Following the assumption that the absolute AE energy is representative of the damage of the material (expression 20) and that two nonlinear regions exist, matrix-driven and fiber-driven, the next assumptions are made:

1. Matrix cracking is the most important damage mechanism in the matrix-driven region, as was concluded in several studies about damage evolution in $\text{Si}_f\text{-SiC}_m$ composites [16,33,38,85,81,84,97]. It is not probably true in the fiber-driven region.
2. Most of the matrix cracks are perpendicular to the loading direction. This was confirmed by microscopy (Figure 5.1) and is mentioned in several studies on fiber reinforced composites, i.e. $\text{Si}_f\text{-SiC}_m$ composites [18,24,102,103,104,105] and carbon epoxy composites [35].
3. The absolute AE energy represents the energy released by a corresponding damage mechanism in the material. In the case of cracks, the amount of energy is proportional to the size of the crack, i.e. the higher the energy released the bigger the crack.
4. The damage variable D in the matrix-driven region is related to the absolute AE energy. This is not expected to occur in the fiber-driven region.

A first approximation is made for the case of the matrix-driven region by making the damage variable D equal to N (the normalized cumulative AE energy). Knowing D , the strains are calculated from the stresses, using expression (7). The modulus of elasticity is calculated from the stress-strain data corresponding to the elastic region, $E = 243$ GPa in the case of sample A. The calculated strains using this approximation are plotted in Figure

5.5 in the same stress-strain curve of the experimental data. The curve of the calculated strains starts at 90 MPa which is the calculated PLS. For stresses less than 90 MPa, D is so small that damage is marginal. As can be seen in Figure 5.5, the strains are predicted satisfactorily in the initial portion of the curve up to about 1200 $\mu\epsilon$, at strains larger than 1200 $\mu\epsilon$ the predicted strains are overestimated.

By definition, N represents the normalized cumulative AE energy of all the events that occurred during the test, therefore represents all the AE activity. A conclusion is drawn here, not all the events occurring during the test contribute to the damage in the material therefore some AE energy is not related to D . At this point, a method to identify the events not related to the damage D is needed. The methods of Unsupervised Pattern Recognition (UPR), Fast Fourier Transform (FFT) and modal analysis (MA) were used with the objective of classifying the AE data and separate the AE events that are not related to D . The optimum result in the UPR was two clusters. But the corresponding normalized cumulative AE energy of any of the clusters when made equal to the damage D , resulted in worse prediction than in Figure 5.5. The FFT and MA methods did not help to separate the AE data. It was no possible to form groups of AE data by comparing the peak frequencies obtained with FFT or the extensional/flexural modes of the waveforms. The reason is probably because in the open-end internal pressure test the direction of the stresses doesn't coincide with the direction of the fibers of the $\text{Si}_f\text{-SiC}_m$ composite tube.

When the direction of the load follows the orientation of the fibers a more predictable sequence of damage mechanisms is expected. In this case, the use of advanced methods such as UPR has been proved to be successful. Matrix microcracking, matrix cracking, fiber cracking, debonding and sliding may occur randomly during the open-end

internal pressure test of the $\text{Si}_f\text{-SiC}_m$ composite tube. The presence of noise is discarded as no noise was found during tests of dummy alumina and steel samples in internal pressure. As mentioned in the work by Morscher [19], the classification of waveforms is a difficult task because of the limitations of the AE sensors, the fact that a waveform corresponding to a source is made up of many frequencies, and presences of the reflections. Signal attenuation adds up to the limitations for the classification of waveforms as the AE parameters could change depending on the distance of the source to the AE sensor, this makes look different the waveform of similar sources [71].

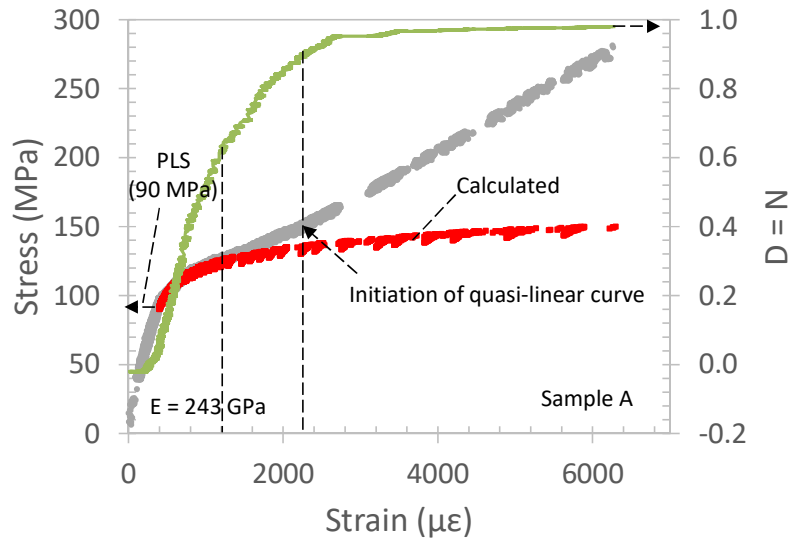


Figure 5.5: Stress vs. strain curve: experimental and calculated strains using D .

An analysis of the AE data was done based on some of the conclusions in the work by Maillet et al. [16]. Maillet et al. analyzed the AE data from a tensile test of a $\text{SiC}_f\text{-SiC}_m$ minicomposite using the method of Unsupervised Pattern Recognition (UPR) and wavelet analysis. Two clusters that represent two groups of AE signals were identified. One cluster grouped AE signals characterized by short risetime, short duration, high amplitude and high energy. A second cluster grouped AE signals characterized by longer risetime, longer

duration, lower amplitude and lower energy. The authors associated the first cluster with matrix crack and fiber break however it was concluded that this damage mechanisms do not occur at the same time; matrix cracking occurs first following fiber cracking. The second cluster is associated with interfacial phenomena such as debonding and frictional slip at the fiber/matrix interfaces.

Following the suggestion by Maillet et al., a trial an error analysis of the AE data was done using the AE parameters of risetime, duration, amplitude and energy. The focus was to find similarities between AE events having short risetime, short duration, high amplitude or high energy. Then it must be confirmed that the normalized cumulative AE energy is representative of the progress of damage in the $\text{SiC}_f\text{-SiC}_m$ composite tube by making D equal to the new calculated normalized cumulative AE energy. A successful estimation of the damage variable D , was possible by discarding events with high risetime starting by the event with the highest risetime. The risetime vs time graphic is shown in Figure 5.6. In Figure 5.6, the three regions identified in the stress-strain curve are delimited by dashed lines, they are elastic region, matrix-driven region and fiber-driven region. The best estimation of strains was possible by discarding the events with risetime equal or higher than a reference risetime which corresponds to 25% of the highest risetime. The discarded events are shown in Fig. 18 and they are located above the dashed line corresponding to the reference risetime equal to 25%. Then the normalized cumulative AE energy of the remaining events was calculated, $N_{25\%}$, and the new damage variable D was obtained by making $D = N_{25\%}$.

The strains calculated using the damage variable $D = N_{25\%}$ and expression (7) are shown in Figure 5.7. As can be seen in Figure 5.7, the strains predicted are very similar

than the experimental strains up to the initiation of the quasilinear curve where $D = 0.738$, beyond this point the strains are overestimated. In the fiber-driven region, part of the calculated curve seems to be shifted respect to the experimental curve. Clearly the method cannot be used in the fiber-driven region.

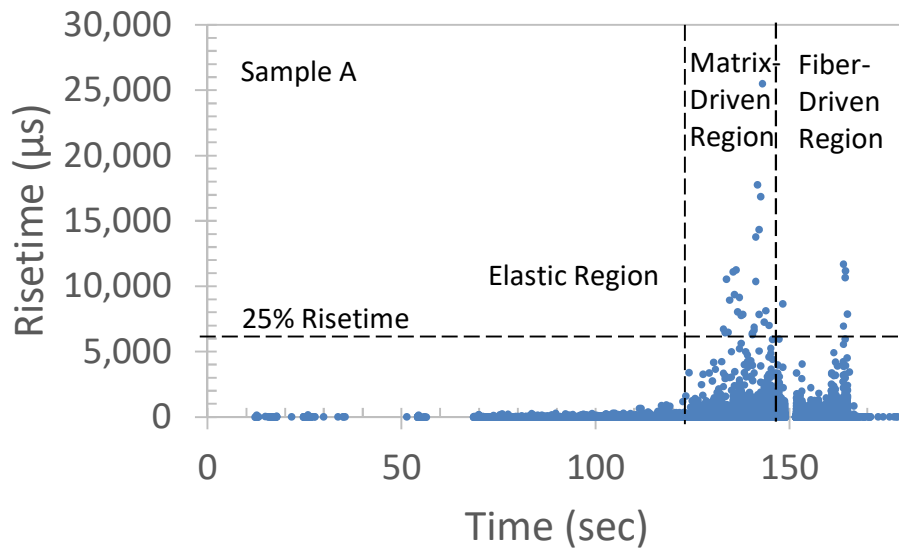


Figure 5.6: Risetime vs. time for sample A.

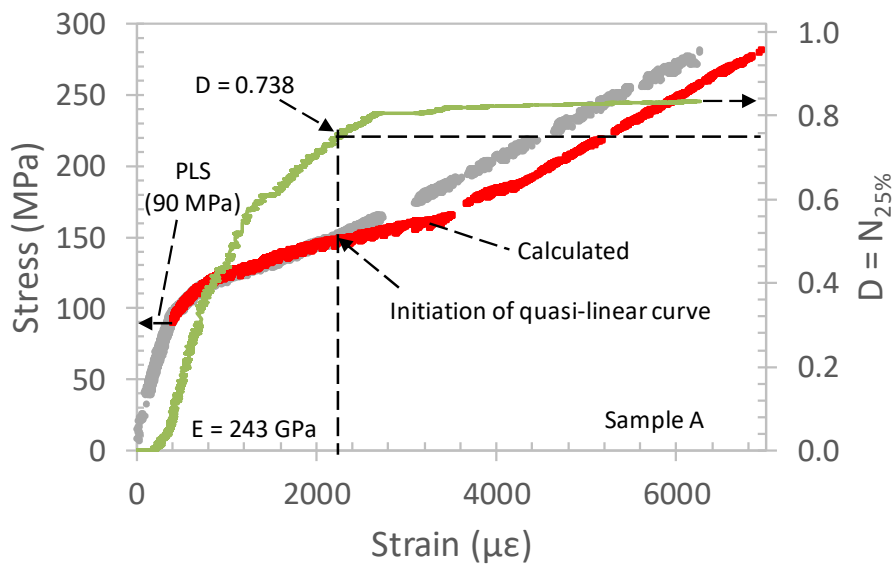


Figure 5.7: Stress vs. strain curve: experimental and calculated strains using $N_{25\%}$.

5.1.2 FIBER-DRIVEN REGION

Some studies make reference to the relation between fiber breaking and AE events. Maillet et al [16] found that the number of AE events in the fiber-driven region is in good agreement with the estimated number of fibers that must break before the collapse of the SiC/SiC minicomposite. Maillet et al. mentioned that a tow fails when 15% of the total number of fibers fail. Ni et al. [28] studied the fracture process of a single fiber composite in tension, he found that the number of AE events was in good agreement with the number of fiber breakages. An analysis of the AE parameters in the fiber region of sample A, suggest that the progress of damage occurs in sequences of events with AE parameters varying within a range as can be seen in Figure 5.8. If the cumulative AE events are plotted against the time as in Figure 5.9, a linear trend is noticed, with an average rate of events per second of ~ 187 . This suggest that the increment of the damage variable in the fiber-driven region has a direct correlation with time.

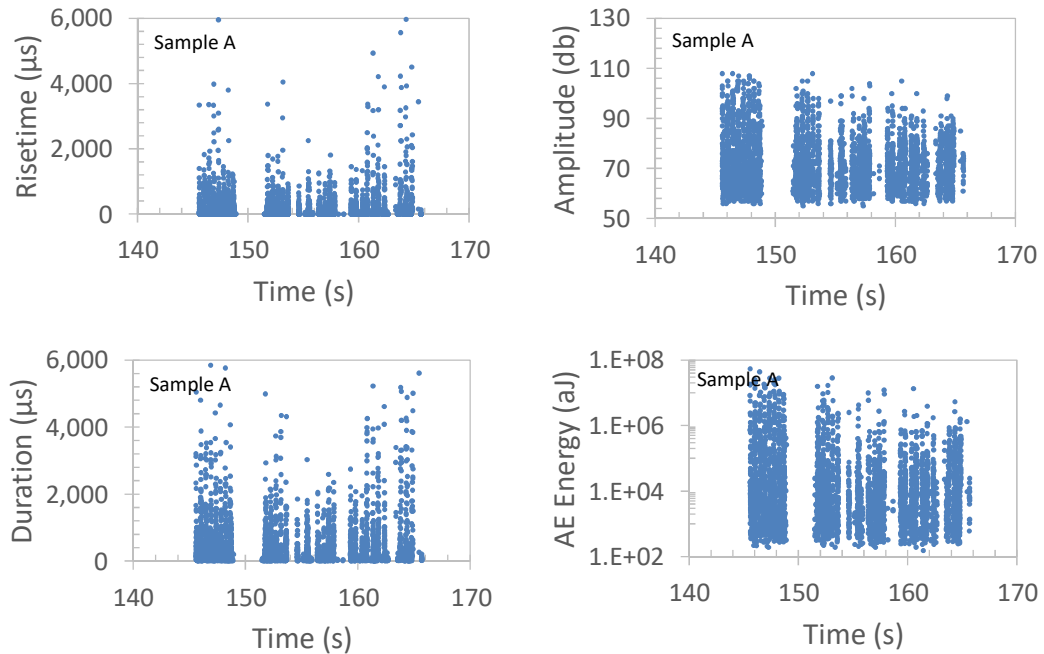


Figure 5.8: AE parameters in the fiber region of sample A.

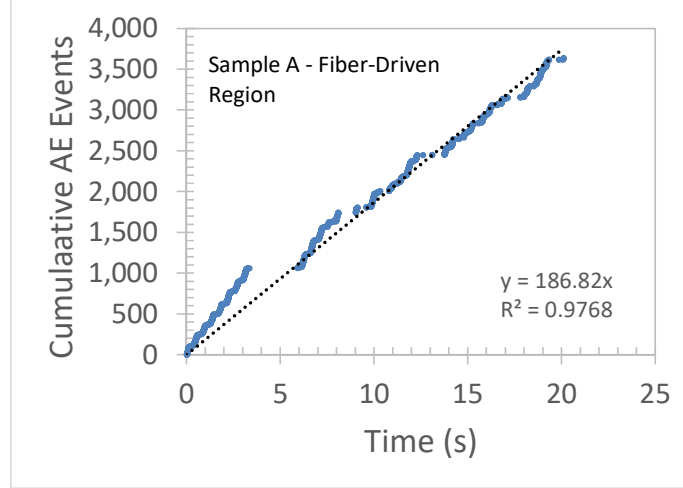


Figure 5.9: Cumulative AE events of sample A in the fiber-driven region.

Using the values of stress and strain corresponding to the last event, just before failure, from the experimental data, the last value of the damage variable can be calculated. The last value of the damage variable is 0.82, and from Figure 5.7, the value of the damage variable at the initiation of the quasilinear curve is $D_{RT} = 0.738$. In other words, the damage variable in the fiber-driven region varies from 0.738 to 0.82, an increase of 0.082. At this point an assumption is made, that the increase in damage can be calculated by multiplying the total increase of the damage variable by the fraction of time, expressed as,

$$\Delta D_{FR} = (\text{Increment of } D \text{ in quasilinear region}) \cdot \left(\frac{\text{Time between events}}{\text{Total time (s)}} \right) \quad (21)$$

In the case of sample A, the increment of D in the quasilinear region is 0.082, and the total time is 20.11 seconds. Finally, the damage variable is calculated as,

$$D_i = D_{i-1} + \Delta D_{FR, i} \quad (22)$$

Where i is the event number. The calculated stress-strain curve corresponding to sample A is shown in Figure 5.10.

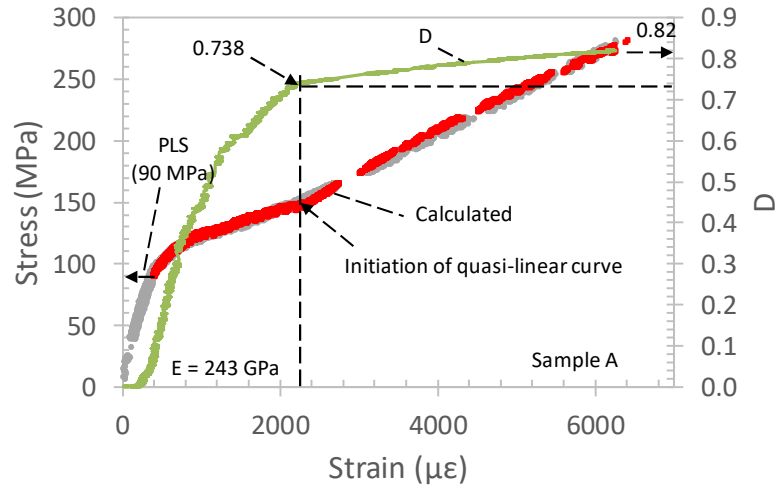


Figure 5.10: Stress vs. strain curve: experimental and calculated strains of sample A.

Data from sample B was analyzed following the same procedure as sample A but this time all data with risetime higher than 18% of the highest risetime was discarded. The results are shown in Fig. 23.

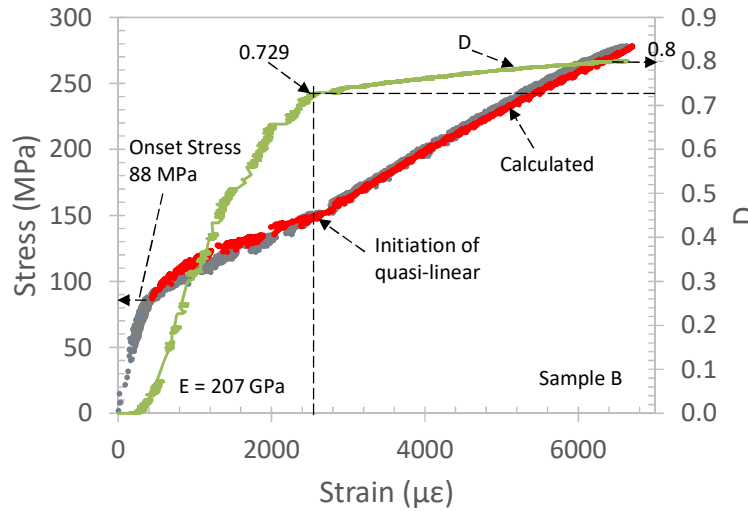


Figure 5.11: Stress vs. strain curve: experimental and calculated strains of sample B.

Data from sample C was analyzed as well following the same procedure as samples A and B. The results are shown in Figure 5.12. Sample C is from a different batch than samples A and B.

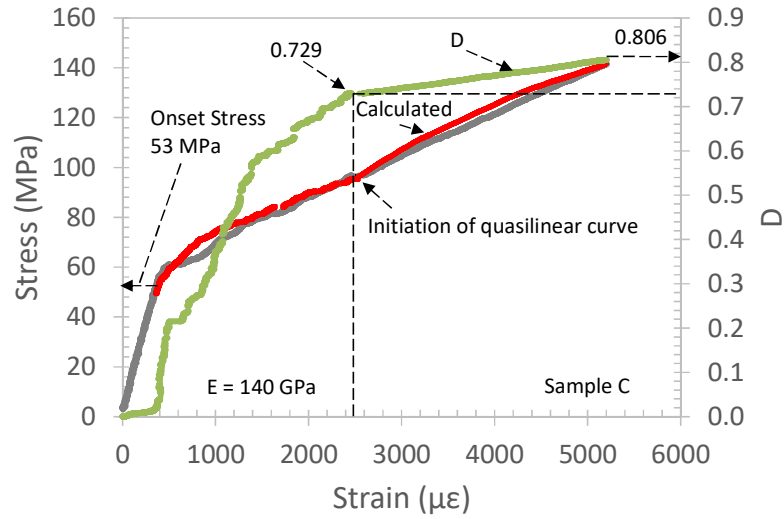


Figure 5.12: Stress vs. strain curve: experimental and calculated strains of sample C.

Based in the results of sample A, the next correlations are obtained as function of the stresses, see Table 5.3:

Table 5.3: Correlations to calculate the damage variable D .

Region	Correlation, D
Matrix-Driven Region	$-5.105 \exp^{-6} \sigma^3 + 1.801 \exp^{-3} \sigma^2 - 1.962 \exp^{-1} \sigma + 6.841$
Fiber-Driven Region	$3.205 \exp^{-1} \sigma^{1.671 \exp^{-1}}$

Where σ is the stress and $\exp. = 10$.

Correlations in Table 5.3 can be used to calculate the strains using D and expression (7) on samples showing similar characteristics than sample A, i.e. similar elastic modulus.

5.1.3 IMPORTANT REFERENCE POINTS IN THE STRESS-STRAIN CURVE

As a result, the AE analysis in part 5.1.1 and 5.1.2, two regions were found in the nonlinear part of the stress-strain curve in addition to the elastic region. One region is related to the nonlinear portion of the stress-strain curve that starts after the PLS and ends when the stress-strain curve becomes quasilinear. This region is characterized by matrix

cracking and is known as matrix-driven region. The other region is the quasilinear portion of the stress-strain curve that is characterized by fiber braking and is known as fiber-driven region. From the stress-strain graphs of the samples tested, the point at the end of the matrix-driven region and the beginning of the fiber-driven region seems to be located at approximately the same position in the graphs of all the samples tested, suggesting that it could be a characteristic of the material. The location of this point can be obtained by following the AE analysis followed in part. 6.1.1.

In Table 5.4 a summary of the damage variable, stress and strain corresponding to the point between the two nonlinear regions is shown. The damage variable, stress and strain at failure is included as well. In Table 5.4, the sub-index “int” refers to the damage variable, stress and strain at the point between regions. The sub-index “fail” refers to the damage variable, stress and strain at the failure of the sample. Data from samples A, B, E, F and C are included in the table. Sample F has an elastic modulus higher than A, B and E however they correspond to the same batch. Sample C is slightly different than the others having a lower elastic modulus than the other samples. It is important to notice that the values of the damage variable, stress and strain of the samples is close, including sample C, as can be seen in Table 5.4.

The damage variable corresponding to the point of the stress-strain curve between the matrix-driven region and the fiber-driven region is very close for all the samples, even for sample C. The value of the damage variable corresponding to the failure of the samples is very close as well for all the samples, including sample C. The difference between the values of the damage variable between regions and at failure, is shown in the last column

of Table 5.4. This value is very similar as well for all the sample. This difference must be related to the number of fibers broken during the test.

Table 5.4: Summary of data corresponding to inter regions and at failure reference points.

Sample	E(GPa)	D_{int}	σ_{int}	ϵ_{int}	D_{fail}	σ_{fail}	ϵ_{fail}	$D_{fail} - D_{int}$
A	243	0.738	150	2,165	0.82	273	6,191	0.082
B	207	0.729	152	2,623	0.8	278	6,223	0.071
E	211	0.758	153	3,039	0.82	280	7,436	0.062
F	330	0.75	178	2,200	0.814	266	4,342	0.064
Average	248	<u>0.744</u>	158	2,507	<u>0.814</u>	274	6,048	<u>0.0697</u>
C	140	<u>0.729</u>	96	2,420	<u>0.806</u>	141	5,190	<u>0.077</u>

It seems, that the value of the damage variable between nonlinear regions, D_{int} , and at failure, D_{fail} , are characteristics of the material, and can be used as references to quantify the level of damage, to identify the end of the matrix-driven region and end of the fiber-driven region. The variables D_{int} and D_{fail} may depend on the material and architecture of the SiC_f-SiC_m composite tubing. For the samples tested in this work D_{int} is 0.744 and D_{fail} is 0.814. This is valid for uniaxial loading as in the open-end internal pressure test.

5.1.4 USING THE MODEL TO PREDICT THE STRESS VS. STRAIN CURVE

The damage-variable method can be used to predict the stress-strain curve of a group of samples corresponding to the same batch. If the average modulus of elasticity of a few samples is known and the damage variable, D , of one of the samples is calculated, then the stress-strain curve of the other samples of the same batch may be predicted. In Table 5.5 the average modulus of elasticity of samples A, B, E, G and H and the correlation

of the damage variable calculated using data corresponding to sample A is shown. The average elastic modulus and the correlation of damage was used to predict the stress-strain curve of samples B, E, G and H. Figure 5.13 shows the plots of predicted and experimental curves of the samples. The predicted curve simulates the experimental curve closely however the predicted strains are slightly underpredicted. In the case of sample F, there is not a good match between the predicted and experimental curves. This difference is due to the high modulus of elasticity of sample F (330 GPa) which is about 57% higher than the average.

Table 5.5: Correlation of damage variable, D and average modulus of elasticity.

Average E (GPa)	$D_{\text{Matrix-Driven Region}}$	$D_{\text{Fiber-Driven Region}}$
209	$1.364760E^{-9}\sigma^5 - 7.962063E^{-7}\sigma^4 + 1.792464E^{-4}\sigma^3 - 1.936945E^{-2}\sigma^2 + 1.009528\sigma - 2.0399910$	$0.321663\sigma^{0.166490}$

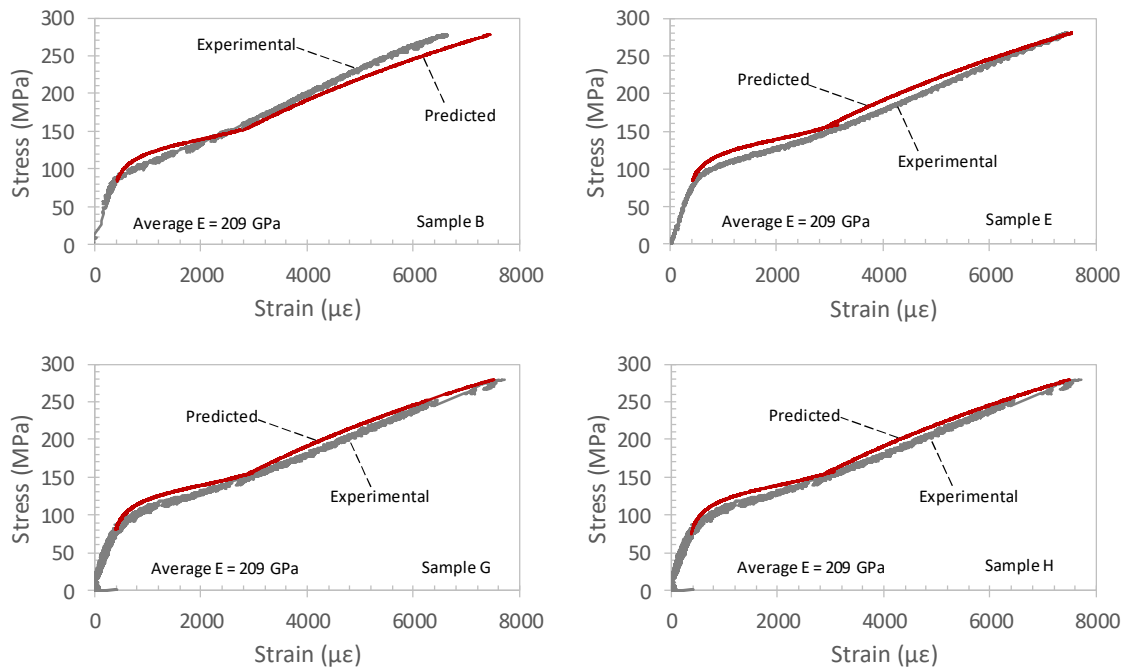


Figure 5.13: Predicted vs. experimental stress-strain curve.

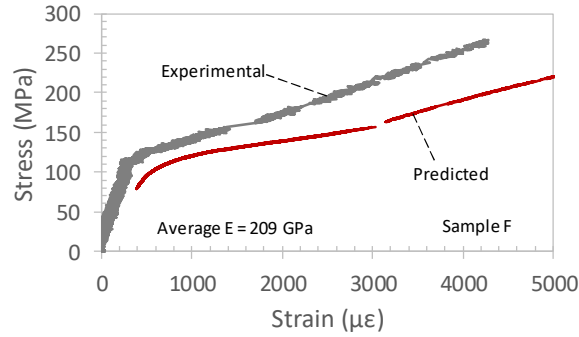


Figure 5.14: Bad match between predicted and experimental stress-strain curve.

5.1.4 WAVEFORMS

In this work, there are no intentions to relate waveforms and damage mechanisms. However, a visual inspection of the waveforms corresponding to sample C, made possible to identify the waveforms that are more frequently observed. The waveforms, corresponding to events with AE energy with order magnitude 10^6 and 10^7 aJ, found more frequently in the matrix-driven region, are shown in [Figure 5.15](#). In the vertical axis, it is shown the Voltage of the signal, the range is ± 2.5 Volts and in the horizontal axis it is shown the time in microseconds (μs), the range is zero to $800 \mu\text{s}$. Only the waveforms with high energy are included as it is believed that these waveforms represent the progress of damage in the composite more than the low energy signals. Signals with AE energy of less than 10^6 aJ are considered low energy signals, which contribution is low or none.

In [Figure 3.15](#), signals (1) and (3) represent about 40% of the total number of signals found in the matrix-driven region. The total number of high energy signals was 513. It is probable that most of the waveforms in [Figure 5.15](#) represent matrix cracking, however it cannot be confirmed. Signals (1) and (2) are clearly different, signal (1) has short risetime, low amplitude and long duration, while signal (2) has very short risetime, high amplitude and short duration, both have AE energy in the order of 10^6 aJ.

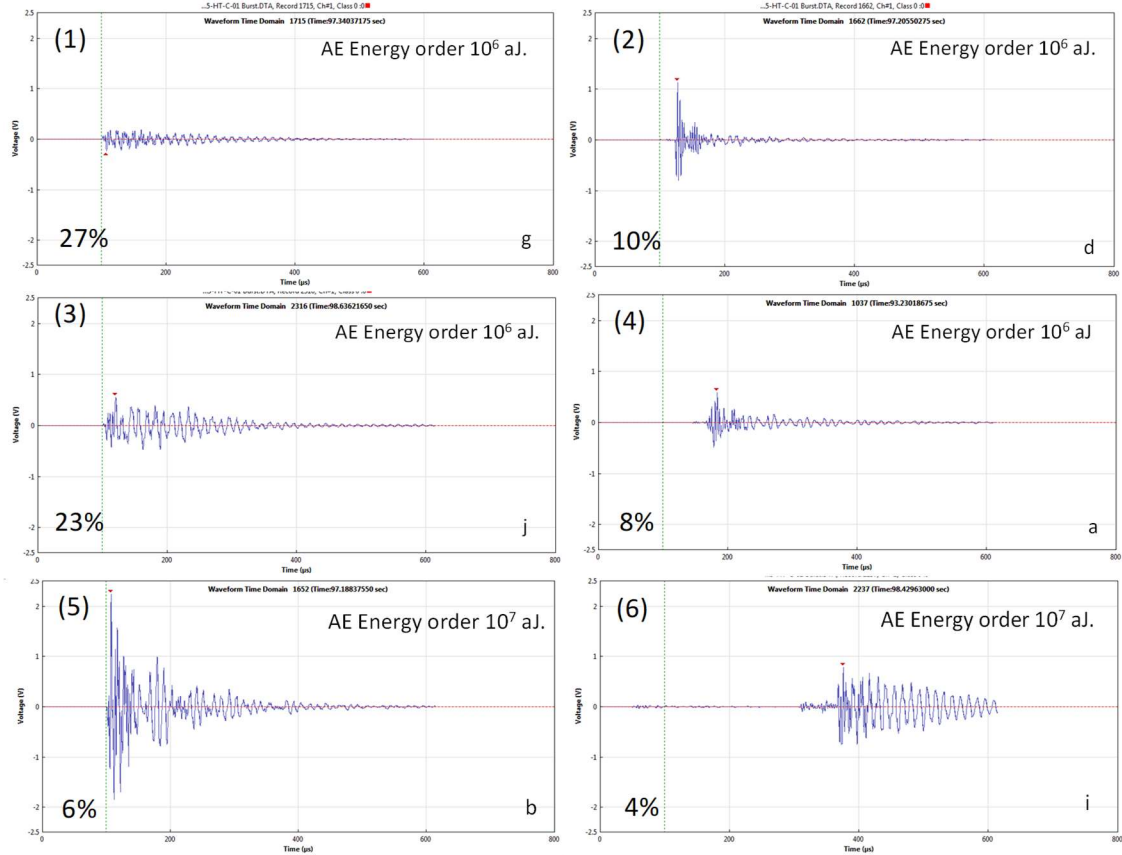


Figure 5.15: Frequently observed waveforms in the matrix-driven region.

Signals (2) and (5) have similar risetime and similarity in the modes of the wave: extensional, flexural and reflections, but different amplitude and duration. It seems that waveforms (1), (3) and (6) may be related to the same damage mechanism. The same can be said from waveforms (2), (4) and (5). Based on a FFT analysis, the peak frequency of waveforms 1, 2, 3, 4 and 6 is 78 kHz while the peak frequency of waveform 5 is 83 kHz. This difference of 5 kHz is not significant.

The waveforms, corresponding to events with AE energy in the order of magnitude of 10^6 and 10^7 aJ found more frequently in the fiber-driven region, are shown in [Figure 5.16](#). In the graph, the vertical scale is ± 2.5 V and horizontal scale is zero to 800 μ s.

In Figure 5.16, waveform (1) alone represent about 44% of the total number of signals found in the fiber-driven region, followed by waveform (2) with about 21%. The total number of high energy signals was 63, lower number of signals than in the matrix-driven region. Waveforms (1), (3), (4) and (6) may be related to the same damage mechanism. The same may be the case of waveforms (2) and (5). It is not possible under the circumstances and is not the objective of this work to identify the waveforms and the corresponding damage mechanisms. Based on a FFT analysis, the peak frequency of waveforms (1), (4) and (6) is 78 kHz, the peak frequency of waveform (2) is 302 kHz, the peak frequency of waveform (3) is 87 kHz and peak frequency of waveform (5) is 83 kHz. The peak frequency of waveform (2) is clearly the largest, the peak frequency of the other signals is very close.

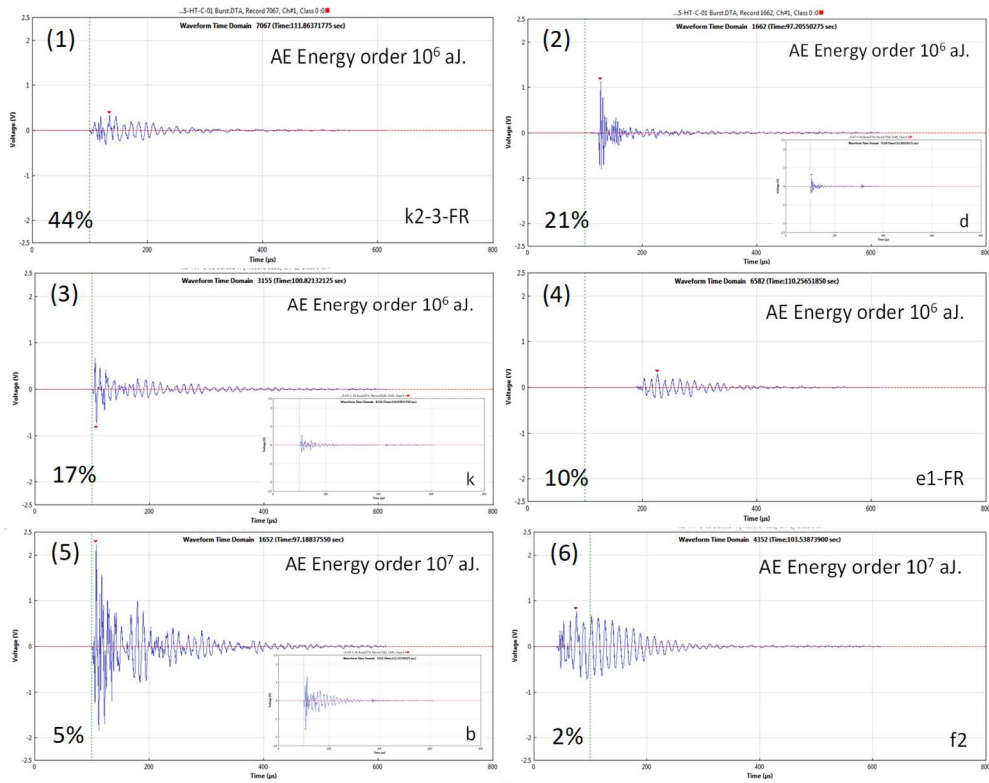


Figure 5.16: Frequently observed waveforms in the fiber-driven region.

Comparing waveforms from [Figure 5.15](#) and [Figure 5.16](#), it seems to be a similitude between waveforms from the matrix-driven region and the fiber-driven region. The only exception is waveform (2) from the fiber-region which has a peak frequency that is higher than the peak frequencies of the other signals, regardless the similitude with waveform (2) from the matrix-driven region. About 13 waveforms (2) were observed in the fiber-driven region.

Finally, an example of the waveforms discarded due to high risetime, see part 5.1.1, is shown in [Figure 5.17](#). A total of 15 waveforms were discarded. In the graph, the vertical scale is ± 2.5 V and horizontal scale is zero to 800 μ s. These waveforms seem to be the results of two or more signals that occurred in a very short time and were interpreted by the AE program as one signal as in (1). Signal (1) correspond to the knee in the stress-strain curve, and waveform (2) corresponds to the event at failure of the sample. The peak frequencies of 11 of the waveforms are between 78 and 87 kHz. Four waveforms had frequencies between 268 and 307 kHz.

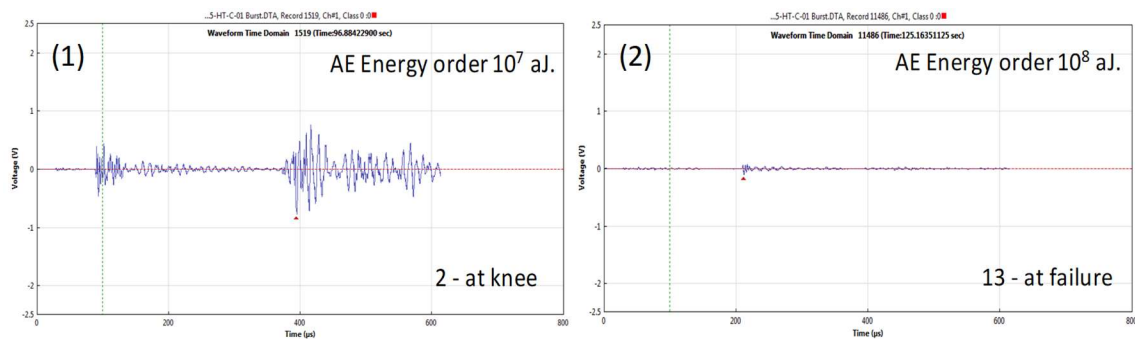


Figure 5.17: Example of waveforms discarded due to high risetime.

5.2 CONTINUUM DAMAGE MECHANICS IN UNIAXIAL LOADING

Another method to predict the strains is using the continuum damage mechanics (CDM) approach introduced in Chapter 4. An important step in the formulation of the

method is the identification of the damage evolution law and the reference thermodynamic forces, Y_{oi} . The damage evolution law is the variation of the damage variable as function of thermodynamic forces and reference thermodynamic forces. Remember that the thermodynamic forces are defined by the stresses induced in the composite. The reference stresses are extracted from the stress vs. strain curves obtained from mechanical tests performed to the composite sample. Typical mechanical tests are: uniaxial tension, uniaxial compression, torsion, Iosipescu test etc. The tests are performed in directions that coincide with preferred orientations such as fiber orientation and load direction, or oriented at a specific angle. In this work, the test is an open-end internal pressure test that loads the sample in the hoop direction. This test is a uniaxial test and the load induces hoop stresses and strains. No axial load is applied. The stress vs. strain curve corresponding to sample A is shown in Figure 5.18 where four regions can be seen in the graph: the elastic region, the matrix-driven region I, the matrix-driven region II and the fiber-driven region. The matrix-driven region was separated in two: matrix-driven region I and matrix-driven region II. The reason to separate the matrix-driven region in two is because the CDM method correlated in part of the matrix-driven region only. For this reason, the AE energy was used to calculate the damage variable in the matrix-driven region I, and the CDM method was used in the matrix-driven region II and the fiber-driven region. Once the damage variable is calculated, the strains can be found using the stresses and expression (7). The expressions used are found in Table 5.6.

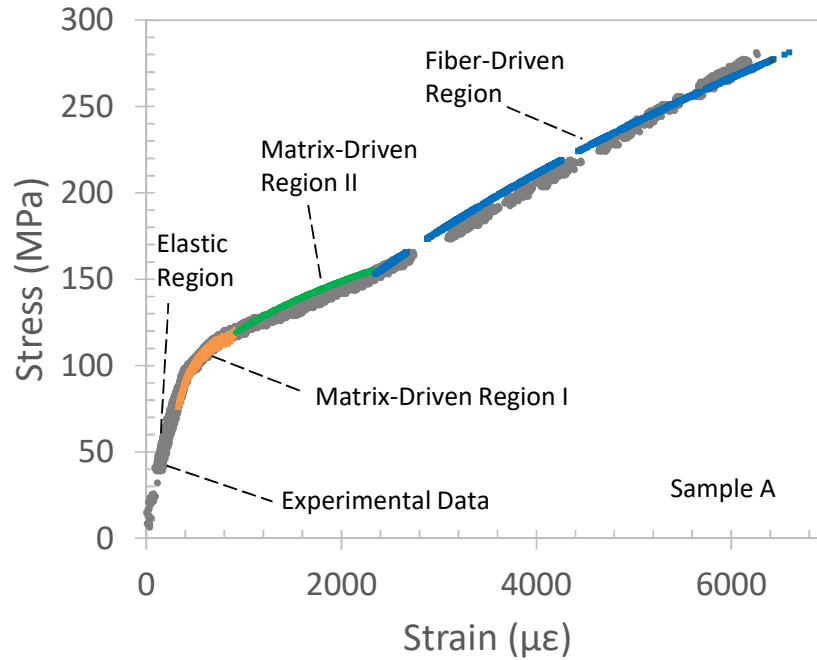


Figure 5.18: Stress vs. strain curve: experimental and calculated strains of sample A, found using expressions from Table 5.4.

Table 5.6: Expressions of the damage variable D used to predict the strains obtained during the internal pressure test of sample A.

Region	Expression	Ref. force, σ_{R1}	Ref. force, σ_{R2}
Elastic Region	----	----	----
Matrix-Driven Region I	$D = (\text{norm. cumulative AE energy})$	----	----
Matrix-Driven Region II	$D = 1 - 0.3 \left(\frac{\sigma_1}{\sigma_{R1}} \right)^{-2.5}$	150	----
Fiber-Driven Region	$D = 1 - 0.15 \left(\frac{\sigma_1 + \sigma_{R1}}{\sigma_{R2}} \right)^{-1.2}$	150	500

The same expressions from Table 5.4 were used to predict the strains of sample D, the results are shown in Figure 5.19.

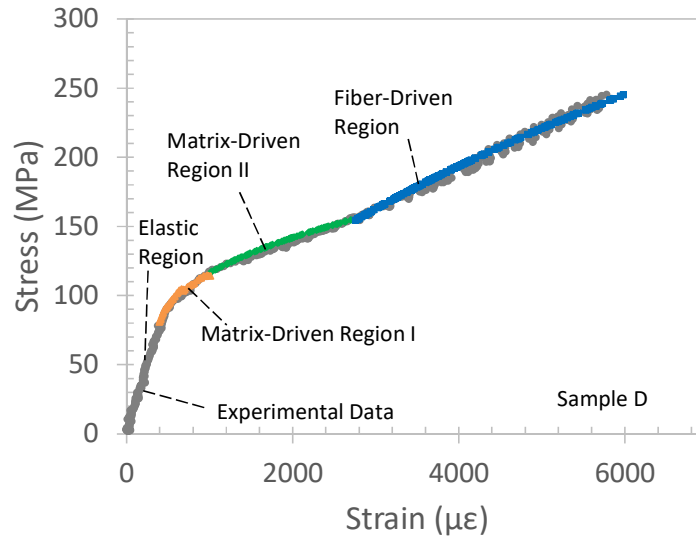


Figure 5.19: Stress vs. strain curve: experimental and calculated strains of sample D, found using expressions from Table 5.4.

As can be seen in Figure 5.18 and Figure 5.19, the CDM method predicts the strains satisfactorily however this is not always the case. Some deviations from the experimental values could happen for example when there is a difference in elastic modulus or when the stress-strain relation is different, e.g. samples from different batches or presence of fabrication defects.

5.3 RESULTS OF HT SOLID-SURROGATE TEST

A picture of the $\text{SiC}_f\text{-SiC}_m$ composite sample mounted on the alumina surrogate tube is shown in Figure 5.20. In Figure 5.20, the position of the AE sensor is represented by a circle. The dimensions of the samples and the surrogate tubes used in the HT solid-surrogate test are shown in Table 5.7.

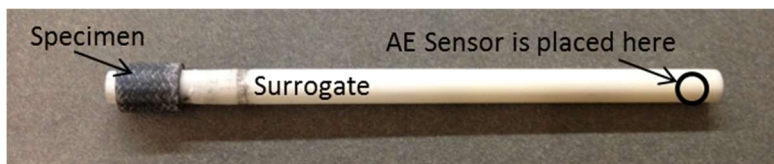


Figure 5.20: Picture of $\text{SiC}_f\text{-SiC}_m$ composite sample mounted on surrogate tube.

Table 5.7: Dimensions of SiC samples and surrogate tubes.

Parameter	Monolithic SiC	SiC Composite	Surrogate
Outer Diam. O.D. (mm)	9.5	10.63	6.35 and 7.95
Thickness (mm)	1.58	1.4	0.79 and 1.2
Length (mm)	9	12.7 (G), 8.5 (H), 4 (I)	10 and 140

Figure 5.21 shows the representative temperature and strain history for SiC_f-SiC_m composite sample G. The test was conducted up to ~1350 K as measured on the outer surface of the specimen. T_{out} and T_{middle} are the temperature at the outer surface and in the ceramic adhesive layer, respectively. The temperature difference ($T_{middle} - T_{out}$) increases as the power of the heater increases reaching a maximum of 250 K when T_{out} is 1350 K. Despite the thinness, the adhesive bond layer is porous. This will lead to a finite thermal contact resistance [94] between the surrogate and the specimen. The sudden rise in temperature at 117 seconds corresponds to the time when the heater was inserted into the position inside the surrogate. At ~215 seconds T_{out} was increased at the rate of 0.45 K/s by increasing the voltage in the circuit.

In Figure 5.22, the 3D-DIC total-strain map on the outer surface of the SiC_f-SiC_m composite sample HT1 at ~1350 K is shown. The strain distribution on the surface is non-uniform as a result of the complex structure of the composite. Some of the color bands in the strain map can be seen to overlap with the fiber tow structure. The high strain values on the border of mapped region are believed to be the result of image correlation error due to the curvature of the sample. The reported strain value is the average value of a 5 mm x 10 mm window in the center of the specimen. The mechanical strains are calculated by subtracting the thermal strains from the total DIC strains. The thermal expansion

coefficient of nuclear grade $\text{SiC}_f\text{-SiC}_m$ as a function of temperature from Snead et al. [31] is used to calculate the thermal strain. The total strains and the mechanical strains are shown in Figure 5.21 as well. Clearly, the strain-time profiles follow the temperature-time profile as expected. The error of the total DIC strains is around $250 \mu\epsilon$ during the test.

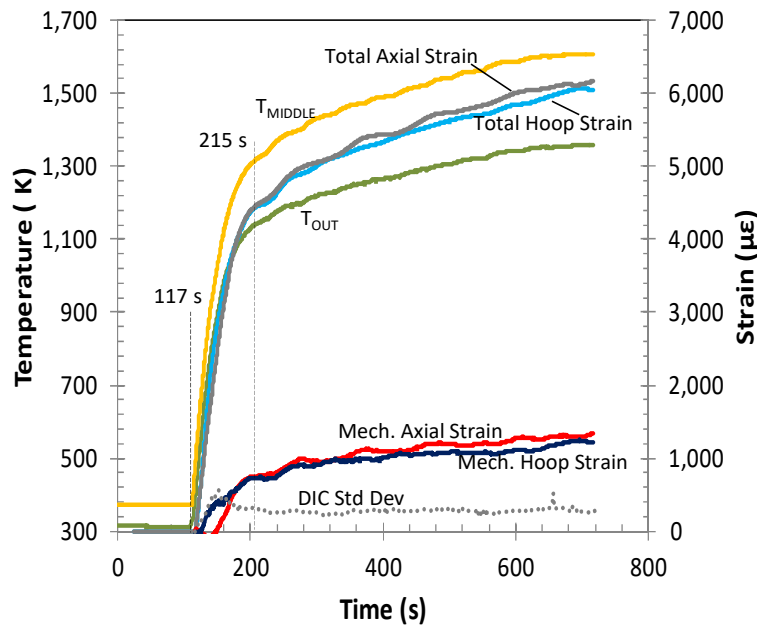


Figure 5.21: Temperature profiles and strains of sample HT1.

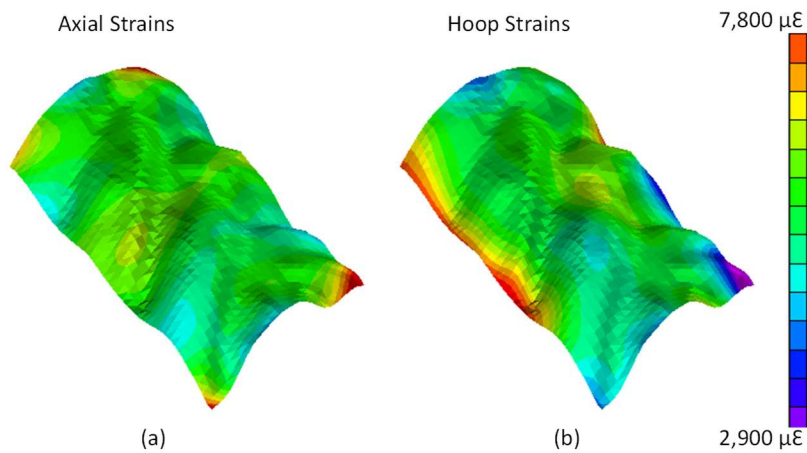


Figure 5.22: 3D DIC-strain map of sample HT1 at $1350 \text{ }^\circ\text{K}$, (a) total axial strains, (b) total hoop strains.

The maximum combined thermal and mechanical strain measured during testing reaches approximately 6000 $\mu\epsilon$ in both the axial and hoop direction. This corresponds to mechanical strain of approximately 1300 $\mu\epsilon$. Based on room temperature stress versus strain data obtained by burst test similar to the test shown in Figure 5.1, this corresponds to approximately 130 MPa hoop stress at the OD of the composite and 200 MPa at the ID of the composite. This stress/strain values are well past the linear elastic region of the composite, but short of the UTS which is typically a minimum of 250 MPa and 5800 $\mu\epsilon$.

In Figure 5.23, T_{out} , ϵ_{ma} , ϵ_{mh} , and AE energy are plotted vs. time. As can be seen from Figure 5.23, the AE activity starts shortly after the heater was inserted in position, and of special interest is the AE activity during the transient phase, from 117 to 215 seconds. Is in this region that the PLS must be located. AE events with high energy, much higher than the bulk energy data such as points *a*, *b*, *c* and *d* in Figure 5.22, represent important stress levels associated with internal damage of the material (e.g. microcracking) manifested as a decrease in the modulus of elasticity [100].

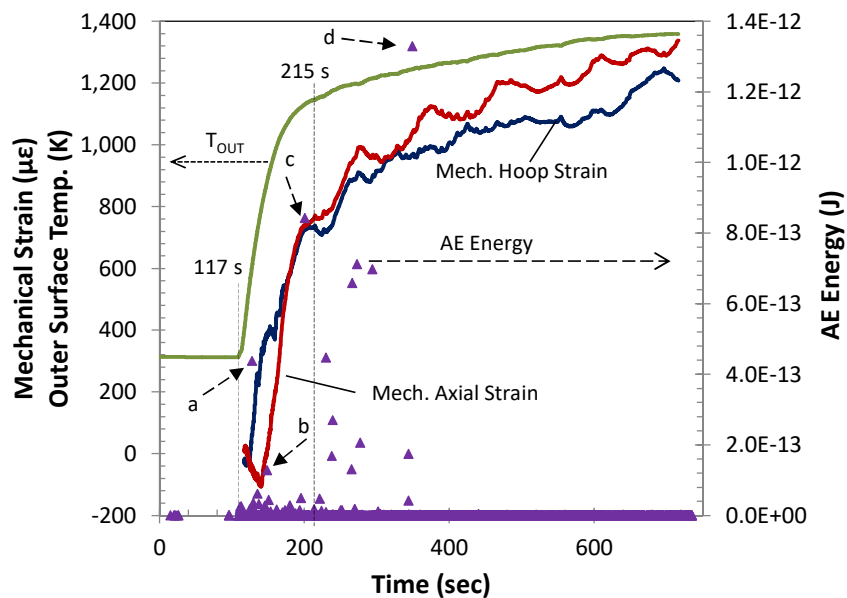


Figure 5.23: T_{out} , Mechanical strains and AE energy of sample HT1.

While the specimen remained intact, inspection under optical microscope LEICA CTR6000 (50x magnification) revealed microcracks in the inner surface of the sample, as shown in Figure 5.24, where the maximum hoop stress occurs. This suggest that the specimen was damaged beyond the PLS.

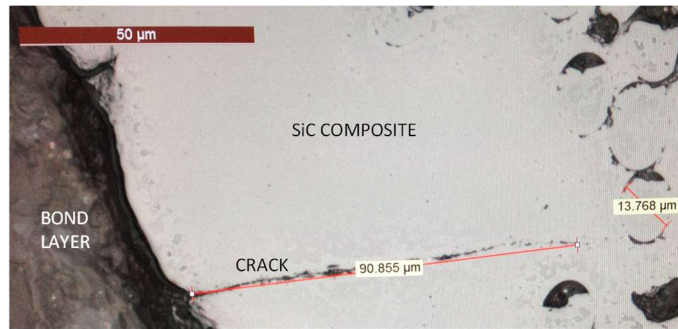


Figure 5.24: 50x magnification microscopic image of cross section of sample HT1.

Results on sample HT2, with length of 8.5 mm, are shown in Figure 5.25 and 5.26. In Figure 5.25, the temperature and strain history of specimen I are plotted. The total strains follow the temperature profile, as expected. The axial (ϵ_{ma}) and hoop (ϵ_{mh}) components of the mechanical strains are equal in magnitudes at the beginning of the test; however, the axial mechanical strain become larger than the hoop mechanical strain after the transient phase till the end of the test. The same temperature ramp rate of ~ 0.45 K/s was applied after the transient phase of the test. The strain ratio, $\epsilon_{ma}/\epsilon_{mh}$, grows from 0 to 1.03 (273-832 K), then slightly decreases down to 0.97 and then continues to increase until the end of the test reaching a maximum value of 2.7. This indicates that while the micro-cracking has relieved most of the hoop stress, the sample is still bonded to the surrogate and thus being forced to extend in the axial direction with the surrogate tube. The DIC error is around $250 \mu\epsilon$, increasing at the end of the test to $800 \mu\epsilon$. The larger error at the end of the test is probably caused by micro cracking at the surface and the spallation of the speckle pattern.

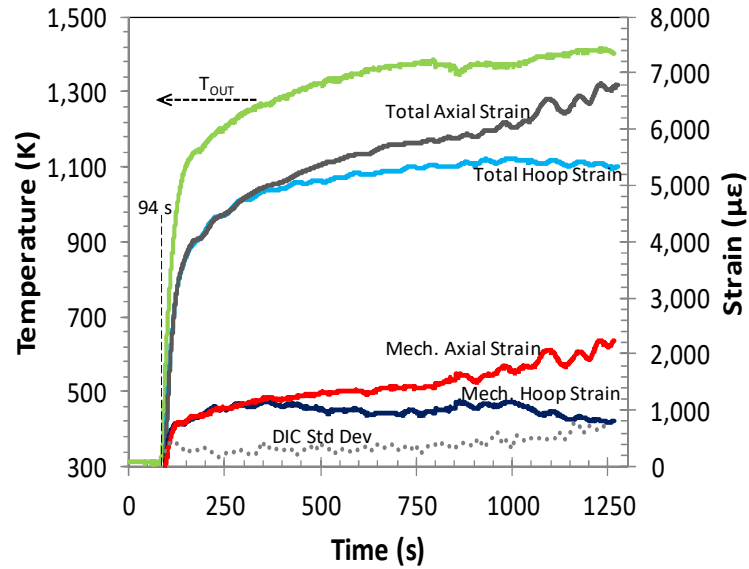


Figure 5.25: Temperature profiles and strains for sample HT2.

In Figure 5.26, the mechanical strains and the individual AE energy events are plotted vs. time for sample H. As in the case of specimen HT1, the largest activity of AE signals occurs during the transient phase and the beginning of the constant temperature ramp phase up to 280 s. In Figure 5.25, bursts of energy are observed at different times during the test. The first high energy event ($4.1 \text{ E}^{-13} \text{ J}$) occurred when the surface mechanical hoop strain reached $\sim 731 \text{ } \mu\epsilon$, and an energy emission of $3.5 \text{ E}^{-13} \text{ J}$ is observed close to the end of the test. During post-test examination under a microscope, a single thin surface crack was observed orientated along the axis of the sample tube.

Similar results were observed for all types of composite samples in terms of temperature, strain and AE response. No macroscopic cracks can be seen by unaided visual examination for all specimen types. Micro-cracking at the I.D. was observed for specimen type HT1 and micro cracking at the OD were observed for specimen type HT1 and HT3. Figure 5.27 shows the X-ray tomography image of a composite sample (type HT3) after test with maximum $T_{\text{out}} = 1351 \text{ K}$, showing a micro crack running through the thickness of

the specimen. The through-crack appears to have been deflected multiple times when advancing through composite wall. Despite the through thickness crack it does appear that some ability to carry stress and strain is retained in the specimen as no sudden drops in strain were observed during the high temperature testing.

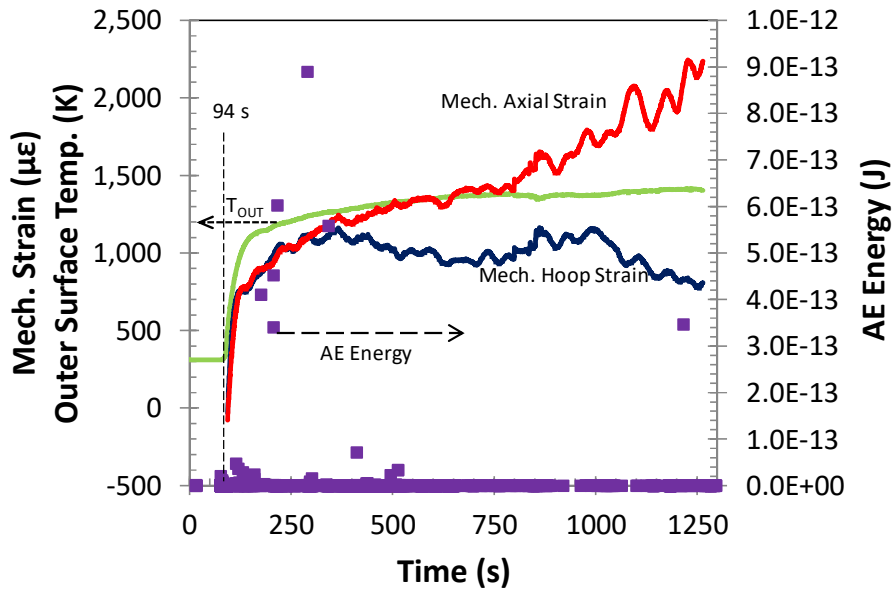


Figure 5.26: Mechanical strains and individual AE events for sample HT2.

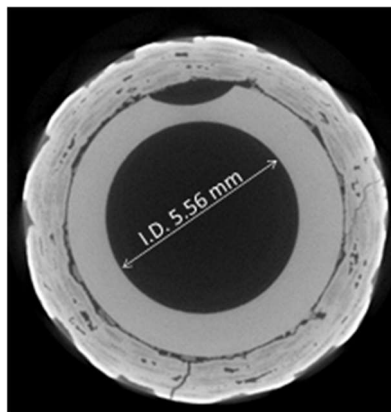


Figure 5.27: X-ray image of sample HT3.

An interesting pattern of surface mechanical strain history is observed for all lengths of $\text{SiC}_f\text{-SiC}_m$ samples. Initially, the measured axial strain on the sample surface is

close to the measured hoop strain. This is consistent with the expected bi-axial stress state in which roughly equal amounts of stress are observed in both the axial and hoop direction, as demonstrated in the FEM described below. After a period of intense AE events, the axial strain starts to exceed hoop strain as the test progresses. Together with post-examination evidences, it is believed that micro-cracking is occurring during the thermo-transient phase (as evidenced by the intense AE events), and these cracks runs primarily along the axial direction as seen in the micrograph. Such cracks relax the hoop stress more than the axial stress, and hence results in lower hoop strain than the axial strain.

This effect seems to be more pronounced as size of the specimen is decreased. They are two contributing factors that may explain this observed trend. The type G samples were overcoated with SiC at General Atomics so that the cut ends were sealed and protected from the environment. However, for type H and I composites this overcoating was not performed. It is believed that in type H and I samples, oxidation of the PyC interphase coating occurs which leads to a more brittle like composite behavior and additional through thickness cracking takes place. The second factor is that the FEM model described below reveals a pronounced edge affected zone where the hoop stress near the free edge of the tube segment is significantly higher than the hoop stress in the center of the tube. For shorter specimen, the edge affected zone represents a much larger fraction of the samples. It is believed that more cracking (along the axial direction) occurred in shorter specimen. This resulted in more pronounced relaxation of hoop strain. Additional testing is currently being performed to validate these theories, which may underscore the need to select sample of adequate length and properly protect the interphase layer from degradation during exposure to severe conditions.

5.3.1 SiC_f-SiC_m COMPOSITE MODELING

FEM models were constructed to predict temperature, stress, and strain distribution through the thickness direction and length of the high temperature test assembly. The model is steady state with a temperature of 1087 K on the outer surface of the sample. In order to simplify the modeling, the composite material is assumed to be a linear-elastic orthotropic material. This assumption is acceptable, because the level of mechanical strains on the outer surface at the temperature of 1087 K, are expected to be inside or close to the elastic region of the SiC_f-SiC_m composite. As such, the FEM model will not be able to capture the pseudoplastic behavior that occurs beyond the PLS of the SiC_f-SiC_m composite. The thermo-mechanical properties of surrogate, bond layer, and specimen used in the model are in Appendix 1 [106,107,108,109]. The constitutive equations solved in the model and boundary conditions are shown in Appendix 2. The SiC_f-SiC_m sample is modeled as a four-layer orthotropic composite with fiber orientation of +45°/-45°/+45°/-45° for each layer. An image of the sample-surrogate assembly is shown in Figure 5.18 and the dimensions are given in Table 5.6. A schematic of the sample-surrogate assembly and heat flux modeled (convection was modeled but is not shown in the schematic) are illustrated in Figure 5.28(a). Figure 5.28(b) show the mesh used and Figure 5.28(c) shows the deformed sample-surrogate (exaggerated) corresponding to a simulation for $T_{out} = 1087$ °K.

The model solves a heat transfer problem where radiation, convection and conduction of heat are involved, having as boundary conditions the ambient temperature and a heat flux on the inner surface of the surrogate that extends in axial direction in a length similar to the specimen's length. Heat conduction occurs through the material, and

convection and radiation occur on the outer surfaces. The deformed $\text{SiC}_f\text{-SiC}_m$ sample shows a characteristic wheat sheath (or hourglass) shape due to the transition from plane strain (near the center) to plane stress (at free end) state. The fuel pellet shows similar deformed shape when temperature gradient exists [107].

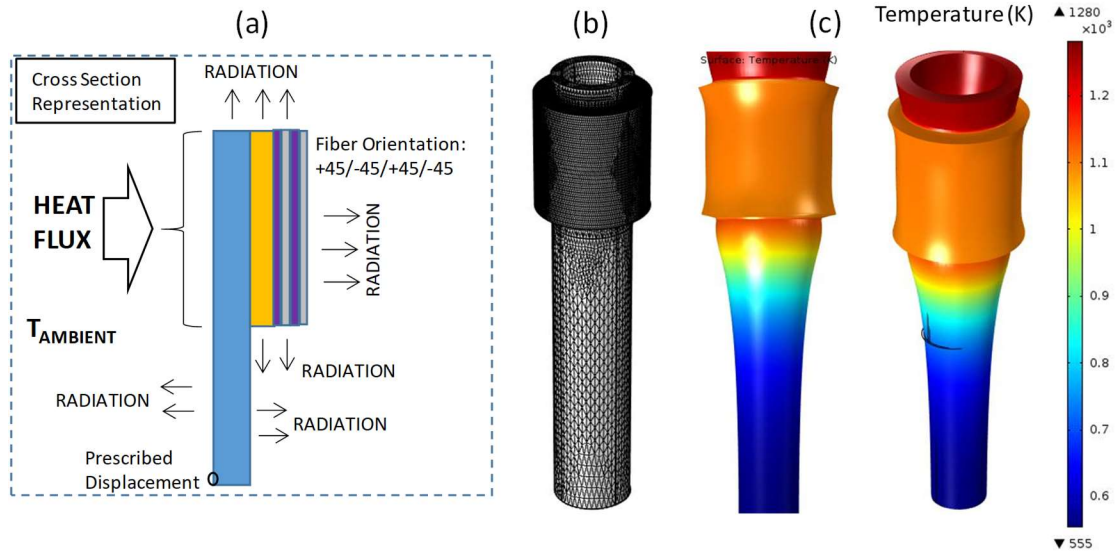


Figure 5.28: Schematic of sample-surrogate assembly showing the heat flux (a), an image of the meshed sample (b) and the deformed sample obtained from the simulation.

Figure 5.29 – 5.31 show the through thickness distribution of temperature, stress and strain near the center of the specimen. Due to the porous nature of ceramic paste, its thermal conductivity is much lower than dense ceramic material of the same composition. A large temperature drop across the ceramic paste is predicted. The model predicts that the surrogate is in compression, while the SiC composite sample and the bond layer are in tension. The predicted mechanical strain is slightly higher than the measured mechanical strain at the corresponding outer surface temperature ($T_{\text{out}} = 1087 \text{ }^\circ\text{K}$). The axial mechanical strain distributed through the wall is very uniform, while a gradient of hoop mechanical stress is predicted. The highest hoop stress and strain occurs at the inside

surface of the SiC composite sample. This is also the location where the hoop cracks were observed.

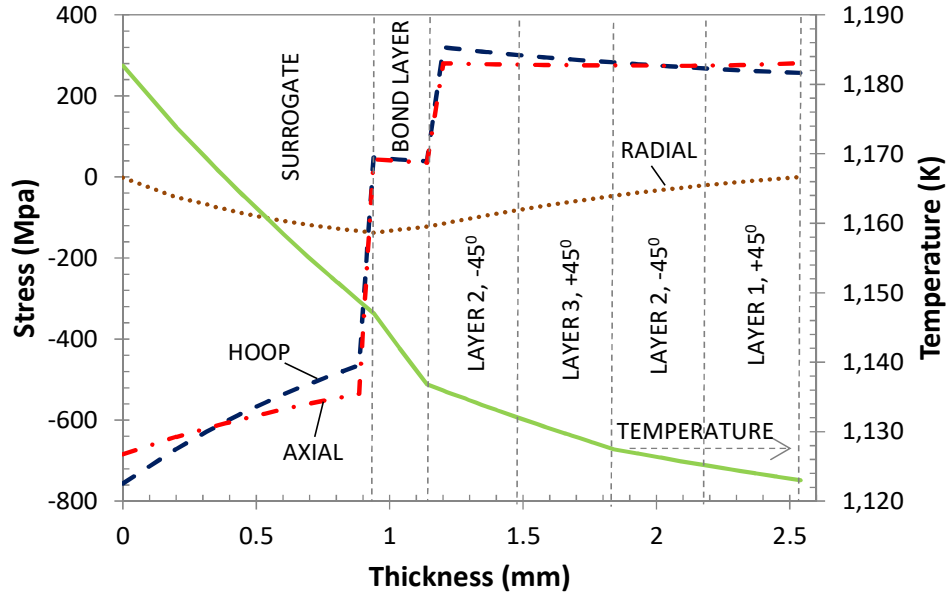


Figure 5.29: Model predicted temperature profile and stress distribution through the wall at $T_{out} = 1087 \text{ }^\circ\text{K}$ for $\text{SiC}_r\text{-SiC}_m$ sample.

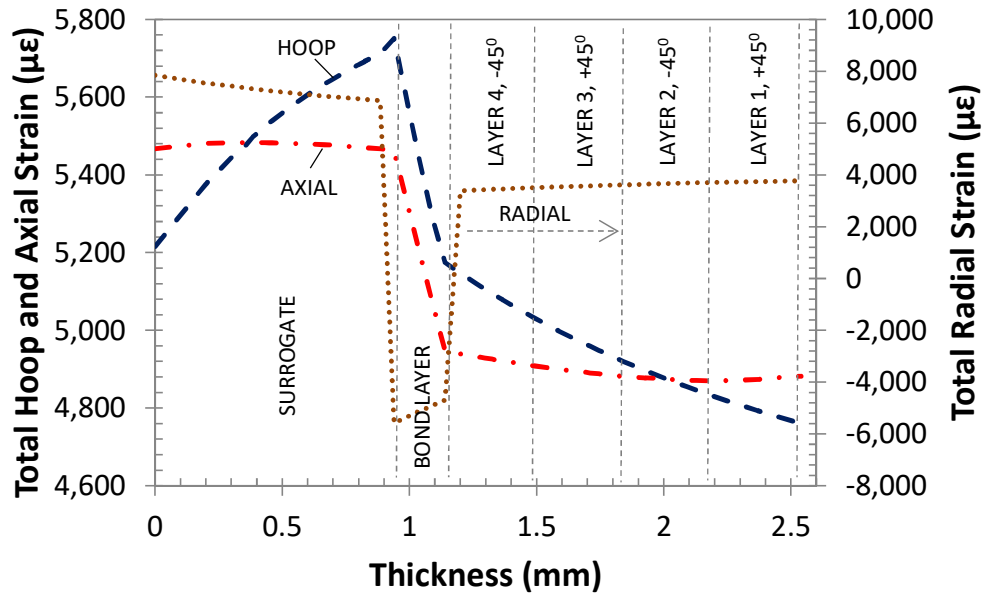


Figure 5.30: Model predicted total strain distribution through the wall at $T_{out} = 1087 \text{ K}$ for $\text{SiC}_r\text{-SiC}_m$ sample.

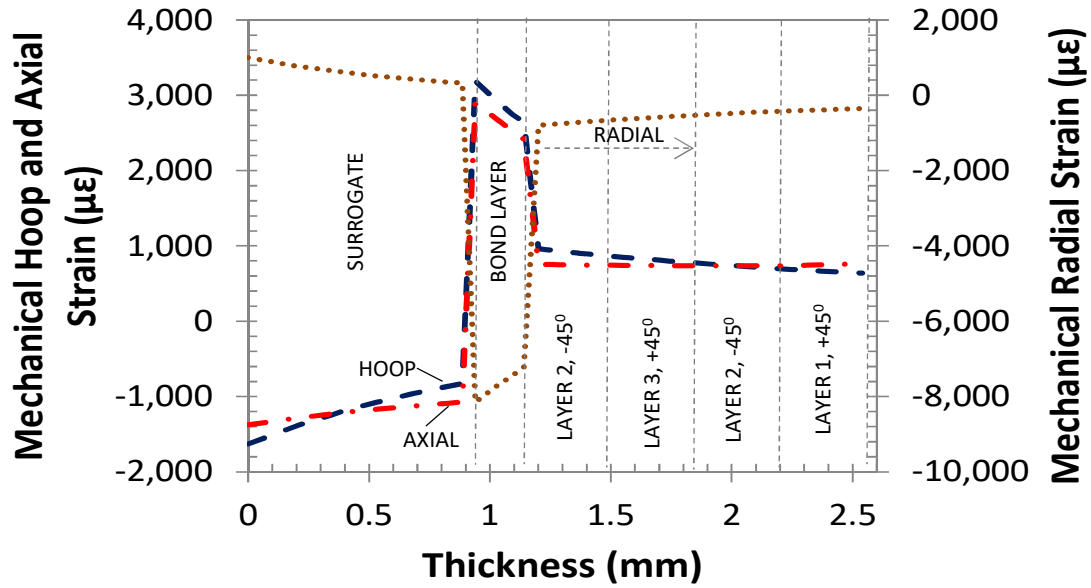


Figure 5.31: Model predicted mechanical strain distribution through the wall at $T_{\text{out}} = 1087 \text{ K}$ for $\text{SiC}_f\text{-SiC}_m$ sample.

Figure 5.32 shows the stress and strain distribution along the length of the sample. Much higher hoop strain can be found near the free edge of the sample due to the transition from plane strain to plane stress conditions near the edge. In comparison, the axial stress/strain build up from the free edge to the center of the sample due the shear lag, as expected (Figure 3.3). Due to the high hoop stress/strain in the edge affected zone, shorter samples will experience high hoop stress in a larger volume. This is believed to be one of the root causes for the different responses observed in sample type HT1, HT2, and HT3.

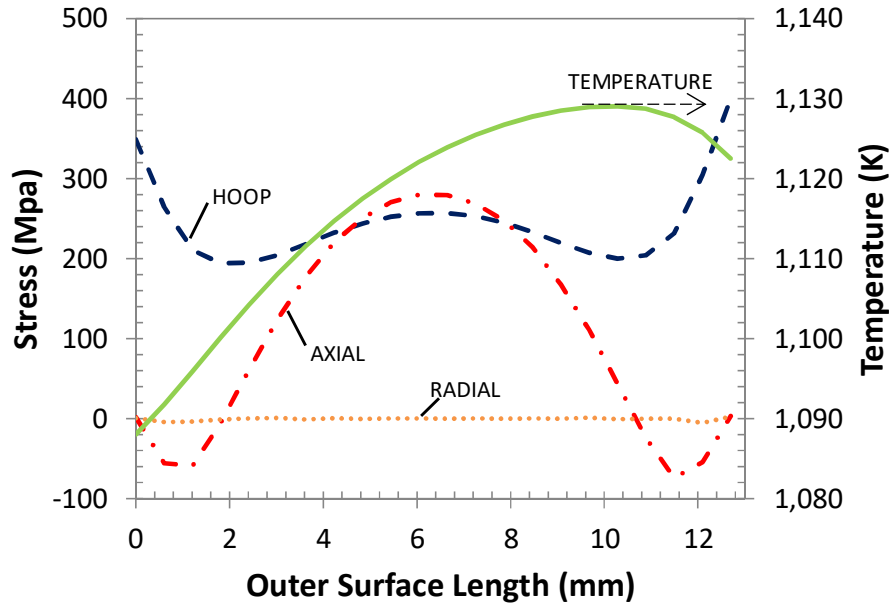


Figure 5.32: Model predicted mechanical stress distribution along the length of the sample at $T_{out} = 1087$ K for SiC_f-SiC_m sample HT1.

5.4 QUENCHING TEST RESULTS

The temperature profiles and the AE energy corresponding to the quenching of sample 2 are shown in Figure 5.33. Similar results were obtained for samples 3 and 4. In Figure 5.33, T_{in} is the temperature inside the sample-surrogate assembly, T_{out} is the temperature on the outer surface of the sample and the dots represent AE energy. The quenching process can be divided into four Phases, as shown in Figure 5.33. In Phase I an increasing pressure is applied on the holder, in Phase II the assembly is quickly displaced downwards, immersing the sample in the water and initiating the quench. During Phase III the pressure on the holder is kept steady and in Phase IV the holder has reached final position. The quenching process alone is estimated in about 4 seconds, the time needed to immerse the whole sample (107 mm long) in water is about 1 second. The quenching process in this work is estimated to be about 5 times faster than a reflooding of a pressurized

water reactor (PWR) with a cladding length of 4.3 mm [108] assuming the reflooding phase takes 200 seconds [111]. T_{in} is about 1743 °K (1470 °C) at the beginning of Phase I (19.2 sec.) and starts to decrease as the induction heater is turned off, reaching 1473 °K (1200 °C) after 7 seconds. T_{out} is about 1273 °K (1000 °C) at the beginning of Phase I, abruptly decreases in 953 °K (680 °C) during Phase II and continuous to decrease at a smaller rate during Phases III and IV, reaching 313 °K (40 °C) after 7 seconds.

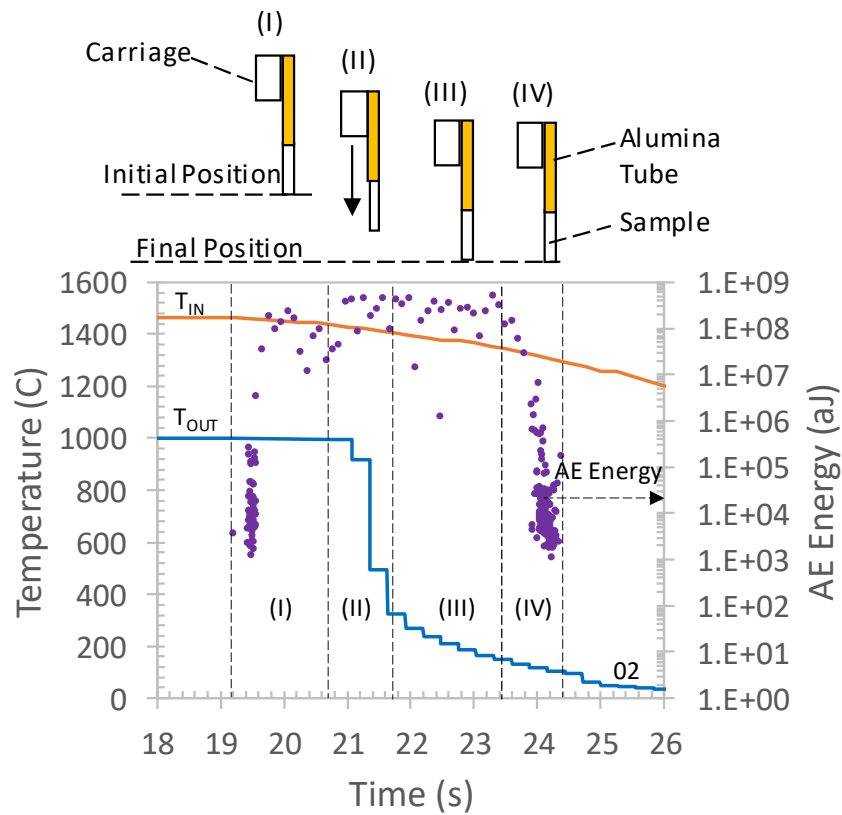


Figure 5.33: Quenching process corresponding to sample 2.

Additional details were obtained with the help of the video taken with the high-speed camera. At 21 sec. the end-plug of the sample contacted the water. From this point forward and for a very short time, vapor bubbles are formed following with a mild decrease in surface temperature. When enough vapor bubbles were produced, a vapor blanket

covered the sample (film boiling) accompanied by a reduction in heat transfer from the surface to the fluid [112]. At 21.5 sec. vapor bubbles were observed forming on the flat end of the sample. Bubble formation suggest that initiation of nucleate boiling is happening, this is accompanied by an increase in the heat transfer rate and consequently lower temperature in this area. At 21.7 sec. the sample is in final position, a wetting front is observed in the lower side of the SiC_r-SiC_m tube moving upwards. The wetting front separates the nucleate boiling from the film boiling phases [112]. At approximately 21.3 sec. Tout experiments a steep decrease of about 953 °K (680 °C) which could be related to a partial collapse of the continuous vapor blanket, this is accompanied by a high heat transfer rate [112]. This could happen in the area around the thermocouple.

Some nucleate boiling was observed at the top of the sample, close to the water surface in the final phases of quenching. Lower temperatures in this area could be attributed to heat loss by conduction through the alumina tube. The temperature data shows that T_{in} is still very high, 1473 °K (1200 °C), when Tout is about 313 °K (40 °C). It takes several minutes for the susceptor to reach RT. The mechanism of heat transfer from the hot susceptor to the sample is mainly radiation, as there is a gap between the inner surface of the sample and the susceptor. Some marginal amount of heat is lost by conduction through the ceramic cover of the B-thermocouple. The thermal gradient from the inner surface to the outer surface of the sample is determined by the heat transfer rate between the outer surface of the sample and the fluid. A faster cooling of the area around the thermocouple may be possible but this is difficult to quantify.

Film boiling was observed during the immersion of all the samples. However, the film corresponding to samples 2 and 3 was thinner and less irregular than the film of sample 4 quenched in boiling water.

The temperature profile of samples 2, 3 and 4 are shown in Figure 5.34, a normalized time is used. Time zero corresponds to the initiation of Phase II. The samples quenched in RT water shows a similar temperature profile, with a steep decrease in T_{out-2} and T_{out-3} during Phase II and a smoother decrease during Phases III and IV. The temperature at the center is similar as well, T_{in-2} and T_{in-3} . For the sample quenched in boiling water, T_{out-4} has a less steep decrease than samples quenched in water at RT. Clearly, there is a slower cooling rate on the surface of the sample. The slope in the temperature profile of T_{out-4} is the same during Phases II and III. T_{out-4} reaches the same temperature than T_{out-2} and T_{out-3} in Phase IV. The temperature at the center, T_{in-4} , decreases at a lower rate than T_{in-2} and T_{in-3} .

After quenching, a microscopic analysis showed visible cracks in samples 2 and 3, Figure 5.35, while no visible cracks were found in sample 4. The cracks on the face located at the lower end of the SiC_f-SiC_m composite tubes of samples 2 and 3, extended towards the lateral side however does not compromise the composite. After the quenching, a large portion of the monolithic endplug region of sample 2 was broken apart, Figure 5.35(a). In a fuel rod, the failure of the endplug could cause the release of the radioactive fission products into the coolant and eventually into the environment. Reducing the quenching temperature difference between the outer surface of the endplug and the quenching media improves the strength of the monolithic SiC, depending on the fabrication method [65]. FEA may help to improve the design of the plug.

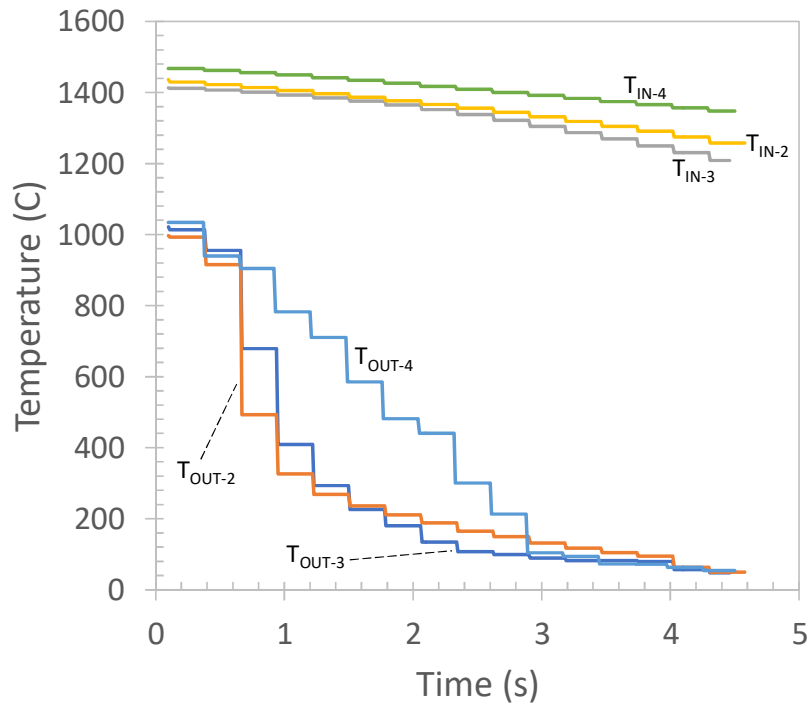


Figure 5.34: Temperature profile of samples 2, 3 and 4.

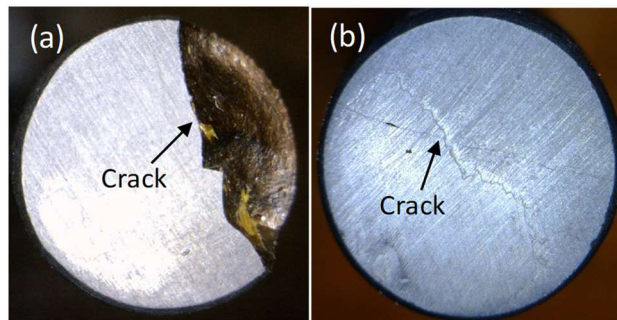


Figure 5.35: Cracks in the face of the endplug of the composite tube, sample 2 (a) and sample 3 (b).

5.4.1 AE ANALYSIS

Based on extensive observations of AE signals corresponding to various mechanical tests of $\text{SiC}_f\text{-SiC}_m$ composite tubes, such as burst tests, high temperature solid-surrogate tests and quenching tests conducted previously, a criterion based on the absolute AE energy was used to classify the AE signals. The AE signals were classified as high

energy when the AE energy was $\geq 10^6$ aJ and low energy when the AE energy was $< 10^6$ aJ. The high energy AE signals must be related to damage in the material. In addition to the AE energy, the amplitude in volts and the waveform of the signals were used. A summary of the AE signals found during the quenching test of sample 2 is presented in Table 5.8. Four AE signals were identified, they are (a), (b), (c) and (d). In the same table, the number of signals found in the different phases is included, in percentage of a total of 222 AE signals.

Table 5.8. Summary of AE signals corresponding to sample 2.

AE Signal	P-I	P-II	P-III	P-IV	Energy (aJ)	% of Signals
High Energy Crack (a)	X	---	X	---	$\geq 10^6$	4.5
Low Energy Crack (c)	---	---	---	X	$< 10^6$	3
High Energy Friction (b)	---	X	---	---	$\geq 10^6$	2
Low Energy Friction (d)	X	---	---	X	$< 10^6$	>80

In Figure 5.34, the waveforms corresponding to the AE signals mentioned in Table 2 are shown. The horizontal axis in Figure 5.36 is time in microseconds, and the vertical axis is the amplitude in volts (V) ranging from -0.1 V to +0.1 V. Similar waveforms were found during quenching of samples 3 and 4. More than 80% of the AE signals correspond to waveform (d) which is a low energy signal with a very small amplitude of about 0.01 V. A separate test showed that waveforms similar to waveform (d) are obtained when a thermocouple rubs against the sample or against the alumina tube. Signals like (d) are also

obtained when the sample contacts the induction coil while displacing downwards. Waveforms (d) are found in Phases I and IV (at the beginning and the end) and it is believed that they are not related to damage in the sample.

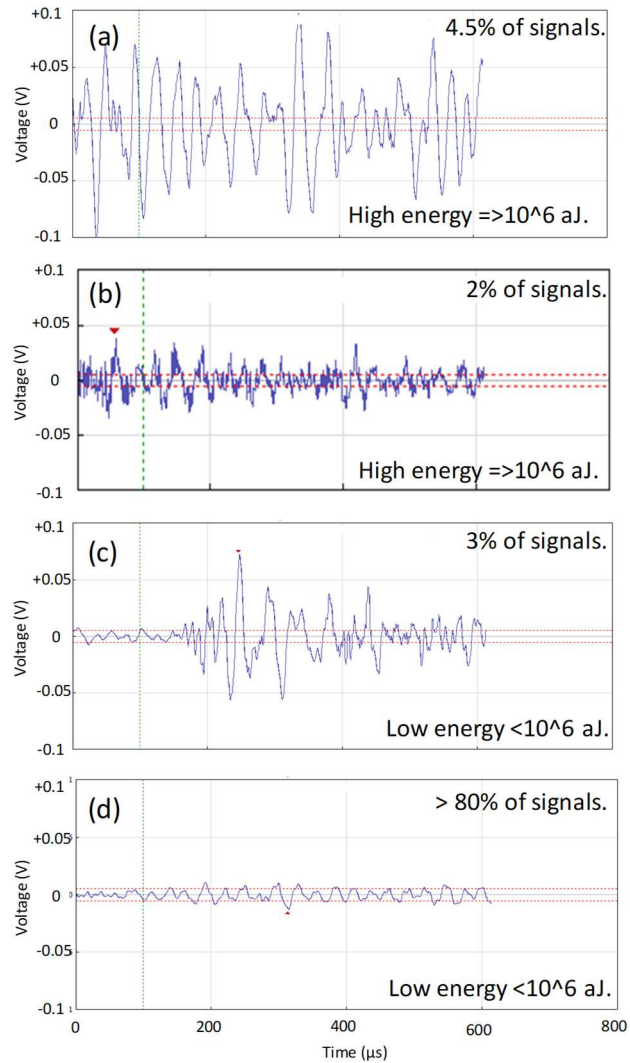


Figure 5.36: AE signals found during quenching of sample 2.

The waveform corresponding to AE signal (b) is found in Phase II only, when the sample is displaced downwards. Signal (b) is a high energy signal with high AE counts and a continuous waveform, with an amplitude of about 0.04 V. The number of signals (b) is small (2%) and the source is probably friction.

The waveforms corresponding to signals (a) and (c) have similar characteristics. Signals (a) and (c) have waveforms similar to the waveforms of AE signals corresponding to a pencil lead break, see Figure 8. Amplitude of signals (a) and (c) are in the range of about 0.1 V to 0.02 V. However, signals (a) have high energy ($\geq 10^6$ aJ) and signals (c) have low energy ($< 10^6$ aJ). Signals (a) were found in Phases I and III. Signals (c) were found in Phase IV only. The pencil lead break in Figure 8 was performed using a 0.5 mm mechanical pencil on the sample. The pencil lead break is a test used to verify the response of the AE sensor and the system, performed before the test [98]. Because of this similarity with the signal from a pencil lead break, it is possible, that AE signals (a) and (c) are related to cracks in the sample. The number of signals (a) and (c) found are 4.5% and 3% of the total of signals respectively.

It is suspected, that the presence of AE signals (a) in Phase I may be related to a misalignment of the assembly (holder-alumina rod-sample) caused when the holder is pushed down. Any deviation from the vertical position could cause the susceptor to move laterally hitting the sample, resulting in a moment applied on the area where the sample and the alumina tube are connected. The susceptor is several times heavier than the sample and the alumina tube. This could cause cracking of the ceramic paste present in the area, explaining the source of AE signals. During Phases II and III this type of event is not expected however it could be present in Phase IV.

It is believed, that the presence of signals (a) in Phase III and signals (c) in Phase IV must be related to cracks. Signals (a), with higher energy, are probably related to large cracks and signals (c), with lower energy, are probably related to small cracks.

The AE signals found during quenching of sample 3 are similar to the AE signals corresponding to sample 2. However, most of the AE signals (~99%) corresponding to sample 4 had energies less than 10^6 aJ. About 95% of signals were similar to signal (d) and 4% were similar to signal (c). Only one signal like signal (a) was found. In summary, the cracks induced to sample 4 during quenching in hot water were probably small cracks.

5.4.2 INTERNAL PRESSURE TESTS

Burst tests of samples 2, 3 and 4 were conducted after quenching. The samples were loaded to failure. Samples 2 and 3 failed at the plug and sample 4 failed close to the plug. The burst pressure and maximum stress of the samples are listed in Table 5.9. The burst pressure and maximum hoop stress of the as-fabricated sample (control) was 53.8 MPa and 175 MPa. Clearly the burst pressure and the stress at failure of samples 2, 3 and 4 are lower than the (control) sample. These are preliminary results; more tests will be conducted in the future.

Table 5.9: Results of the close-end burst test.

Close-End Samples	Water Temperature (C)	Burst Pressure (MPa)	Maximum Hoop Stress (MPa)
1-Reference	---	53.8	175
2	23	32.4	118
3	23	34.5	127
4	~100	27.6	98

It appears that all samples have sustained some damage at or near the region of the end-plug, during quenching. Figure 5.37 shows the hoop strain map of sample 2 right before failure. Sample 2 failed on the region labeled (a) where a big crack can be seen, and the level of strains is high. In Figure 5.37, strain fringes can be seen along the sample, in

the axial direction. Two notorious fringes with an average of about $1000 \mu\epsilon$ (c) and about $4000 \mu\epsilon$ (b) can be observed in most of the surface. It is believed that partial delamination is causing relaxation and lower strains in region (c). Similar strain mapping was observed in samples 3 and 4.

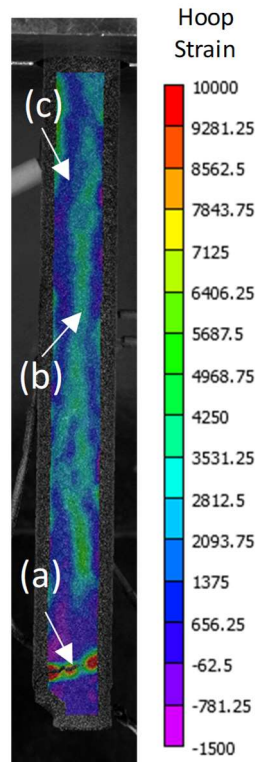


Figure 5.37: Hoop strain map at failure of sample 2.

It is suspected that quenching induced damage is concentrated near the end plug. To quantify the “undamaged” tube segments, samples 2, 3 and 4 were cut off and tested for burst strength. The damaged region was removed using a diamond saw, resulting in an open-end $\text{SiC}_f\text{-SiC}_m$ composite tube. The samples were cleaned up and then prepared as in the case of the first burst test, strain gauges were attached, and a speckle pattern for DIC was painted. The same bladder-based burst rig was used. The stress-strain curves of the

samples, corresponding to the open-end burst tests, are shown in Figure 5.36 and the results are shown in Table 5.9.

In Figure 5.38, the hoop stress vs. hoop strain curves were plotted. The strains were obtained with the DIC technique. All the samples follow approximately the same curve up to $400 \mu\epsilon$ and then separate. Clearly, the stress-strain curves of samples 2, 3 and 4 are completely non-linear, or in other words, there is no initial linear elastic region as in the case of the reference sample. The absence of the initial elastic region is a consequence of damage in the matrix caused during the previous tests. The curve of samples 2 and 3 intercept the curve of the reference sample beyond the PLS (Proportional Limit Stress) and above the $700 \mu\epsilon$. The PLS of the reference sample is calculated in 65 MPa. Sample 2 shows a higher strain and higher stress at failure compared to the reference sample, however this variation in stress and strain is not atypical. Samples 3 and 4 have lower stresses and strains at failure compared to the reference sample. The stress-strain curves of samples 2, 3 and 4, especially from samples 2 and 3, are similar to a reloading curve of the reference sample, as in a loading-unloading burst test. This is possible because the burst pressures during the close-end burst tests, Table 5.9, are lower than the burst pressure during the open-end burst test, Table 5.10.

Table 5.10: Results of the open-end burst tests.

Open-End Samples	Burst Pressure (MPa)	UTS (MPa)
1-Reference	56.6	166
2	49.6	182
3	43.2	159
4	40.3	147

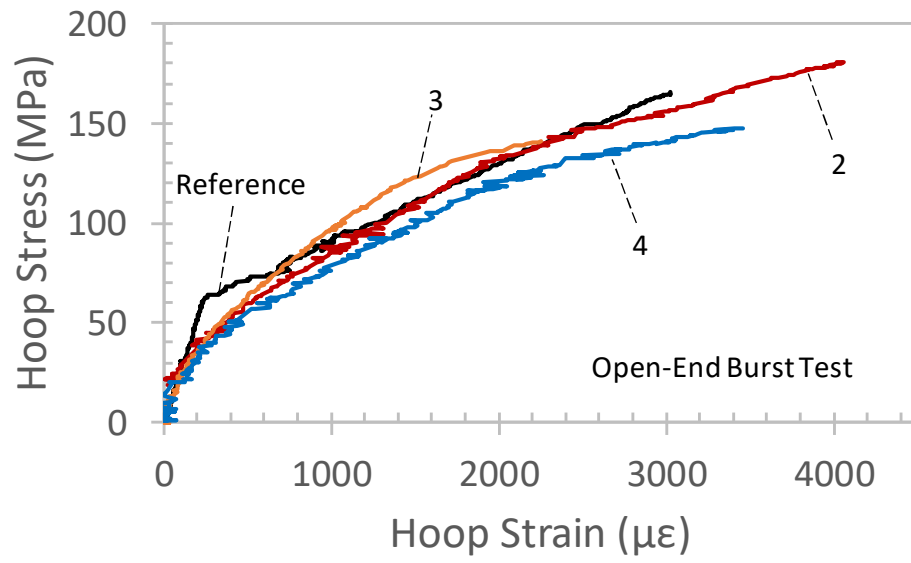


Figure 5.38: Open-end burst test results.

CHAPTER 6

CONCLUSIONS

Some of the loading conditions experienced by the nuclear cladding during accidents, such as high hoop stress, PCMI and thermal shock, were successfully simulated in laboratory conditions.

An analysis of the stress-strain curve obtained from the RT open-end internal pressure tests reveals the existence of three regions, an elastic region, a matrix-driven region and a fiber-driven region. The transition from one region to another coincides with a noticeable change in slope of the stress-strain curve of the sample.

The uniaxial stress-strain curve of a batch of $\text{SiC}_f\text{-SiC}_m$ composite tubes may be predicted if the AE data of a reference sample is available and if the average elastic modulus is known. The AE data is used to calculate the damage variable of the material.

In the case of the internal pressure test, the value of the damage variable D at the end of the matrix-driven region and at failure seems to be a characteristic of the batch and may be used as a reference of progress of damage in the material.

The high energy (≥ 106 aJ) AE signals were found to be more relevant to the calculation of the damage variable D in the matrix-driven region. Therefore, high energy AE signals in this region must be related to damage.

The HT solid surrogate test induces matrix cracking in the sample however the $\text{SiC}_f\text{-SiC}_m$ composite tube shows no visible deformation. Some of the AE activity must

correspond to cracking but is not possible to differentiate between AE signals. More testing is needed to find the remaining strength of the samples after the test.

During quenching, the endplug undergoes severe damage in the form of cracks while the composite part of the sample doesn't show any damage. This is more evident when quenching in RT water. Preliminary results of post-quenching internal pressure test show that the strength of the samples in the regions far from the end plug, retains more than 88% of the original strength.

Based on the results obtained in this work, the $\text{SiC}_f\text{-SiC}_m$ composite tube has demonstrated to possess some characteristics desired in a ATF cladding. It shows high hoop strength and toughness during RT burst test even after exposure to high temperature and thermal shock. The endplug shows severe damage after quenching from 1000 C into RT water however this condition improves at lower quenching-temperature difference. The stress-strain curve of $\text{SiC}_f\text{-SiC}_m$ composite tubes can be predicted in uniaxial tension using AE data and it may be possible to predict the stress-strain relations in biaxial loading by using a combination of AE and CDM.

REFERENCES

- [1] K. Yueh, D. Carpenter, and H. Feinroth, Clad in Clay, Nuclear Engineering International, 2010, pp. 14-16.
- [2] E.D. Herderick, K. Cooper, N. Ames, New approach to join SiC for accident tolerant nuclear fuel cladding, Adv. Mater. Process. (January 2012). ASM International.
- [3] C.R.F. Azevedo, Engineering Failure Analysis, vol. 18, 2011, pp. 1943-1962.
- [4] J. Desquines, D. A. Koss, A. T. Motta, B. Cazalis, M. Petit, “The Issue of Stress State During Mechanical Tests to Assess Cladding Performance During a Reactivity-Initiated Accident (RIA)”, Journal of Nuclear Materials (2011).
- [5] T.M. Link a,1, D.A. Koss a, A.T. Motta b, “Failure of Zircaloy cladding under transverse plane-strain deformation”, Nuclear Engineering and Design 186 (1998) 379-394.
- [6] M. Nakatsuka, M. Aita, K. Sakamoto, T. Higuchi, “An open-end burst test method to obtain uniaxial hoop tensile properties of fuel cladding in a hot cell”, Journal of Nuclear Materials 434 (2013) 303-310.
- [7] R. A. Jaramillo, W. R. Hendrich, N. H. Packan, “Tensile hoop behavior of irradiated Zircaloy-4 nuclear fuel cladding”, Oak Ridge National Laboratory, ORNL/TM 2006/163.
- [8] R. S. Daum, S. Majumdar, H. Tsai1, T. S. Bray, D. A. Koss, A. T. Motta, and M. C. Billone, “Mechanical property testing of irradiated Zircaloy cladding under reactor transient conditions, in small specimen test techniques: Fourth Volume, ASTM STP 1418, West Conshohocken, Pennsylvania, 2002.
- [9] D.F. Ross Jr., W.R. Hendrich, Strength testing of monolithic and duplex silicon carbide cylinders in support of use as nuclear fuel cladding, the 30th International Conference on Advanced Ceramics & Composites, 2006.
- [10] Y. Lee, T.J. McKrell and M.S. Kazimi, “Thermal shock fracture of silicon carbide and its application to LWR fuel cladding performance during reflood”, Nuclear Engineering and Technology, Vol. 45 No. 6, November 2013.
- [11] Lahoda et al., Final technical report, “Development of LWR fuels with enhanced accident tolerance”, Westinghouse Electrical Company LLC. October 30, 2015.

- [12] S. Momon, M. Moevus, N. Godin, M. R'Mili, P. Reynaud, G. Fantozzi, G. Fayolle, "Acoustic emission and lifetime prediction during static fatigue tests on ceramic-matrix-composite at high temperature under air", *Composites Part A* 41 (2010) 913-918.
- [13] E. Maillet, N. Godin, M. R'Mili, P. Reynaud, J. Lamon, G. Fantozzi, "Analysis of acoustic emission energy release during static fatigue tests at intermediate temperatures on ceramic matrix composites: towards rupture time prediction", *Composite Science and Technology* 72 (2012) 1001-1007.
- [14] A.L. Gyekenyesi, G.N. Morscher, L.M. Cosgriff, In-situ monitoring of damage in SiC/SiC composites using acousto-ultrasonics, *Composites Part B* 37 (2006) 47-53.
- [15] T.H. Loutas and V. Loutopoulos, Health monitoring of carbon/carbon, woven reinforced composites. Damage assessment by using advanced signal processing techniques. Part I: Acoustic emission monitoring and damage mechanisms evolution, *Composites Science and Technology* 69 (2009) 265-272.
- [16] E. Maillet, N. Godin, M. R'Mili, P. Reynaud, G. Fantozzi, J. Lamon, "Damage monitoring and identification in SiC/SiC minicomposites using combined acousto-ultrasonics and acoustic emission", *Composites: Part A*: 57 (2014) 8-15.
- [17] T. Nozawa, K. Ozawa, H. Tanigawa, Re-defining failure envelopes for silicon carbide composites based on damage process analysis by acoustic emission, *Fusion Eng. Des.* 88 (9e10) (Oct. 2013) 2543-2546.
- [18] G. N. Morscher, M. Singh, J. D. Kiser, M. Freedman, R. Bhatt, "Modeling stress-dependent matrix cracking and stress-strain behavior in 2D woven SiC fiber reinforced CVI SiC composites", *Composites Science and Technology* 67 (2007) 1009-1017.
- [19] G.N. Morscher, Modal acoustic emission of damage accumulation in a woven SiC/SiC composite, *Compos. Sci. Technol.* 59 (1999) 687-697.
- [20] R.S. Williams and K.L. Reifsnider, Investigation of acoustic emission during fatigue loading of composite specimens, *Journal of Composite Materials*, Vol. 8 (October 1974) p. 340.
- [21] Eiichi Jinen, The determination of G_c fracture toughness values for short carbon fiber reinforced nylon 66 (FRTP) by acoustic emission, *Engineering Fracture Mechanics*, Vol. 21, No. 1, p. 157-171, 1985.
- [22] A. Garg, O. Ishai, Characterization of damage initiation and propagation in graphite/epoxy laminates by acoustic emission, *Engineering Fracture Mechanics* Vol. 22, No. 4, p. 595-608, 1985.

- [23] Qing-Qing Ni and E. Jinen, Acoustic emission and fracture of carbon fiber reinforced thermosoftening plastic (CFRTP) materials under monotonous tensile loading, *Engineering Fracture Mechanics*, Vol. 45 No. 5 p. 611-625, 1993.
- [24] N. Lissart and J. Lamon, Damage and failure in ceramic matrix minicomposites: experimental study and model, *Acta mater.*, Vol. 45, No. 3, p. 1025-1044, 1997.
- [25] M. Surgeon, E. Vanswijgenhoven, M. Wevers and O. Van Der Biest, Acoustic emission during tensile testing of SiC-fiber-reinforced BMAS glass-ceramic composites, *Composites Part A* 28A (1997) 473-480.
- [26] Y.Z. Pappas, Y.P. Markopoulos, V. Kostopoulos, Failure mechanisms analysis of 2D carbon/carbon using acoustic emission monitoring, *NDT&E International*, Vol. 31, No. 3, p. 157-163, 1998.
- [27] Y.A. Dzenis and J. Qian, Analysis of microdamage evolution histories in composites, Faculty publications from the Department of Engineering Mechanics, University of Nebraska-Lincoln, 2001.
- [28] Q-Q. Ni and M. Iwamoto, Wavelet transform of acoustic emission signals in failure of model composites, *Engineering Fracture Mechanics* 69 (2002) 717-728.
- [29] G.N. Morscher, Stress-dependent matrix cracking in 2D woven SiC-fiber reinforced melt-infiltrated SiC matrix composites, *Composites Science and Technology* 64 (2004) 1311-1319.
- [30] C.R. Ramirez-Jimenez, N. Papadakis, N. Reynolds, T.H. Gan, P. Purnell, M. Pharaoh, Identification of failure modes in glass/polypropylene composites by means of the primary frequency content of the acoustic emission event, *Composites Science and Technology* 64 (2004) 1819-1827.
- [31] F. Kaya, Damage assessment of oxide fiber reinforced oxide ceramic matrix composites using acoustic emission, *Ceramics International* 33 (2007) 279-284.
- [32] M. Moevus, N. Godin, M. R'Mili, D. Rouby, P. Reunaud, G. Fantozi, G. Farizy, "Analysis of damage mechanisms and associated acoustic emission in two SiCf/[Si-B-C] composites exhibiting different tensile behaviors. Part II: Unsupervised acoustic emission data clustering", *Composites Science and Technology* 68 (2008) 1258-1265.
- [33] Y. Wang, L. Zhang, L. Cheng, J. Ma, W. Zhang, "Tensile performance and damage evolution of a 2.5-D C/SiC composite characterized by acoustic emission", *Appl. Composite Material* (2008) 15:183-188.

- [34] J. Cuadra, P.A. Vanniamparambil, K. Hazeli, I. Bartoli, A. Kontsos, Damage quantification in polymer composites using a hybrid NDT approach, *Composites Science and Technology* 83 (2013) 11-21.
- [35] SV. Lomov, M. Karahan, AE. Bogdanovich, I. Verpoest, Monitoring of acoustic emission damage during tensile loading of 3D woven carbon/epoxy composites, *Textile Research Journal* 2014, Vol. 84(13) 1373-1384.
- [36] F. Breeded, D. Koch, E. Maillet, G.N. Morscher, Modal acoustic emission of damage accumulation in C/C-SiC composites with different fiber architectures, *Ceramics International* 41 (2015) 12087-12098.
- [37] Gerald Camus, "Modelling of the mechanical behavior and damage processes of fibrous ceramic matrix composites: application to a 2-D SiC/SiC", *International Journal of Solids and Structures* 37 (2000) 919-942.
- [38] X. Aubard, "Modelling of the mechanical behavior of a 2-D SiC-SiC composite at a meso-scale", *Composites Science and Technology* 54 (1995) 371-378.
- [39] J. Lemaitre, "A course on damage mechanics", Springer-Verlag 1992.
- [40] M. A. Sutton, J. J. Orteu, H.W. Schreider, "Image Correlation for Shape, Motion and Deformation Measurements", Springer (2009).
- [41] M.D. Novak, F.W. Zok, High-temperature materials testing with full-field strain measurement: experimental design and practice, *Rev. Sci. Instrum. Pract.* 82 (2011).
- [42] S. J. Zinkel, K. A. Terrani, J. C. Gehin, L. J. Ott, L. L. Snead, "Accident tolerant fuels for LWRs: a perspective", *Journal of Nuclear Materials* 448 (2014) 374-379.
- [43] J. Carmack, Update on U.S. accident tolerant fuel program, DOE, Idaho National Laboratory, February 9, 2016.
- [44] C.L. Whitmarsh, "Review of Zircaloy-2 and Zircaloy-4 properties relevant to N.S. Savannah reactor design", Oak Ridge National Laboratory, ORNL-3281.
- [45] L. Hallstadius, S. Johnson, E. Lahoda, "Cladding for high performance fuel", *Progress in Nuclear Energy* 57(2012) 71-76.
- [46] V.A. Avincola, M. Grosse, U. Stegmaier, M. Steinbrueck, H.J. Seifert, "Oxidation at high temperatures in steam atmosphere and quench of silicon carbide composites for nuclear applications", *Nuclear Engineering and Design* 295 (2015) 468-478.

- [47] J.G. Stone, R. Schleicher, C.P. Deck, G.M. Jacobsen, H.E. Khalifa, C.A. Back, “Stress analysis and probabilistic assessment of multi-layer SiC-based accident tolerant nuclear fuel cladding”, *Journal of Nuclear Materials* 466 (2015) 682-697.
- [48] W-J. Kim, D. Kim, J. Y. Park, “Fabrication and material issues for the application of SiC composites to LWR fuel cladding”, *Nuclear Engineering and Technology*, Vol. 45 No. 4 August 2013.
- [49] D. Kim, H-G. Lee, J. Y. Park, W-J. Kim, “Fabrication and measurement of hoop strength of SiC triplex tube for nuclear fuel cladding applications”, *Journal of Nuclear Materials* 458 (2015) 29-36.
- [50] G.M. Jacobsen, J.D. Stone, H.E. Khalifa, C.P. Deck, C.A. Back, “Investigation of the C-ring test for measuring hoop tensile strength of nuclear grade ceramic composites”, *Journal of Nuclear Materials* 452 (2014) 125-132.
- [51] J. Lamon, “Approach to microstructure behavior relationships for ceramic matrix composites reinforced by continuous fibers”, Chapter 8, *Ceramic Matrix Composites: Materials, Modeling and Technology*, 1st Edition, 2015.
- [52] M. H. Dirikolu, A. Aktas, B. Birgoren, “Statistical analysis of fracture strength of composite materials using Weibull distribution”, *Turkish J. Eng. Env. Sci.* 26 (2002) 45-48.
- [53] O.M. Jadaan, D.L. Shelleman, J.C. Conway, Jr., J.J. Mecholsky, Jr., R.R. Tressler, “Prediction of the strength of ceramic tubular components: Part I – Analysis”, *American Society for Testing and Materials* 1991.
- [54] E. Barbero, J. Fernandez-Saez, C. Navarro, “Statistical analysis of the mechanical properties of composite materials”, *Composites Part B: Engineering*, 2000, Vol. 31, Nol 5, 375-381.
- [55] O. M. Jadaan, D. L. Shelleman, J. C. Conway, Jr., J. J. Mecholsky, Jr., and R. E. Tressler, “Prediction of the strength of ceramic tubular components: Part I – Analysis”, *American Society for Testing and Materials*, 1991.
- [56] C-S Seok, B-K Bae, J-M Koo, K. L. Murty, “The properties of the ring and burst creep of ZIRLO cladding”, *Engineering Failure Analysis* 13 (2006) 389-397.
- [57] F. Nagase, T. Fuketa, “Investigation of hydride rim effect on failure of Zircaloy-4 cladding with tube burst test”, *Journal of Nuclear Science and Technology*, Vol. 42, No. 1, p. 58-65 (January 2005).
- [58] R. Carter, “Compressed elastomer method for internal pressure testing”, *Army Research Laboratory*, ARL-TR-3921, September 2006.

- [59] K.F. Nilsson, O. Martin, C. Chenel-Ramos, J. Mendes, “The segmented expanding cone-mandrel test revisited as material characterization and component test for fuel claddings,” *Nuclear Engineering and Design*, 241(2), 2011, pp 445-458.
- [60] L. Chuck, G. A. Graves, “Hoop Tensile Strength and Fracture Behavior of Continuous Fiber Ceramic Composite (CFCC) Tubes from Ambient to Elevated Temperatures”, *Journal of Composites Technology and Research* (1997).
- [61] T. S. Byun, E. Lara-Curzio, R. A. Lowden, L. L. Snead, Y. Katoh, “Miniaturized fracture stress tests for thin-walled tubular SiC specimens”, *Journal of Nuclear Materials* 367 (2007) 653-658.
- [62] D. M. Carpenter, “An assessment of silicon carbide as a cladding material for light water reactors”, PhD Thesis, MIT 2010.
- [63] J. D. Stempien, “Behavior of Triplex silicon carbide fuel cladding designs tested under simulated PWR conditions”, PhD Thesis, MIT 2011.
- [64] E. Rohmer, E. Martin, C. Lorrette, “Mechanical properties of SiC/SiC braided tubes for fuel cladding”, *Journal of Nuclear Materials* 453 (2014) 16-21.
- [65] K. Shapovalov, G.M. Jacobsen, L. Alva, N. Truesdale, C.P. Deck, X. Huang, “Strength of SiCf-SiCm composite tube under uniaxial and multiaxial loading”, *Journal of Nuclear Materials* 500 (2018) 280-294.
- [66] L. Chuck, A. Szweda, “High-temperature hoop tensile strength testing and failure analysis of a braided Nicalon/PIP Si-C-N ceramic matrix composite tube”, *Proceedings of 18th Conference of Metal Matrix, Carbon and Ceramic Matrix Composites*.
- [67] D. L. Shelleman, O. M. Jadaan, D. P. Butt, R. E. Tressler, J. R. Hellmann, and J. J. Mecholsky, Jr., “High temperature tube burst test apparatus”, *Journal of Testing and Evaluation*, JTEVA, Vol. 20, No. 4, July 1992, p. 275-284.
- [68] H. Wang and R.N. Singh, “Thermal shock behavior of ceramics and ceramic composites”, *International Materials Reviews* 1994 Vol. 39 No. 6.
- [69] R.N. Singh and H. Wang, “Thermal shock behavior of fiber-reinforced ceramic matrix composites”, *Composites Engineering*, Vol. 5 No. 10-11, pp.1287-1297, 1995.
- [70] Bacalski et al.
- [71] J.P. McCrory, S.K. Al-Jumaili, D. Crivelli, M.R. Pearson, M.J. Eaton, C.A. Featherston, M. Guagliano, K.M. Holford, R. Pullin, *Damage classification in*

carbon fiber composites using acoustic emission: A comparison of three techniques, *Composites: Part B* 68 (2015) 424-430.

- [72] P. Forio, J. Lamon, “Mechanical behavior of a 2D SiC/SiC composite with a multilayered matrix”, in: *Proceedings of International Committee on Composite Materials*, Bordeaux, France, 2012.
- [73] T. Weng, A. Hiltner and E. Baer, Damage analysis in reinforced LCP composites by acoustic emission location techniques, *Journal of composite materials*, Vol. 24- January 1990.
- [74] A. Brendel, V. Paffenholz and S. Kimming, Fracture behavior of SiC monofilament reinforced copper – an acoustic emission study, *Journal of Composite Materials* 0(0) 1-8 2013.
- [75] M. Ohtsu, M. Ichinose and H. Watanabe, Damage estimation of concrete by AE rate process analysis, *Journal of Acoustic Emission* 20 (2002).
- [76] M. Zhou, W.B. Yao, X.S. Yang, Z.B. Peng, K.K. Li, C.Y. Dai, W.G. Mao, Y.C. Zhou and C. Lu, In-situ and real-time tests on the damage evolution and fracture of thermal barrier coatings under tension: A coupled acoustic emission and digital image correlation, *Surface & Coatings Technology* 240 (2014) 40-47.
- [77] M. Ji, Y-D. Zhang, W-P. Liu, L. Cheng, “Damage evolution law based on acoustic emission and Weibull distribution of granite under uniaxial stress”, *Acta Geodyn. Geomater.*, Vol. 11, No. 3 (175), 269-277, 2014.
- [78] G.N. Morscher, Intermediate-temperature stress rupture of a woven Hi-Nicalon, BN-Interphase, SiC-matrix composite in air, *J. Am. Soc.* 83 [6] 1441-49 (2000).
- [79] S. Momon, N. Godin, P. Reynaud, M. R’Mili and G. Fantozzi, Unsupervised and supervised classification of AE data collected during fatigue test on CMC at high temperature, *Composites: Part A* 43 (2012) 254-260.
- [80] E. Maillet, N. Godin, M. R’Mili, P. Reynaud, G. Fantozzi and J. Lamon, Real-time evaluation of energy attenuation: A novel approach to acoustic emission analysis for damage monitoring of ceramic matrix composites, *Journal of the European Ceramic Society* 34 (2014) 1673-1679.
- [81] R. Talreja, “A continuum mechanics characterization of damage in composite materials”, *Proc. R. Soc. Lond. A* 399, 195-216 (1985).
- [82] A. Burr, F. Hild, F. A. Leckie, “Micro-mechanics and continuum damage mechanics”, *Archive of Applied Mechanics* 65 (1995) 437-456.

- [83] G. Aiello, L. Giancarli, H. Golfier, J-F. Maire, “Modeling of mechanical behavior and design criteria for SiCf/SiC composite structures in fusion reactors”, *Fusion Engineering and Design* 65 (2003) 77-88.
- [84] J-F. Maire, P-M. Lesne, “An explicit damage model for the design of composites structures”, *Composites Science and Technology* 58 (1998) 773-778.
- [85] P. Ladeveze, E. Le Dantec, “Damage modelling of the elementary ply for laminated composites”, *Composites Science and Technology* 43 (1992) 257-267.
- [86] C. Rospars, E. Le Dantec, F. Lecuyer, “CMC damage prediction by micro-macro modeling”.
- [87] C. P. Deck, H. E. Khalifa, B. Sammulu, T. Hilsabeck, C. A. Back, “Fabrication of SiC-SiC composites for fuel cladding in advanced reactor designs”, *Progress in Nuclear Energy* 57 (2012) 38-45.
- [88] C. P. Deck, G. M. Jacobsen, J. Sheeder, O. Gutierrez, J. Zhang, J. Stone, H. E. Khalifa, C. A. Back, “Characterization of SiC-SiC composites for accident tolerant fuel cladding”, *Journal of Nuclear Materials* 466 (2015) 667-681.
- [89] L.H. Alva, X. Huang, G.M. Jacobsen, C.A. Back, High pressure burst testing of SiCf-SiCm composite nuclear fuel cladding, *Advancement of Optical Methods in Experimental Mechanics*, Volume 3, pp 387-393, 2014.
- [90] Seely FB, Smith JO (1952) *Advanced mechanics of materials*, Wiley, New York.
- [91] L. Alva, K. Shapovalov, G. Jacobsen, C. Back, X. Huang, Experimental study of thermos-mechanical behavior of SiC composite tubing under high temperature gradient using solid surrogate, *Journal of Nuclear Materials* 466 (2015) 698-711.
- [92] A.L. Eustice, *The Nernst Glower, its Development, Characteristics and Application to Illumination*, Armour Institute of Technology, 1910.
- [93] Y. Pan, Y.I. Xiao-su, Thermodynamic Analysis of the Chemical Stability of Silicon Carbide and Alumina Interface, TB332, TQ174. 75 8. 22
- [94] Y.A. Cengel, R.H. Turner, J.M. Cimbala, *Fundamentals of Thermal-fluids Sciences*, third ed., McGrawHill, 2008.
- [95] J.S. Lyons, J. Liu, M.A. Sutton, *High-temperature Deformation Measurements using Digital-image Correlation*, Springer, March 1996.
- [96] J. L. Chaboche, P. M. Lesne, J. F. Maire, “Macroscopic modeling and damage processes in CMC’s, High-Temperature Ceramic-Matrix Composites I, The American Ceramic Society.

- [97] R. M. O'higgins, C. T. McCarthy, M. A. McCarthy, "Identification of damage and plasticity parameters for continuum damage mechanics modelling of carbon and glass fiber-reinforced composite materials", *Strain* (2011) 47, 105-115.
- [98] D. Shi, X. Xiao, "Implementation of a new continuum damage mechanics model for composites in LS-DYNA", 13th International LS-DYNA Users Conference, Session: Constitutive Modeling.
- [99] *Nondestructive testing handbook*, 3rd edition, Volume 6, Acoustic emission testing, American Society for Nondestructive Testing.
- [100] PCI-2 Manual, Mistras Group.
- [101] G. N. Morscher, H. M. Yun, J. A. DiCarlo, "In-plane cracking behavior and ultimate strength for 2D woven and braided melt-infiltrated SiC/SiC composites tensile loaded in off-axis fiber directions.
- [102] W.A. Curtin, Multiple matrix cracking in brittle matrix composites, *Acta metal. Mater.* Vol. 41, No. 5, pp. 1369-1377, 1993.
- [103] F. Bernachy-Barbe, L. Gelebart, M. Bornert, J. Crepin and C. Sauder, Characterization of SiC/SiC composites damage mechanisms using Digital Image Correlation at the two scale, *Composites: Part A* 68 (2015) 101-109.
- [104] L. Li, Fatigue life prediction of fiber-reinforced ceramic-matrix composites with different fiber preforms at room and elevated temperatures, *Materials* 2016, 9, 207; doi:10.3390/ma9030207.
- [105] Y. Chen, L. Gelebart, C. Chateau, M. Bornert, A. King, C. Sauder and P. Aimedieu, Full 3D damage characterization of SiC/SiC composite tubes by X-ray tomography, 3rd International Conference on Tomography of Materials and Structures, Lund, Sweden, 26-30, June 2017, ICTMS2017-16-1.
- [106] W.-S. Kuo, T.-W. Chou, Modeling on nonlinear constitutive relations of woven ceramic composites, *Ceram. Eng. Sci. Pro* 12 (7-8) (1991) 1556-1573.
- [107] T. Helfer, P. Garcia, J.-M. Ricaud, D. Plancq, C. Struzik, Modelling the effect of oxide fuel fracturing on the mechanical behavior of fuel rods, in: Nuclear Energy Agency, Seminar Proceedings Aix-en-Provence, France, March 2004.
- [108] R.G. Munro, Material properties of a sintered α -SiC, Ceramics Division, NIST, Gaithersburg, 1997.
- [109] L.L. Snead, T. Nozawa, Y. Katoh, T-S. Byun, S. Kondo, D.A. Petti, *J. Nuclear Materials* 371 (2007) 329-377.

- [110] J.K. Shultis and R.E. Faw, "Fundamentals of nuclear science and engineering", CRC Press 2008.
- [111] "Nuclear fuel behavior in Loss-of-coolant (LOCA) accident conditions", Nuclear Energy Agency 2009.
- [112] B. Liscic, H.M. Tensi, L.C.F. Canale, G.E. Totten, "Quenching theory and technology", 2nd Edition CRC Press 2010.

APPENDIX A – MATERIAL PROPERTIES USED IN FEM SIMULATION

The material properties used in FEM simulation of the SiC_f-SiC_m composite at high temperature are shown in the Table below.

	SiC Composite	Alumina Surrogate ^d	Bond Layer ^e	Monolithic SiC
Elastic Modulus, E (GPa)	E ^a	359	18	332 ^f
CTE, α (1/K)	α^b	α^d	3E ⁻⁶	α^g
Thermal Conductivity, k (W/m K)	k ^c	k ^d	5	k ^h
Poisson Ratio, ν	0.2 ^a	0.25	0.1	0.17 ⁱ

^a Anisotropic material properties, Kuo et al [104]. E₁₁ = 3.2E¹¹ GPa; E₂₂ = E₃₃ 2.86E¹¹

GPa; G₁₂ = G₁₃ = 9.5E¹⁰ GPa; $\nu_{12} = \nu_{23} = 0.2$.

^b From Snead et al., J. Nuclear Materials 371(2007) 329-377. $A = -1.8276 + 0.0178 T - 1.554 E^{-5} T^2 + 4.5246 E^{-9} T^3$ (10⁻⁶/K), T in Kelvin.

^c Temperature dependent data provided by General Atomic, $k = [-0.0003 + 1.05 E^{-5} T]^{-1}$ (W/m K), T in Kelvin.

^d National Institute of Standards and Technology (NIST) at www.ceramics.nist.gov.

^e Properties were assumed.

^f Measured by Impulse Excitation in-house.

^g Measured by dilatometry in-house.

^h Temperature dependent from R.G. Munro, “Material properties of a sintered α -SiC”,

Ceramics Division, NIST, 1997, $k = \frac{52000 e^{-1.24 \cdot 10^{-5} T}}{T+437}$ (W/m K), T in Kelvin.

ⁱ From Ortech Inc.

APPENDIX B – CONSTITUTIVE EQUATIONS AND BOUNDARY
CONDITIONS USED IN THE FEM MODEL

Constitutive equations (Hook's law) for isotropic material in the model:

$$\varepsilon_r = \frac{1}{E}(\sigma_r - \nu(\sigma_\theta + \sigma_z)) + \alpha(T - T_r)$$

$$\varepsilon_\theta = \frac{1}{E}(\sigma_\theta - \nu(\sigma_r + \sigma_z)) + \alpha(T - T_r)$$

$$\varepsilon_z = \frac{1}{E}(\sigma_z - \nu(\sigma_\theta + \sigma_r)) + \alpha(T - T_r)$$

Radiation (W/m²): $q_{rad} = \epsilon\sigma_B(T_a^4 - T^4)$

Convection (W/m²): $q_{conv} = h_a(T_{ext} - T)$

Conduction (W/m²): $q_{cond} = -k\Delta T$

Boundary conditions:

- Heat flux on inner surface of surrogate, 380 kW/m²
- Ambient temperature, $T_a = 294$ K
- Temperature inside the chamber, $T_{ext} = 600$ K